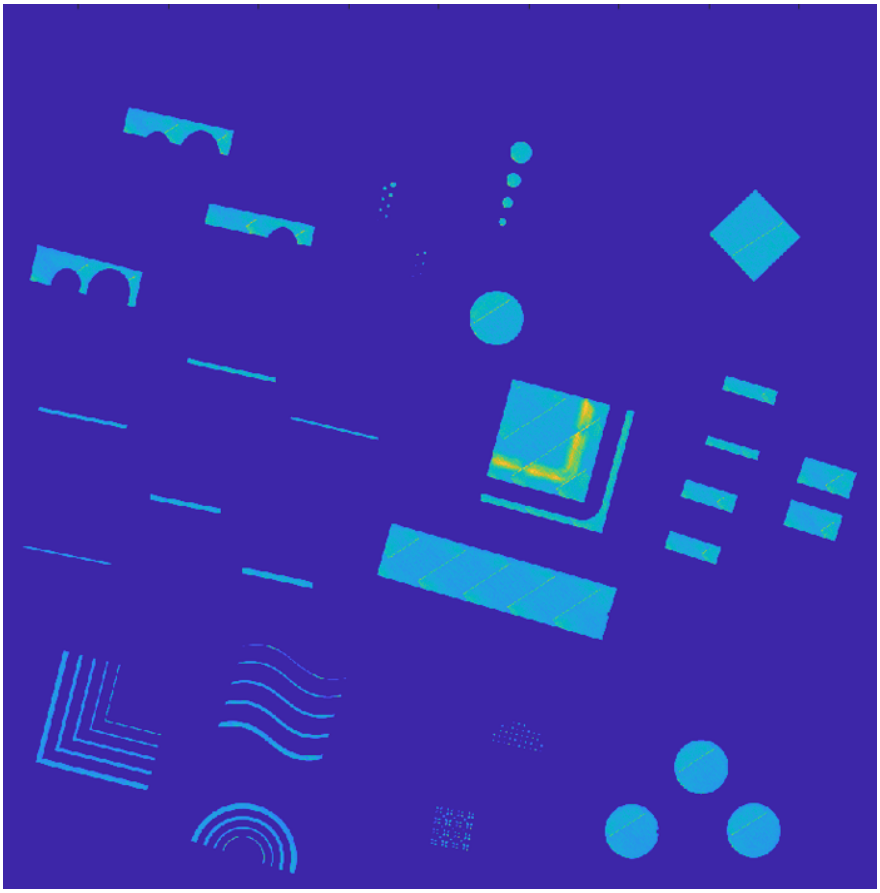

Design-driven defects in laser powder bed fusion: correlation between in-situ monitoring data and ex-situ measurements

Master's thesis in Industrial and Materials Science

NIKHIL BELSURE
VISHAL SUNDAR

DEPARTMENT OF INDUSTRIAL AND MATERIALS SCIENCE

CHALMERS UNIVERSITY OF TECHNOLOGY
Gothenburg, Sweden 2023
www.chalmers.se

Master's thesis 2023

Design-driven defects in laser powder bed fusion: correlation between in-situ monitoring and ex-situ measurements

Nikhil Belsure
Vishal Sundar

CHALMERS
UNIVERSITY OF TECHNOLOGY

Department of Industrial and Materials Science
Division of Materials and Manufacturing
Chalmers University of Technology
Gothenburg, Sweden 2023

Design-driven defects in laser powder bed fusion: correlation between in-situ monitoring and ex-situ measurements
NIKHIL BELSURE
VISHAL SUNDAR

Supervisors:
Claudia Schwerz, Department of Industrial and Materials Science
Mats Delin, GKN Aerospace Sweden AB

Examiner: Lars Nyborg, Department of Industrial and Materials Science

Master's Thesis 2023
Department of Industrial and Materials Science
Division of Materials and Manufacturing
Chalmers University of Technology
SE-412 96 Gothenburg
Telephone +46 31 772 1000

Printed by Chalmers Reproservice
Gothenburg, Sweden 2023

Design-driven defects in laser powder bed fusion: correlation between in-situ monitoring and ex-situ measurements

NIKHIL BELSURE
VISHAL SUNDAR
Department of Industrial and Materials Science
Chalmers University of Technology

Abstract

Industrial adoption of Laser Powder Bed Fusion (LPBF) is hindered by lack of process reliability and stability and the resulting build part quality. Manufacturing defect-free parts is crucial for quality-critical industries such as aerospace. Prior research has proposed in-situ monitoring of LPBF as a novel tool for early defect detection and improving process reliability. Numerous studies investigate causal correlation between anomalies in in-situ monitoring and defects and establishing ground-truth for the anomalies observed in in-situ monitoring data. However, the detection and characterization of defects generated by challenging geometries is relatively underexplored. This study aims to correlate anomalies observed in LPBF in-situ monitoring systems to design-driven defects arising from challenging geometries. Further, these defects are characterized through ex-situ measurements using non-destructive evaluation (NDE), namely X-ray computed tomography (XCT), 3D scanning, and optical surface roughness measurement. Geometries with challenging design features such as thin structures and unsupported overhangs, were designed and printed to provoke defects such as geometrical deviations, surface roughness, and internal flaws. Monitoring data obtained from the LPBF platforms, including optical tomography (OT) images, spectral data, and powder bed images, were analyzed to identify indications of these defects. Distortions in thin geometries exhibited strong correlations to protrusion of the part through the powder bed after powder dosing. Hotspots that corresponded with short hatch vectors and downskin surfaces of overhangs lesser than 45° indicated surface defects. It was observed that hotspots did not always indicate the presence of defects. Sometimes hotspots appeared in areas or parts that were exposed in the prior powder bed layer. Correlating the shifting of thin geometries due to recoater influences with the monitoring data was possible with long exposure OT. The findings highlight the importance of considering geometry-induced defects in LPBF processes and provided a validation for the anomalies observed in monitoring data.

Keywords: additive manufacturing, laser powder bed fusion, in-situ monitoring, Non-Destructive Evaluation, X-ray CT, 3D scanning, surface roughness, geometrical deviation.

Acknowledgements

This thesis was carried out with GKN Aerospace Sweden AB in collaboration with Center for Metal Additive Manufacturing (CAM2),Chalmers University of Technology.

We would like thank our supervisors Claudia Schwerz at Chalmers University of Technology and Mats Delin at GKN Aerospace Sweden AB, who gave us the opportunity to conduct our degree thesis work on this interesting topic. Their constant involvement and feedback throughout the thesis period were of high value and have aided us in successfully finalizing our work. They have been a huge support in enabling resources, providing contacts, and valuable insights on organizing the work.

This thesis project comprised of both theoretical and experimental work carried out at Chalmers University of Technology, GKN Aerospace locations at Trollhättan (SE) and Filton (UK). We would like to extend our gratitude and specially mention everyone who participated in the project. The AM printing at Filton and Chalmers were carried out by Steven Milward and Claudia Schwerz respectively. The NDE evaluations at Trollhättan were supported by Arda Baytaroglu and Rosa Sala. The 3D scanning facility at Chalmers was shared with us by Hans Sjöberg. We were trained to use the microscope and lab facilities by Erika Steyn and Antonio Mulone. Saeed Khademzadeh helped us in refining the specimen design. Code for the MATLAB was developed with Erik Henrikson, master's student in Materials Engineering department.

Finally, we would like to thank Lars Nyborg, our examiner at Chalmers University of Technology. The opponents at our presentation Garret Dawson, Ludvig Linde and Simon Anderson. Their valuable comments helped us write a better thesis report.

This work has helped us gain knowledge and insights in various engineering and research disciplines. Hopefully, the outcome of this project will be of value to the company, GKN Aerospace AB, and the Additive Manufacturing community in general.

NIKHIL BELSURE
VISHAL SUNDAR
Gothenburg, June 2023

List of Acronyms

Below is the list of acronyms that have been used throughout this thesis listed in alphabetical order:

AM	Additive Manufacturing
ASTM	American Society for Testing and Materials
AT	Acoustic Emission Testing
BCC	Body Centered Cubic
CAD	Computer-Aided Design
CAM	Computer-Aided Manufacturing
CCD	Charged coupled device
CMOS	Complementary Metal-Oxide Semiconductor
CT	Computed Tomography
DfAM	Design for Additive Manufacturing
ET	Eddy Current Testing
FCC	Face Centered Cubic
HCP	Hexagonal Closed Packed
HTML	Hypertext Markup Language
LOM	Light Optical Microscope
LPBF	Laser Powder Bed Fusion
LWIR	Long-wavelength infrared
MT	Magnetic Testing
NDE	Non-Destructive Evaluation
NIR	Near-infrared
OCT	Optical Coherence Tomography
OT	Optical Tomography
PB	Powder-bed
PNG	Portable Network Graphics
RMS	Root Mean Square
RT	Radiographic Testing
sCMOS	scientific Complementary Metal Oxide Semiconductor
STL	Stereolithography (File Format)
TIFF	Tagged Image File Format
UNS	Unified Numbering System
UT	Ultrasonic Testing
XCT	X-Ray Computed Tomography
3D	3-dimensional

Contents

List of Figures

List of Tables

1

Introduction

1.1 Background

Additive Manufacturing (AM) processes are defined as "process of joining materials to make parts from 3D model data, usually layer upon layer, as opposed to subtractive manufacturing and formative manufacturing methodologies" [1]. AM is transitioning from rapid prototyping to integration into the production chain [2]. This advanced manufacturing technology has revolutionized manufacturing by enabling the production of complex parts with reduced material wastage and rapid product realization among many other advantages [3] [4]. Laser Powder Bed Fusion (LPBF) is an AM technique that allows layer by layer manufacturing of metallic materials using thermal energy from a laser source to melt successive layers of metal powder on a powder bed [1]. LPBF stands out as a promising manufacturing technology for the aerospace industry due to its ability to produce high-resolution, lightweight, and complex parts, part consolidation and reducing lead times [5]. Titanium alloy (Ti6Al4V) and nickel superalloys like Inconel 718 (IN718), Inconel 625, Hastelloy X are processed via LPBF for aerospace applications [6].

However, the rapid adoption of LPBF for aerospace manufacturing is hindered by challenges related to process robustness, reliability, and repeatability. The stringent quality control requirements and regulatory compliance further complicate its integration into the production chain [5]. LPBF is susceptible to several defects such as porosity, lack of fusion, warpage, and detrimental effects of surface roughness, which could be parameter, material or geometry-induced. [7]. Despite process parameter optimization these defects still persist. Hence, is imperative to establish correlations between process-defect relationship to improve as built product quality and production throughput [8]. In-situ monitoring of the LPBF process has been proposed for past several years to improve the process reliability to achieve better quality as-built parts [9] [8] [10]. These monitoring techniques use various sensors and cameras to capture critical process signatures related to laser intensities, powder bed, meltpool [11]. The data collected by these sensors serves as the foundation to identify potential defects and their root causes which can help reduce variability of part quality, and properties of AM processes and components through robust process control [8].

While in-situ monitoring has been proposed to improve LPBF process reliability, the detection and characterization of defects in challenging geometries remains underexplored. Existing research primarily focuses on parameter-induced [12], seeded [13]

[14] and random defects [15]. However, in a production environment, in-situ monitoring system would be used to indicate defects that occur even with optimized parameters. Studies using non-destructive evaluation (NDE) techniques to establish ground truth for in-situ monitoring by quantifying the reliability of detection are relatively limited [16] [17]. Among the biggest challenges associated with correlating monitoring data to defects is the lack of causal correlation and the difficulty in establishing ground truths [18].

To address these gaps, this study proposes to link anomalies observed in in-situ monitoring data to the defects provoked by manufacturing challenging geometries in LPBF. This design-driven approach will likely preserve defect formation mechanisms eliminating parameter-induced or seeded defects. Furthermore, these defects will be measured by NDE methods to establish ground truths for the observations in-situ monitoring systems.

1.2 Aim

This thesis aims to investigate geometrically-induced defects in components produced using LPBF and establish correlations between these defects and the corresponding anomalies observed in real time in-situ monitoring data. Furthermore, the defects are validated using NDE methods. By achieving this objective, the study seeks to contribute to the overall quality and reliability of LPBF in aerospace manufacturing.

1.3 Scope

Defects in LPBF can be attributed to inadequate process parameters, feedstock powder, random or stochastic defects and geometry. This thesis specifically examines defects such as porosity, dimensional inaccuracies, distortion and surface roughness provoked by challenging geometries. A high amount of porosity results in lower density of as built parts and severely impacts their mechanical properties, particularly strength, elongation and fatigue properties [19]. Dimensional inaccuracies and warping can potentially cause non-conformance in the part assembly and may also lead to catastrophic failure of parts in service [20]. Surface roughness as a defect can impact mating of components and reduce fatigue performance of a component [7] [21]. All these quality parameters are critical due to their potential impact on structural integrity and performance of the part.

The study encompasses the following aspects:

- Designing and manufacturing of parts with challenging geometries - This step involved literature review of geometries considered challenging for LPBF and defects associated with these geometries. Further, the learnings from the review were applied to design parts to provoke the said defects. These were produced on two LPBF platforms in two different materials.

- In-situ monitoring data acquisition - The study focused on data acquired specifically from powder bed camera, optical tomography and spectral data on the two LPBF platforms.

- Monitoring Data Analysis - Tools like ImageJ, MATLAB and Python were used to analyze the monitoring data gathered from the LPBF systems. Indications in the monitoring data linked to various defects induced by challenging geometries were identified.

- NDE (XCT, surface roughness measurement, 3D scanning) - Appropriate NDE methods were selected and performed on each part based on the expected defects.

- Correlation of NDE results to in-situ monitoring observations - Indications observed in the in-situ monitoring and subsequent measurements in the NDE methods were correlated.

2

Literature review

2.1 Laser Powder Bed Fusion

Laser Powder Bed Fusion (LPBF) is an additive manufacturing (AM) process which uses thermal energy from laser source for fusing the surface of powder particles or fully fuse the powder particles together on a powder bed [22]. The laser beam traverses across the powder bed and the thermal energy from the laser is partially absorbed by the powder particles on the upper layers of the powder bed creating a meltpool which solidifies rapidly [23]. Subsequently the powder bed moves down by a few microns (layer thickness), a recoater brings in the new powder layer and the laser scans the powder surface again. This cycle is repeated several times until the part is completed. Fig.2.1 represents the basic LPBF process.

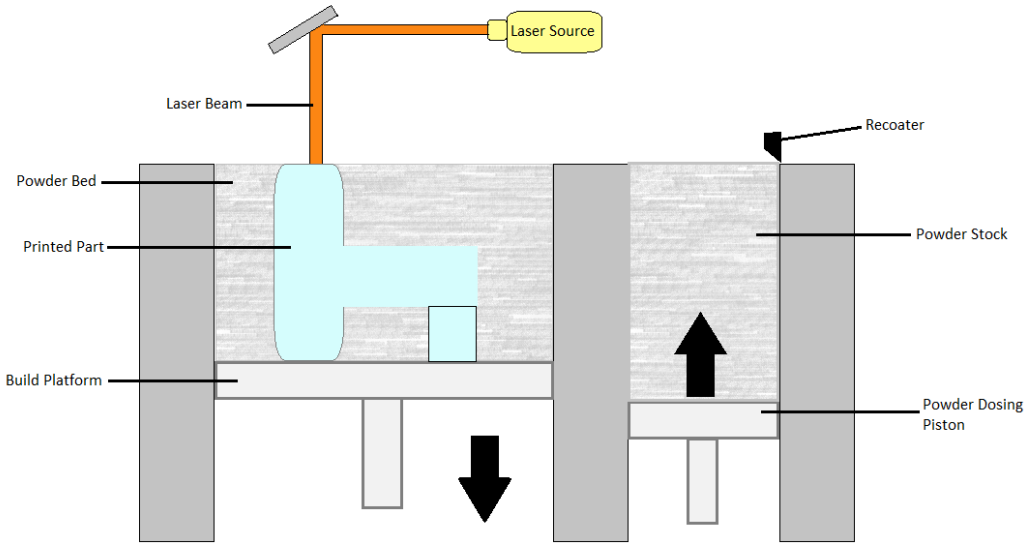

Figure 2.1: Diagram representing LPBF process.

The LPBF manufacturing process is carried out in an inert gas atmosphere to avoid oxidation and degradation. Typically, the build chamber is filled with argon gas. A combination of material properties (powder properties, composition, powder size), process parameters (laser power, layer thickness, scan speed), ambient properties

(shielding gas, gas flow direction and speed) and machine system (build plate size, motion accuracy etc), influence the part quality built in an LPBF process [24].

2.2 Defects in LPBF

The most common defects occurring in LPBF process that are widely recognised in various review articles [25] [20] [7] [26] [27][28] include:

- Internal defects such as porosity (keyhole and gas), lack-of-fusion defects.
- Geometrical and dimensional inaccuracies like shrinkage, oversizing, super-elevated edges, curling, warping and distortion.
- Surface defects like surface roughness and balling.
- Residual stresses, cracking and delamination.
- Microstructural defects like anisotropy, inhomogeneity, inclusion, partially melted powder, surface oxides and other material contamination.

To understand the formation and impact of these defects in the process, review articles classify the defect classes and sub-classes by their source [25] [20] and by their effect on the final part [27]. The sources of these defects can be traced back to the powder, process, post-process, equipment and design. The generated defects mainly affect the microstructure, surface quality, mechanical properties, geometry and dimension, of the printed part.

Internal defects relate to voids that can originate within a meltpool layer, between adjacent layers or on the external surface of the part [25]. The presence of these defects degrades the mechanical properties of the part, especially fatigue. These voids act as stress concentrations and under loading leads to formation of crack and propagation when the load is cyclic [29]. The morphology [30] and size [31] of the voids have a major effect on the fatigue performance. Large irregular pores are significant contributors to poor dynamic properties. [30] The different types of voids are keyhole porosity, gas porosity, and lack-of-fusion [25]. Gas pores are introduced in the melt pool when the trapped gases in the feedstock powder are unable to escape during rapid solidification [7] [32] [33]. Longer solidification time allow more time for the gas to escape [34]. Gas pores have a regular (spherical) morphology and smaller in size compared to keyholes pores and lack-of-fusion defects [7] [35]. Keyhole pores are entrapped gas and located generally near the bottom of the melt-pool [7] [36]. They are formed due to sudden incomplete collapse of vapor cavity under severe conditions of keyhole fusion [36]. These occurrence of these defects are reduced when the processing occurs in the conduction melting window [7]. Lack-of-fusion are unmelted regions caused by insufficient overlap between adjacent melt pools [37] [33] [15]. These occur systematically and stochastically even under optimized process parameter conditions [7] [38] [39]. Factors for lack of fusion defects include improper hatch spacing[40] [33], larger layer thickness [40] that do not allow sufficient re-melting; and insufficient melting due to various reasons that include low energy input [41], beam passing over redeposited spatter [42] [43] [44], fluctuating power absorptivity along melt pool depth due to vapor or plume formation [45]. Other factors like flow rate of the inert gas [46] and uneven powder distribution [47]

also contribute to these defects.

Geometrical inaccuracies are described as deviation in the form while dimensional inaccuracies are deviation in the size [27]. These defects affect the form/fit function of the final part permanently, causing loss of intended function for critical tolerance applications. Poor geometrical accuracy might be mainly attributed to the staircase effect [48], laser-beam positioning error [47] [49], platform movement error, gas flow velocity [46], beam spot distortions at the end of build plate [47]. The staircase effect increases with the increase in layer thickness. The contamination in the powder bed, due to gaseous byproducts and reflected energy from powder bed, impacts the local beam spatial energy distribution causing poor geometrical resolution in those regions. Increased gas velocity increases the powder bed contamination [20]. Some common dimensional deviation include shrinkage, warping, deformation, super-elevated edges [25]. Thermal shrinkage occurs due to cyclic heating [27]. This effect can be reduced by controlled laser power, proper hatch spacing, increased layer time and elevated powder bed temperature. Warping refers to surface being bent out of its natural shape and occurs due to the observed thermal gradient between the currently exposed layer and the substrate [20]. It is an effect of the thermal strain caused by the heat dissipation and thermal stresses due to by rapid solidification. Controlled heat input by proper selection of scan strategy and part design is key to overcome this defect [20]. Super-elevated edges are solidified material at edges of successive layers and are an effect of thermal strain [25]. When these defects are large enough to protrude from the powder bed, they interact with the recoating blade causing wear, non-uniform powder distribution and deforming the part. A similar effect is also observed when redeposited spatter particles on the solidified area interfere with recoating movement [20].

Cracking and delamination phenomena occur as a result of residual stress exceeding the ultimate tensile strength and binding ability of the material respectively [25]. The most prominent factor contributing to these defects is the ineffective heat dissipation influenced by the build plate thickness, temperature [50], scanning strategy [51], and/or layer thickness [52]. Parts containing residual stress have reduced mechanical properties if they are not stress-relieved post build. They can also be expected to go out of tolerance due to warpage effect observed post removal from the build plate [28].

Surface defects in the LPBF process include staircase effect [48], actual roughness of the surface [53] and balling effect [52]. Although better surface finish can be achieved post-process with surface and thermal treatments, surface defects are still relevant for its impact on the fatigue performance of the part [25]. Rough surface finish is a result of partially melted powder particles adhering to the solidified surface and surface waviness on free surface due to complex relationship of melt pool behaviour in the contour regions [20]. The general roughness of the surface is affected by the build direction [54], orientation [55], layer thickness [56], spacing between parts [57] and laser power [20]. It is to be noted that surface roughness is not the same for upward and downward surfaces. This is due to the effect of gravity which causes

the melt pool to sag into the unmelted powder from the below layers[27]. Balling occurs when the molten material solidifies as spheres instead of solid layers, creating a discontinuous scan track [25]. This phenomenon is resultant of various factors like high laser scan speed [58], surface tension [59], high oxygen content [52], rapid rate of cooling [27] and poor wetting [58]. The irregular deposition due to balling would result in rougher tracks, low surface quality, formation of open pores between discontinuous balls and failure of the build in the case of severe balling [25].

2.3 Challenging design-related features in LPBF

Design plays a crucial role in part feasibility and quality. Many authors [60] [61] [62] [63] have contributed in developing guidelines on how to design a part, standard approaches, design-manufacturing constraints, and design suitability to the particular AM technology, also known as "Design for Additive Manufacturing (DfAM). A standard process to evaluate the capability and the limitation to produce these complex geometrical features with the particular AM technology was needed to establish DfAM guidelines [64]. Researchers developed "benchmark artefacts" to assess the technological capability and limitation of a specific process [64]. Benchmark artefacts, containing one or multiple features, are used to evaluate the performance of the machine or process in producing the defined feature(s). Numerous benchmark artefacts have been used to test different capabilities of AM machines and the first sound classification of these artefacts was proposed by Mani et. al., [8] who classified it into three groups [8]. "Geometrical benchmarks" are used to characterise the accuracy and the dimensional performance. "Mechanical benchmarks" are used to characterise the mechanical properties such as stiffness, strength, shrinkage, creep characteristics, etc. "Process benchmarks" are used to establish optimum process parameters such as speed, power, layer thickness, hatching space, orientation. [65]. Some critical features seen in geometrical benchmark developed for LPBF include thin walls [3] [66] [67], overhangs [68] [21], bore holes [68], internal channels [69] [70], minimal feature sizes [68]. Lattice structures are also among the commonly investigated designs for light-weight applications [68].

The following sections describe various critical geometrical features used in various studies, and provide insights on the limits to manufacturability of these features and expected defects in the printed part. The geometrical features and commonly occurring defects associated to them are summarized in Table. 2.1.

2.3.1 Thin walls

Yang et al. [3] have described in their study the significance of individual powder particle size when producing minimal features sizes like thin walls. When the dimensions of the melt pool becomes comparable to the particle size, it is observed that capillary forces dominate the behaviour of the melt pool exhibiting Plateau-Rayleigh instability resulting in dimensional variations and increased surface roughness, or balling in some severe cases [3]. Wu et al. [66] observes a similar variation in thickness and attributes it to the low heat dissipation due to the lower thermal

conductivity of the surrounding loose powder. It is also observed that scanning pattern and subsequent excessive heat input at laser turnaround causes enlarged melt pool size leading to larger wall dimension. Wang et al. [71] observe in their study that the accuracy of the thin walls is limited by the optical spot diameter. The distortion in the wall is also attributed to powder recoating, spattering and other stochastic defects. The orientation of the walls had little effect on the manufacturability . Yang et al. [67] showed the capability to fabricate thin walls in Inconel 718 using LPBF within keyhole process parameters . Kranz et al. [72] successfully printed thin walls in Ti-6Al-4V down to 400 μm. The above studies investigated both the achievable wall dimension and the impact of orienting the wall at different angles with respect to recoater blade. Only few of the thin walls between 200 and 300 μm successfully printed due to process instability and thermal distortion [67] [72]. Similarly, studies from Wu et al. [66] showed instabilities in manufacturing walls thinner than 200 μm in 316L stainless steel. It is observed that the accumulation of shrinkage causing thermal stress distorts the thin wall both upwards and horizontal depending on direction of thermal stress. While the vertical warpage is prone to interacts with recoating blade, the horizontal warpage cause discontinuity in the build direction [66]. Excessive energy is observed in the thin wall as an effect of short raster scans on the limited cross sectional area leading to the formation of pores that are similar to end-of-track porosity [66].

2.3.2 Unsupported Features

Jones et al. [21] investigated the role of shape and inclination in defects produced in LPBF process. Their study describes how flat surfaces are prone to warping at low inclination with respect to powder bed and highlights the importance of curvature in reducing the warping effect. Using coupons with varying thickness and curvatures, inferences on part quality were made in the regions (critical regions) where the inclination angles with respect to the powder bed were below 30° or above 150°. It was found that inclination angles below 30° showed large deflection, increased surface roughness and possible part failure [21]. It is also observed that thickness also plays a role in the deflection, with thicker walls showing less deflection. This behaviour with critical angles was attributed to lack of material substrate to support the track in subsequent layers, insufficient heat conduction, and subsequent slower cooling rate. The slower cooling rate causes increased melt pool depth and dross formation in the downskin surface. For thinner walls, similar defect formation is observed on the upskin surfaces [21].

Herzog et al. [68] in their comprehensive study carried out analytical and experimental work on IN718 produced using LPBF for several unsupported critical features. From the manufacturing of unsupported inclined wall, it was observed that walls down to 25° were fully built. Higher surface roughness was observed in the downskin surface of the parts for inclination angles greater than 50° [68]. Bridge-like structures built with flat overhangs >3 mm showed considerable fall-in on the downskin surface. Unsupported horizontal holes of diameters from 1 mm to 12 mm showed high material fall-in at the top. Holes with diameter <4mm showed deviation in

diameter overall. Dahmen et al. [69] in their study investigated the hollow cylinders with its main axis perpendicular to build direction. A decrease in cross sectional area due to dross formation in cylinders of diameter greater than 2mm was observed. This behaviour is attributed to powder particles unintentionally partially melted to the internal walls due to insufficient heat dissipation. This effect decreases with increase in nominal diameter. A high degree of dross formation is also observed for cylinder diameters less than 0.8mm, clogging the hollow channels [69]. Klingaa et al. [70] observed a similar deviation on a helical cooling channels and characterizes the defect as surface deviation. A higher surface roughness was observed in the overhanging areas as compared to the opposite half of the channel and it was concluded that the surface roughness of cooling channels are highly dependent on the orientation [70].

2.3.3 High aspect ratio parts

Vertically-built bars with diameters less than 2.5mm are difficult to manufacture to their target dimensions [68]. Similar behaviour is observed for varying aspect ratios, confirming that the defect is invariant of the height. Bars less than 0.8mm are also found to be unstable and tend to bend during manufacturing due to their weak structural integrity [68].

2.3.4 Lattices

Low mass and high strength lattices of different unit cell types are common design studied for light-weight applications. Yan et al. [73] studied the manufacturability and mechanical performance of gyroid cellular lattices . The study shows that lattice structures with unit cell size from 2mm to 8mm with a volume fraction of 15% were manufactured with no deformations. It was found that the relative density decreased from 99.5% to 90.6% when the unit cell size increased from 2mm to 8mm. The low density was due to the presence of pores, which were larger and maximum in amount in the 8mm part. On the other hand, the parts with smaller unit cell sizes experienced maximum balling and powder particles bonded to the surfaces [73].

Zanini et al. [74] investigated the dimensional accuracy of additively manufactured strut lattices that have both vertical and horizontal struts of diameter 0.4mm. They concluded that vertical struts have sizes closer to the nominal (design) values compared to the horizontal features, as the vertical features were parallel to the build direction and self-supported.

Geometries	Defects/Flaws	Phenomenon	Ref.
Thin Walls/ Thin Structures	Warpage/ Dimensional Intolerance	Lack of heat conduction through surrounding powder. Short scanning vectors can also induce overheating in localized regions to cause warping.	[3]
	Porosities	Combination of loose powder adhering to surfaces and excess heat energy accumulation causing porosities.	[66]
	Surface roughness	Ineffective heat conduction through the powder, balling and partial melting of powder particles at the surface.	[3] [21] [66]
Unsupported Features/ Overhangs	Surface Roughness	• Balling due to inefficient heat conduction through the powder bed. • Adhering of powder particles to the downskin surfaces. • Higher energy input, dross formation and printing below certain critical angle worsen surface quality.	[21] [68]
Internal Channels	Surface Roughness/ Dross formation	Partial melting of loose powder particles on internal channel walls due to inefficient heat dissipation. Impact of these particles increases with channel diameter and also affects channels smaller than 3 mm.	[69] [68]
High Aspect Ratio Parts	Warpage/ Dimensional Intolerance	High aspect ratio parts are prone to higher heat stresses and low structural stiffness causing warpage and/or bending.	[21] [68]
Lattices	Porosity	• Greater number of pores are observed in larger struts, resulting in lower density. • Possibly attributed to long hatch vectors and poorer wetting.	[73]
	Dimensional Intolerance	Horizontal elements of lattice are more prone to deviation from nominal dimensions. Better conduction of heat in vertical elements causes lower warpage and better surface finish.	[74]
Thick parts/ Thin to Thick Cross sections	Warpage/ Dimensional Intolerance	Short scanning vectors and end-of-track vectors can cause severe overheating.	[3]

Table 2.1: Map of geometries challenging for LPBF, with their corresponding expected defects and a brief description of the phenomena causing the defect.

2.4 In-situ monitoring and control of LPBF

In-process monitoring and control systems have been developed and implemented to monitor that the key process parameters and process stability [18]. In-situ measurement and monitoring methods for LPBF have significant potential advantages over post-process inspection such as, early defect detection and real-time process control to potentially optimize the LPBF process parameters for improved quality and efficiency [11] [75] [17]. Experimental challenges including the restricted access to the process zone have led to the development of non-intrusive techniques, such as optical sensors and acoustic emission sensors, which can monitor the LPBF process without interfering with the process itself [76] [8]. Various techniques, including acoustic emission sensors, optical coherence tomography, X-ray computed tomography and machine vision, have been employed to monitor the LPBF process. Using the in-situ monitoring data coupled with machine learning can assist in efficient real time defect detection and take a step towards close looped monitoring system [77] [78]. By integrating these techniques together into the LPBF process control and optimization workflow, manufacturers can increase the reliability of the process, produce high-quality parts consistently, and enable its implementation the aerospace industry.

Grasso et al. [11] proposed a classification of different levels of in-situ monitoring in powder bed fusion processes. Level 0 includes embedded sensors in the PBF systems to keep the machine states and environment under control, e.g. oxygen sensors, pressure sensors. Level 1 refers to the measurements collected once or more per layer. These measurements mainly include, powder bed inhomogeneity and geometrical and dimensional variations of the printed slice. Level 2 includes measurement of laser beam interaction with the materials during the current layer, like the thermal history of the process and its by-products such as spatters and plumes. Level 3 refers to the measurements of the melt pool in the current layer. Level 4 refers to the measurements under the currently processed layer. It can include X-ray imaging, acoustic or ultrasound monitoring methods.

Radiative and non-radiative sensors measure parameters of the melt pool such as, temperature, size, rate of solidification, and the measured signals can be correlated with the quality of the printed parts. Cameras (Visible, near infrared (NIR), long wavelength infrared (LWIR)), optical coherence tomography (OCT), X-ray imaging, photodiodes and pyrometers are some of the radiative sensors used for in-situ monitoring in LPBF. Acoustic sensors, thermocouples, and displacement sensors are the commonly used non-radiative sensors used for in-situ monitoring [24]. However, thermocouples and displacement sensors are contact based.

Cameras are often used to capture images and videos during the printing of each layer in the LPBF process. Digital cameras are used to monitor the powder bed, typically taking images after the powder dosing and after laser exposure to identify the inhomogeneity in dosing of the powder and surface patterns every layer [75] [79]. Visible and NIR sensors have a wavelength between 400 - 1000 nm and are used to

monitor surface temperature [80], meltpool [12] [81], dimensional accuracy [82] and deformation [79]. Charged coupled device (CCD) and complementary metal-oxide semiconductor (CMOS) are often used in meltpool monitoring in LPBF [24] [83]. NIR and LWIR cameras capture images with wavelengths from 1000 nm to 1 mm. They monitor the process's thermal behaviour, maximum temperature and cooling rates [24]. The thermal images acquired from these sensors can be further analyzed to identify cooling rates [84], key hole porosity [85] and delamination [86]. In the optical monitoring methods based on cameras, illumination of the layer, field of view and the angle error are important factors in defect detection [79]. Additionally, for visible range, presence of heat source, spatter and small dynamic melt pool pose challenges which can be mitigated by using filters [24]. Other challenges associated with optical methods are the need for a continuous stream of images in order to capture useful information, appropriate frame rate selection, and necessity of image processing to extract information [9].

Photodiodes are used in LPBF for sensing thermal radiations and light emissions. They are semiconductors which convert photons to electrical current. Typical photodiode setups include two photodiodes, one which detects plasma emission with a wavelength 700-1050 nm and the second with wavelength 1100-1700 nm to detect thermal radiation [24]. Photodiodes have been successfully used to determine melt pool size, intensity and detect signs of overheating and balling in PBF [87]. However, photodiodes have slower response time with the increase in the surface area of the monitoring [88].

Pyrometers are another non-contact sensors to estimate the temperature from the thermal electromagnetic radiation in visible and infrared spectrum. They have been used in studies to detect overheating and predicting keyholes [24] and porosity [89] [90]. Pyrometers are typically used in combination with cameras to detect overheating and overhang layers [91]. OCT is another non-invasive technique that was proposed for monitoring surface defects in each layer [92]. In recent studies, OCT has been used in LPBF for meltpool characterization and morphology including keyhole depth [93]. X-ray imaging, particularly XCT technique has also been used to observe sub-surface meltpool dynamics, penetration depth and pore formation [11]. Zhao et al. [94] studied meltpool characteristics using in-situ X-ray imaging and diffraction and observer keyhole formation in detail. Paulson et al. [85] X-rays to detect subsurface porosity formation. However, it must be noted that all the work involving XCT for in-situ monitoring in LPBF is still under research and has been carried out with specialized equipment and custom LPBF builds. Integrating XCT based in-situ monitoring in commercial LPBF machines would be very challenging in comparison to other sensors [95].

Non-radiative sensors include acoustic sensors, thermocouples and displacement sensors. Acoustic sensors have the ability to detect sudden releases of energy which enable monitoring below the layer with the possibility to detect crack formations, detachment of supports or delamination [11]. Sensors used to detect acoustic sensors for in-situ monitoring include, microphones, solid-state acoustic detectors and

ultrasonic detectors [24]. Rieder et al. [96] demonstrated the use of ultrasound for the in-situ monitoring in LPBF to qualitatively evaluate residual stresses. Ye et al. [97] also successfully used acoustic signals for LPBF to detect indications of balling, overheating and normal deposition. However, acoustic sensors are suitable for qualitative evaluation of defects and are sensitive to weak emission signals, high background noise and in-process vibrations [98] [88].

Despite the promise shown by various in-situ monitoring techniques, there is a need to bridge the gap between research and industrial implementation. Most monitoring techniques use multiple sensing methods together which are expensive, or even difficult to install on industrial machines [11]. Incorporation of high-end sensors and cameras in the LPBF can have prohibitive costs [99]. Large amount of data generated during in-situ monitoring also calls for efficient solutions to handle large datasets [11]. Additionally, the data generated during the monitoring poses another challenge in terms of further processing and computational challenges to extract useful information from raw data [9].

Table 2.2 summarizes the various levels of the in-situ monitoring systems, corresponding sensors and defects they can detect.

Levels	**Region of Interest**	**Measurements**	**Sensing methods/Sensors**	**Defect Detection**
Level 0	Machine states and environmental conditions	Ambient temperature, oxygen content, chamber pressure, inert gas flow	Pressure transducers, rake sensors, thermocouples, flow sensors, oximeters etc.	Process parameter variations
Level 1	Powder bed and slice	Surface topography, powder bed homogeneity, geometrical and dimensional features	Visible range imaging (cameras), blade mounted sensors, NIR/IR Sensors (photodiodes)	Powder bed anomalies, warpage/distortion of parts, overheating, volumetric flaws
Level 2	Scan track	Process by products, high speed emissions, thermal gradients	High resolution visible range and thermal cameras, pyrometers, airborne acoustic emission detector, long exposure imaging	Overheating, spatter, plume, balling, surface temperatures, overhang features, delamination
Level 3	Melt Pool	Melt pool morphology (shape, size, temp distribution, etc.)	Photodiodes, video imaging, optical emission spectroscopy	Melt pool instabilities
Level 4	Under the layer	Subsurface measurements	X-ray imaging, X-ray tomography, acoustic sensors, strain gauges	Porosity, keyholes, cracks, delaminations, warpage, support detachment

Table 2.2: Levels of in-situ monitoring in LPBF. Adapted from [11][24].

2.5 Ex-situ measurements of defects

Ex-situ validation particularly with NDE techniques of additively manufactured components is widely accepted to ensure efficient quality control and inspection without altering the changing the characteristics and initial state of the materials [100]. The application of NDE to metal AM is crucial to validate, certify or qualify AM processes and components for aerospace service [101]. In the industry NDE techniques are prominently used in post process quality control and inspection. In research NDE techniques have been used to compare and correlate presence of de-

fects to observations in the in-situ monitoring [102] [103].

XCT is a method using X-ray projections on a component in 360° to capture 2D images which are images are stacked together to reconstruct a 3D model of the scanned component. This model provides data about the internal and superficial characteristics of the component which are not accessible to optical of contact systems [100]. Inclusions, porosities and surface roughness in metal AM parts have been measured using XCT technique. Schwerz et al. [16] have demonstrated detection of large spatter induced lack of fusion defects with in-situ monitoring and validated their presence through XCT. Klingaa et al. [70] have demonstrated internal surface roughness measurement of metal AM cooling channels using XCT. Lessuer et al. [14] have also used XCT to detect artificially seeded porosities in the metal AM components. Porosities bigger 30µm were detected using XCT, enabling further analysis of pore size, sphericity, and their distribution in the printed component [104] [105]. XCT is also a suitable technique to examine lattice structure artefacts [74]. Slotwinski et al. [106] used in-situ monitoring with ultrasonic sensors to detect porosity and validated it with ex-situ measurements using XCT.

3D scanning system consists of of an optical system with laser or light projection to capture the surface of the part being scanned [107]. The 3D scan data consists of a point cloud which can be converted to a mesh to compare with the CAD model [108]. This approach has been successfully used for inspection and quality control by measuring the geometrical deviation of dental crowns produced by metal AM [109]. 3D scanners are beneficial to scan surfaces of complex geometries and oversized aerospace parts [108]. Geometrical variations, warpages, and dimensional intolerances in as built metal AM parts are the defects which can be measured through 3D scanning. However, 3D scanning cannot capture internal features, and it is challenging to scan shiny, black or transparent surfaces and features of smaller resolutions [108].

Optical method of surface roughness measurement incorporates focus variation microscopy and is suitable for measuring areal surface roughness (Sa) of non-planar surfaces. Although tactile surface roughness measurement was prevalent for AM components, Triantaphyllou et al. [110] in their seminal study proved the applicability of the optical method for metal AM surface roughness measurement. The study concludes that areal surface roughness parameters (Sa and Sq) were sufficient to measure AM surfaces and the skewness (SSk) could be used to distinguish between upskin and downskin surfaces. It was also noted that reflective surfaces did not provide reliable readings [110]. Optical methods of surface measurements can be used to characterize the surface roughness and surface morphology of additively manufactured geometries [111] [112]. Charles et al. [113] used this technique to measure the surface roughness of downskin surfaces at 45° and 35° angles. They concluded that the 35° downskin surfaces showed higher surface roughness compared to the 45° surfaces due to large overheating and the powder particles adhering to the downskin surface at 35° [113]. Whip et al. [114] and Gockel et al.[115] also used the optical method to study the relationship between process parameters and

surface roughness. The study showed a correlation between high surface rouhgness and its detrimental effect on fatigue life of as built LPBF components.

Table 2.3 summarizes the defects and the corresponding NDE techniques which can characterize them.

NDE Technique	Defects Detected	Ref.
X-ray CT	Porosity, lack of fusion, cracks, dimensional deviation	[102] [103] [70] [14] [104] [105] [95] [106] [74]
3D Scanning	Dimensional deviation, warpage	[109] [108]
Optical surface roughness measurement	Surface roughness (Sa), surface morphology	[110] [111] [112] [113] [114] [115]

Table 2.3: NDE techniques and defects detected by them. Adapted from [100] [101].

2.6 LPBF in aerospace

Historically, AM was used extensively for rapid prototyping and functional testing in the aerospace industry. However, since early 2000s in-flight use of AM parts has been noted [5]. Metal additive manufacturing, including LPBF, is being increasingly used in the aerospace industry to produce functional parts such as engine components, brackets, turbine blades, fuel nozzles, and heat exchangers, among others. Overall, LPBF also enables the production of unique and customized parts, and is suitable for low volume parts or obsolete parts [6]. With ongoing research and development, LPBF is expected to play an even greater role in the production of critical components for aerospace applications in the future.

Aluminium, nickel and iron based superalloys, copper alloys, titanium alloys and refractory alloys are some of the metal alloys used in metal AM for aerospace applications [116]. Aluminium alloys have been used to produce lightweight aerospace brackets with LPBF, however they have limited aerospace applications due to poor capabilities at elevated temperatures [5] [117] . Copper alloys are used in heat exchangers such as for liquid cooled rocket engines [118]. Refractory alloys produced with AM for high temperature applications are still under development, and can possibly used to produce thruster components and nozzles [119].

Inconel 718 (In718) and titanium alloy (Ti6Al4V) are commonly used metal alloys in LPBF for aerospace applications. Nickel superalloys including In718 are crucial to manufacture turbine blades, combustion chambers, casings, impellers, fuel nozzles and other high temperature applications [6]. In718 is a nickel based superalloy particularly chosen for exceptional properties at elevated temperatures [24]. Ti6Al4V has high strength-to-weight ratio, high corrosion resistance, and compatibility with

composite structures which makes it ideal for structural components in aerospace [120]. Turbine blades, components for cryogenic applications, brackets, landing gear components are among the few parts made with Ti6Al4V alloy in LPBF [5].

2.7 Inconel 718 in LPBF

Inconel 718 is one of the most commonly employed alloys for metal additive manufacturing. It is a precipitation hardening nickel-iron alloy that has outstanding strength, creep resistance, fatigue life at elevated temperatures (up to 700 °C); excellent resistance to wear, hot corrosion; good weldability [121]. Conventional manufacturing and forming of this alloy posses challenges like excessive tool wear and low material removal rates because of its high hardness and low thermal conductivity. This is a critical challenge for the manufacturing of complex parts which is mostly the case for aircraft components. Introduction of AM addresses some of these challenges and thus making it a crucial material development for AM, especially for powder-bed processes [121].

2.7.1 IN718 Microstructure and properties

The common phase configuration of Inconel 718 contains an austinite face centered cubic (FCC) matrix of γ composed of mostly Ni atoms, and other alloying elements randomly substituting other lattice sites [122]. The FCC matrix of γ is present with strengthening carbides and intermetallic phases are namely FCC $\gamma'Ni_3$(Al, Ti, Nb), ordered tetragonal γ"Ni_3Nb and fcc MX (Nb,Ti)(C,N) [121]. The presence of metastable γ' and γ" phases coherant with γ fcc matrix is the main strengthening mechanism (precipitation hardening) for this alloy. The microstructure of as-built AM Inconel 718 alloy is a supersaturated solid solution with non-equilibrium phases, micro-segregation and high residual thermal stress due to complex solidification and cooling process. The as-built microstructure contains brittle Laves phase and the δ phase which form because of the micro-segregation of Nb and Ti. The alloy should be solution heat treated to dissolve the Laves and δ phase and homogenize the Ti, Al and Nb distribution which helps effective precipitation and allows peak strength attainment in subsequent aging treatment [121]. The tensile and yield strength of the fully heat treated alloy significantly improve over the as-built condition, and is found to be between the cast and wrought versions. The creep properties of the LPBF as-printed alloy is inferior to the cast ones [122]. However, some studies have shown that the AM Inconel 718 have better creep properties and this is attributed to the different processing conditions [121]. Due to the presence of defects and poor surface quality, the fatigue performance of as-built AM Inconel 718 alloy is inferior to wrought Inconel 718 alloy. But with optimized parameter selection, combined with heat treatment and surface machining the performance can be superior to that of its wrought counterpart.

2.8 Titanium alloy (Ti6Al4V) in LPBF

Ti6Al4V, also abbreviated as Ti64 is an $\alpha + \beta$ titanium alloy with high strength, low density, high fracture toughness and excellent corrosion resistance [123][124]. It has become a popular choice for additive manufacturing processes, particularly LPBF [120]. Ti6Al4V is a commonly used to manufacture landing gears, bearing frames, rotating machinery, compressor discs and blades, cryogenic propellant tanks among other aerospace components [6]. Conventional manufacturing of Ti6Al4V is challenging due to its poor thermal conductivity, propensity to strain harden, and high reactivity to oxygen, which makes LPBF an attractive manufacturing technique aerospace applications [123]. Titanium is also notoriously difficult to machine and extremely costly to roll [125]. LPBF is used to produce titanium parts for the aerospace industry particularly due to lower buy-to-fly ratios (12:1) compared to conventional manufacturing by forging (25:1) [123].

2.8.1 Ti6Al4V Microstructure and properties

Ti6Al4V alloy consists of 6 wt%Al and 4 wt%V in Ti. Titanium is an allotropic element existing in two different crystal structures, α-Ti with hexagonal closed packed (HCP) array and body centered cubic (BCC) β-Ti. Al is the α stabilizer and V is the β stabilizer, hence Ti6Al4V maintains $\alpha + \beta$ dual phase at room temperature [123]. However, phase transformation of Ti6Al4V is strongly dependent on temperature history and cooling rates in the fabrication process [124]. Typically, homogenization is done above the β phase temperature (approximately 920-950°C) and then with deformation and recrystallization the β phase grain size is controlled to get lamellar microstructure [124]. When fast cooling from above the β annealing temperature, β is decomposed by a non-equilibrium martensite reaction instead of the $\alpha + \beta$ transformation. Thus, rapid cooling as observed in LPBF process, forms α' martensite phase through diffusionless transformation instead of the diffusional $\alpha + \beta$ transformation [123].

The mechanical properties of Ti6Al4V are dependent on its microstructure including the phases, size of grains, and the texture of prior β grains [123]. Among all the Ti6Al4V phases α' has the highest strength value [126]. However, it also has low plasticity. Martensitic α' is a non-equilibrium phase and has deformed lattice structure which incurs lattices strains and it also has a high density of dislocations which results in dislocation strengthening. Hence, it is stronger than the $\alpha + \beta$ phases [123]. Thus, the LPBF parts usually exhibit higher tensile strength but lower ductility [127]. The α lath thickness also has an effect on the yield strength and fatigue strength [124]. Increase in the α lath thickness increases the slip length and hence decreases the yield strength. Ti6Al4V LPBF parts built have a higher fatigue strength but lower fatigue toughness [123]. The fine α' martensite structure has a high density of dislocations and hence the dislocation strengthening effect is enhanced [123]. Fracture toughness of the LPBF Ti6Al4V can also be increased by annealing, which decomposes α' martensite structure and removes residual stresses

[128]. For $\alpha + \beta$ microstructure, fatigue performance improves as the size of α phase decreases. A 20% increase in fatigue strength has been noted as the thickness of the α lath decreases from 10 µm to 1 µm [124]. LPBF produces α' martensite lath structure with sizes ranging from 0.2 - 1 µm [123] [127]. A finer α' microstructure also affects crack initiation and propagation. Grain and phase boundaries impeded the localization of plastic slip, and in the $\alpha + \beta$, the localization of plastic slip prevails in HCP α phase. As the thickness of α phase decreases, resistance to long plastic slip bands increases, resulting in a higher resistance to fatigue crack initiation [123] [124].

3
Materials and Methods

This section describes the LPBF platforms, their respective monitoring systems, materials used, specimen designs, NDE techniques, sample preparation, build preparation and software used for data and image analysis. The manufacturing of the specimens were conducted in two different LPBF machines at two different locations. The specimens built with Inconel 718 alloy using EOS M290 LPBF machine were manufactured at Chalmers University of Technology (Gothenburg). The specimens built with Ti6Al4V alloy using RenAM 500Q Flex LPBF machine were manufactured at GKN, Filton (United Kingdom).

3.1 Materials

3.1.1 Inconel 718

The feedstock material used was vaccum inducted melted, argon gas atomised Inconel 718 (forAM718 15-45VG) virgin powder supplied by Hoganas AB. The powder composition (equivalent with the UNS N07718 and ASTM B637) and the particle size distribution of the batch was specified by the manufacturer, as mentioned in the Table 3.1. The apparent density was 3.94 g/cm^3 and hall flow rate was 15.6 s for 50 g of powder. The quality of the virgin feedstock powder was not evaluated.

	Inconel 718							
Elements	Ni	Cr	Nb	Mo	Ti	Al	Co	Fe
%wt	53.29	19.02	5.307	3.09	1.04	0.52	0.02	Balance
	Particle Size Distribution							
Particle Size	<15 µm			>45 µm			15 - 45 µm	
%wt	2.5			4.3			Remaining	

Table 3.1: Powder composition and particle size distribution of Inconel 718.

3.1.2 Ti-6Al-4V

The titanium alloy feedstock powder was electrode inert gas atomised Osprey Ti6Al4V Grade 23 powder supplied by Sandvik. This was a used powder. The powder composition and the particle size distribution was as descried in the Table 3.2. The apparent density was 2.32 g/cm^3 and the hall flow rate was 28.6 s. Investigation of

the feedstock powder was not carried out.

	Titanium (Ti6Al4V)								
Elements	Ti	Al	V	Fe	O	N	C	H	Y
%wt	89.8	6.0	3.9	0.19	0.104	0.0275	0.014	0.0028	0.001
	Particle Size Distribution								
Particle Size	<15 µm					>90 µm			
%	0.8 vol%					0.2 wt%			

Table 3.2: Powder composition and particle size distribution of Ti6Al4V.

3.2 LPBF machines

3.2.1 EOS M290

Manufacturing was carried out with a EOS M290 metal 3D printer which uses the LPBF technology. The machine uses a Yb-fiber laser energy source with a maximum nominal power of 400 W, laser beam diameter of 100μm, and a build volume of 250x250x325mm. A EOS HSS (hard) recoater blade was used for consistent layer thickness and ability to remove ejected spatter from the part surface. The build was carried out in argon atmosphere with oxygen content less than 0.1%. The build plate temperature was set at 80°C and a powder dosing factor of 100% was used.

The process parameters used in the experiment are modified values of standard EOS parameters for IN718 material (IN718_040_PerformanceM291_2xx) for a layer thickness of 40 μm [129]. The build parameters used to print In 718 in EOS M290 were as summarised in Table 3.3. The scan pattern used were stripes with width of 10mm and rotates at an angle of 67° between layers. The exposure order was against the gas flow.

EOS M290 Inconel 718 Parameters			
Layer Thickness	**Laser Power**	**Scan Speed**	**Hatch Distance**
40 µm	300 W	1000 mm/s	0.10 mm

Table 3.3: Build parameters for Inconel 718 on EOS M290.

3.2.2 RenAM 500

The manufacturing for the Ti6Al4V alloy was done on the Renishaw RenAM500Q Flex LPBF system. The machine has consists of a quad laser system of four 500W ytterbium fibre lasers with laser diameters 80µm and argon inert gas atmosphere in the build chamber [130]. The build envelope is 245x245x335 mm and a soft silicon recoater was used for this build. The parameters used for this study were the

standard Renishaw parameters as given in the Table 4. Only 1 laser was used for the study for ease of gathering monitoring data. Scanning pattern was against the gas flow. The build parameters for Ti6Al4V in RenAM500 Q flex are as summarised in the Table 3.4

RenAM 500Q Flex Ti6Al4V Parameters			
Layer Thickness	**Laser Power**	**Scan Speed**	**Hatch Distance**
60 µm	320 W	600 mm/s	95 µm

Table 3.4: Build parameters for Ti6Al4V on RenAM 500Q Flex.

3.3 Monitoring systems

3.3.1 EOSTATE monitoring suite

This automated monitoring suite consists of three type of in-process monitoring tools (PowderBed, Exposure OT, MeltPool) that provides real-time insights of relevant production and quality data [131] [132]. For this study, the analysis was done on the data from powder bed and optical tomography (OT) images only. As the analysis of meltpool data is laborious and its significance on the outcomes of this study is relatively unknown, it was not further investigated. The data captured during the process are from the sensors that includes photodiodes, thermal and optical cameras mounted either on-axis or off-axis of the laser beam path. These sensors collect emissions in the infrared, near-infrared and visible spectrum from the entire build platform during laser processing. Different filters are also used to block any unwanted effects from laser back-reflections [131].

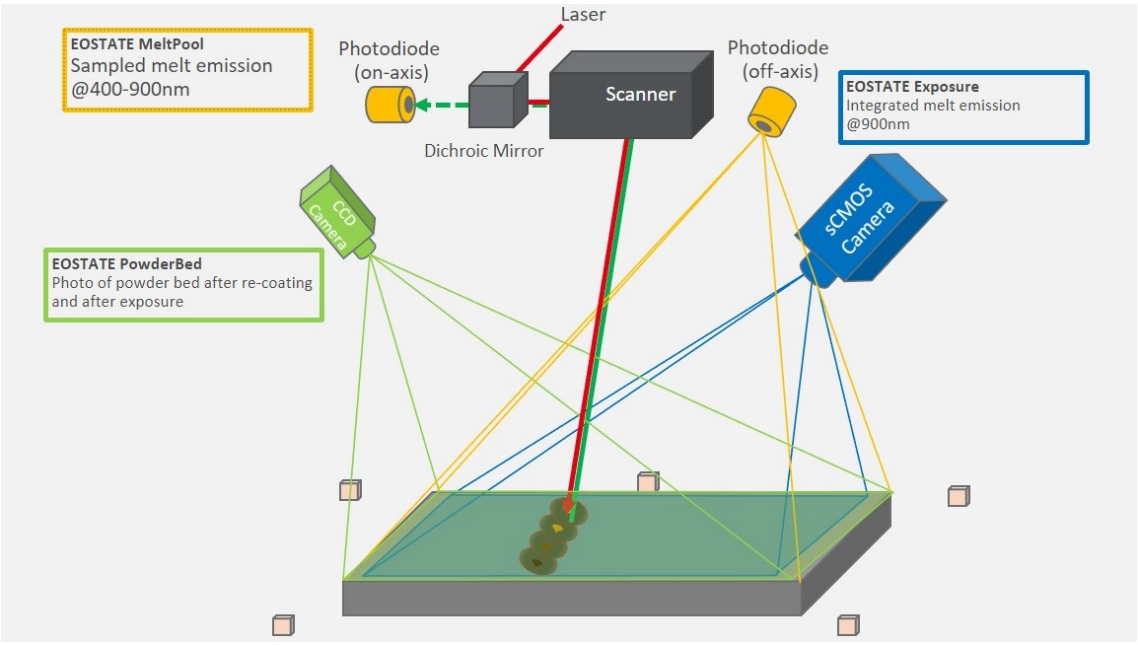

Figure 3.1: Overview of the EOS Monitoring System

3.3.1.1 PowderBed

The powder bed camera is mounted off-axis to the beam path and has sufficient optical resolutions to observe the entire build platform [131]. The camera records two images per layer, one after powder recoating (Figure 3.2a) and one after laser exposure (Figure 3.2b). These images, of dimensions 1280x1024 pixels, can be viewed during the process and can be exported for external analysis post build.

Figure 3.2: Images from the powder-bed camera (a) after powder recoating (b) after laser exposure

3.3.1.2 Exposure OT

The EOSTATE Exposure OT consists of a scientific Complementary Metal Oxide Semiconductor (sCMOS)-based camera, a thermal imaging camera, that captures near-infrared emissions of wavelengths near 900nm. The camera is mounted off-axis to the laser beam path and the construction of the system can be seen in figure 3.3. The output was in the form of high-focal depth images acquired 10 frames per second and combined into a single image at the end of every layer. The camera resolution is 2560 x 2160 pixels, with a spatial resolution of 125 μm/pixel across the build area [131]. The output image size is 2000 x 2000 pixels.

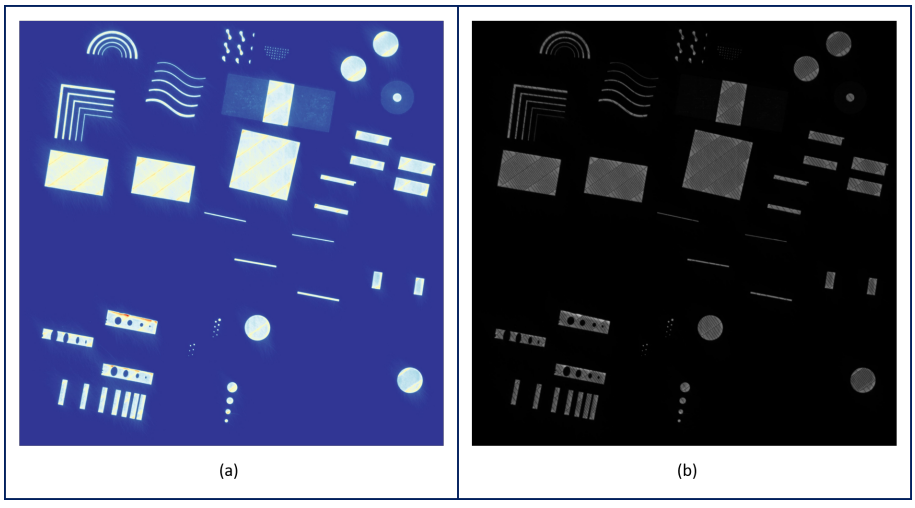

Figure 3.3: Images from the OT camera (a) RBG value (b) MAX grayscale value

The generated images were available in grayscale (Figure 3.3b) and color values (Figure 3.3a), both containing the same information that are visualized differently. The entire stack of images were exported as compressed tagged image file format (TIFF).

3.3.2 InfiniAM Monitoring Suite

The Renishaw proprietary in-situ monitoring software is known as the InfiniAM. It consists of the InfiniAM spectral software, LaserVIEW and MeltVIEW hardware to provide the feedback on energy input and emissions from the AM build process. The LaserVIEW and the MeltVIEW systems are collectively made of three photodiodes. Additionally, there is also a Layer CAM system to capture the powder bed images [130].

3.3.2.1 Layer CAM

The LayerCam system in RenAM500 Q Flex system is a digital camera which captures two images per layer. The first image is taken after the powder is dosed and the second image is taken after the laser scanning [130]. The powder bed images help determine anomalies and inhomogeneity in the powder deposition, warpage of parts, recoater damage. Powder bed images were used in the study to identify the parts which were deformed or warped and then correlate them to the ex-situ XCT and 3D scanning.

3.3.2.2 LaserVIEW

The LaserVIEW system in RenAM500Q employs a single diode system which captures laser intensities of each layer in the build. The photodiode for this system is embedded within the Fusion optical module and captures the filtered light passing through the fixed mirror without disrupting the laser beam characteristics. It records the wavelengths between 1050 nm to 1080 nm. Fig. 3.4 depicts the LaserVIEW system which operates in two modes[133]. The standard-speed mode captures the laser pulse during each layer at the rate of 100kHz. The second mode is the high speed mode, where the data is acquired at 2MHz. In this study the laser intensities are sampled every 20µs. The data is acquired in the form of text files containing the timestamps, coordinates, and laser intensities mapped to the three photodiodes for each layer. These text files are processed through Matlab to produce a low resolution image of each layer mapped to the corresponding laser intensities and indicates the regions with higher laser intensity.

3.3.2.3 MeltVIEW

The Renishaw MeltVIEW is an in-line opto-mechanical module system which monitors the emissions across a wide spectral range from the AM process. The system has an on-axis coaxial optical configuration which does not interfere with the laser beam and ensures that the meltpool remains in the field of view of sensors. It consists of two photodiodes to measure the plasma emission the infrared radiation.

The plasma emission is within the spectrum range of 300 nm to 700 nm and the meltpool radiation is within near infrared (NIR) spectrum of 700 nm to 1700 nm. The output from each photodiode is obtained as a DAT file for each layer which stores the information as a time series. This data is converted to a 3D visualisation of using the InfiniAM Spectral software as depicted in the Fig. 3.4.

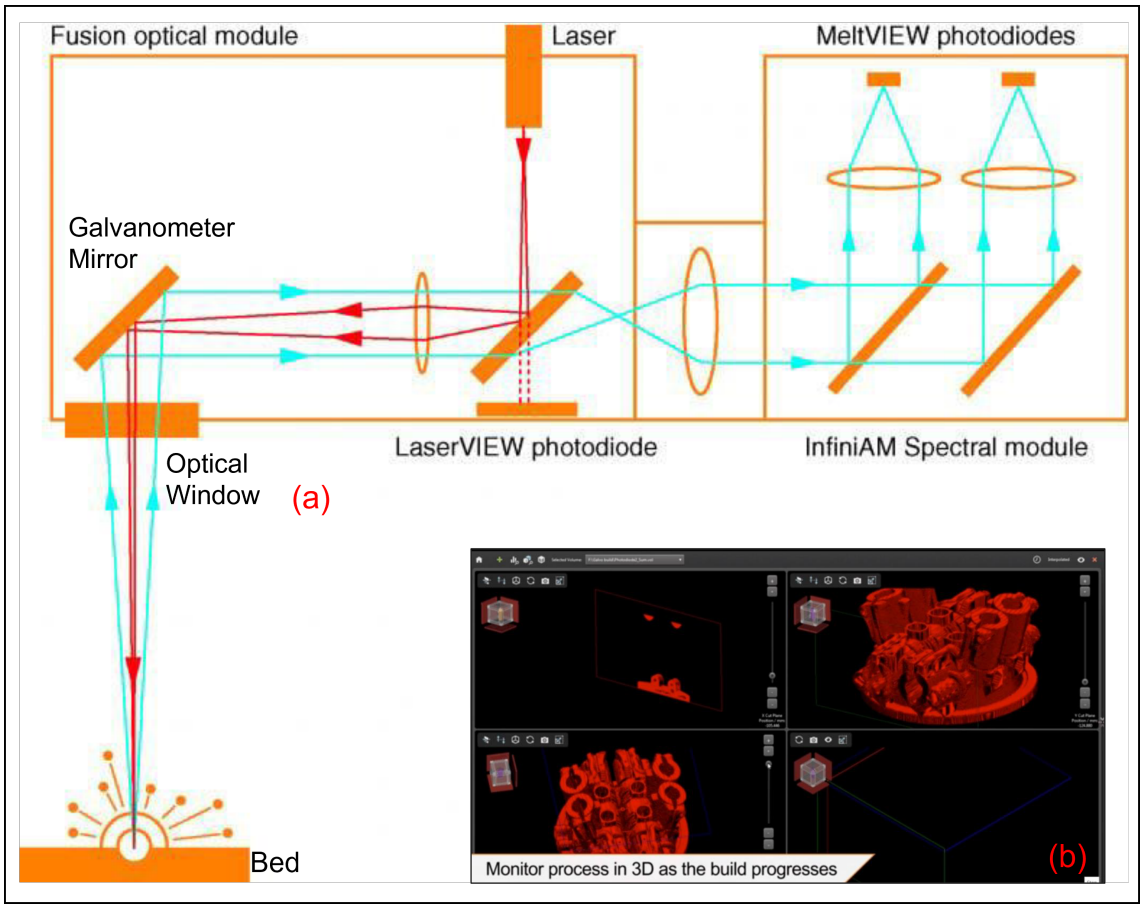

Figure 3.4: Part (a) depicts the schematic layout of the Renishaw InfiniAM monitoring system with LaserVIEW and the MeltVIEW systems. Inset image (b) depicts a screenshot from the InfiniAM Spectral Software with layer and 3D visualization of the printed part [133] [130].

3.4 Design of specimens

The design of specimens with challenging geometries was carried out in Autodesk Fusion 360 Computer Aided Design (CAD) software. The intent was to provoke geometry induced defects in the as built LPBF components. The challenging features in the specimens and their probable defects are based on the findings as described in literature review see Table 2.1. Table 3.5 and Table 3.6 summarize the specimens, dimensions and type of the features of interest and the probable defects they can provoke.

Part Name	Geometry	Overall Dimensions (LxWxH) (mm)	Features of interest	Possible defects
Large Artefact with internal channels		35 x 35 x 30	Internal Channel Diameter (mm) - 0.8, 1, 2, 3, 5, 7 Tubes Thickness (mm) - 0.3, 0.4 , 0.5 , 1	Dross formation on internal channels, Diemnsional deviation of internal channels, Warpage of thin tubes
Square (L shaped) thin walls		35 x 35 x 32.5	Wall Height - 30 mm Wall thickness (mm) 0.3, 0.5, 0.8, 1.0, 1.5	Distoration/ warpage of thin walls, Porosities
Semi-Ciruclar thin walls		17 x 32 x 32.5	Wall Height - 30 mm Wall thickness (mm) 0.3, 0.5, 1.0, 1.5	Distoration/ warpage of thin walls, Porosities
Curved thin walls	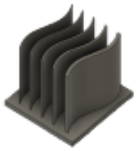	33 x 35.5 x 32.5	Wall Height (mm) - 30 mm Wall thickness (mm) 0.3, 0.5, 0.8, 1.0, 1.5	Distoration/ warpage of thin walls, Porosities
Overhang holes		5 x 20 x 30	Overhang Angles - 60°, 45°, 30° Hole Diameters - 1, 2, 3, 4, 8, 12	Distortion, geometrical deviation in holes
Thin Arch		22.48 x 20 x 19.22	Wall thickness (mm) EOS - 0.5, 1.0 Renishaw - 0.5, 1.0, 1.2, 1.5	Distoration/ warpage of thin walls, upskin/ downskin surface roughness
Angled Arch	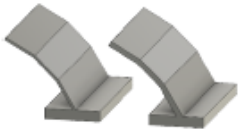	17.44 x 25 x 14.87	Angles - 60°, 45°, 30° Wall thickness (mm) 0.5, 1.0	Distoration/ warpage of thin walls, upskin/ downskin surface roughness
Hourglass	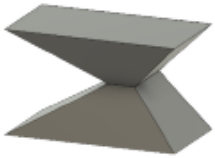	45.25 x 24 x 28	Face Angles - 90°, 60°, 45°, 30°	Upskin/ downskin surface roughness
High aspect ratio thin rods		4 x 32.5 x 10	1. Height - 15 mm Diameter (mm) - 0.3, 0.5, 0.7 2. Height - 15 mm Diameter (mm) - 0.4, 0.6, 0.8	Distortion of thin rods

Table 3.5: Challenging geometries for LPBF (a)

Part Name	Geometry	Overall Dimensions (LxWxH) (mm)	Features of interest	Possible defects
High aspect ratio thin rods		a - 4 x 62.5 x 15 b - 10 x 74.5 x 30	a1 - Height - 45 mm Dia (mm) - 0.4, 0.6, 0.8, 1.0 a2 - Height - 15 mm Dia(mm) - 0.6, 0.8, 1.0, 1.5 b - Rod Height - 72 mm Diameter (mm) - 2, 3, 4, 6	Distortion of thin rods
Thick Plate	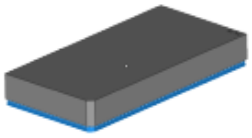	80 x 40 x 10	Thickness (mm) - 10	Distortion at the corners
Cross Lattice		15.3 x 17.5 x 7.5	Strut diameter - 2mm	Distortion in vertical and horizontal struts
Gyroid Lattice	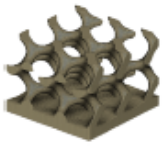	20 x 15 x 20	Strut size - 8 mm	Porosity
BCC X lattice	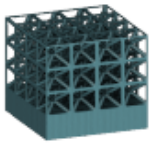	12.5 x 12 x 12.5	Strut size - 3 mm	Distortion
T section		65 x 15 x 15	Top thickness - 5 mm Cantilever length - 25mm	Warpage, overheat
Circular Section		19.95 x 20 x 14.88	Cross section diameter 20 mm (thick), 5mm (thin)	Warpage, overheat
High Stress Arches		20 x 15 x 34	Thickness (mm) - 2.5, 5.0, 7.5	Warpage due to residual stress
Bridges		5 mm bridge 11 x 8 x 5	Unsupported overhang (mm) 0.5, 1, 2, 3, 4, 5	Dross formation, Dimensional deviation

Table 3.6: Challenging geometries for LPBF (b)

3.5 Characterization

3.5.1 X-Ray Computed Tomography

In XCT, a specimen is placed between the X-Ray tube and the detector on a high precision rotating stage and projection images are taken until the object is fully rotated [134]. The X-ray source generates a conical beam of photons which penetrates the specimen and a detector records a 2D image [135]. The 2D image is a magnified penetration image of the specimen generated by the cone beam. The magnification is inversely proportional to the distance between the source and the specimen, i.e. the closer the specimen is positioned to the source the higher the magnification [135]. The 2D images are stacked together to reconstruct a 3D model of the scanned component which provides data about the internal and superficial characteristics of the component which are not accessible to optical of contact systems [100]. The stacked 2D images provide information about the scanned components in the form of volumetric pixel known as voxel. The resolution of these voxels determines the minimum size of the defect detectable. The reliability and sensitivity of this method is dependent on various factors, including the voxel size, penetration of X-rays into the material, absorption density of the material, scattering effects and component size and/or thickness of the geometry [135] [95]. Despite these constraints XCT is a reliable NDE technique to characterize the internal and external defects of the component. In this study XCT was used to examine various geometries for porosity, dimensional variation, and internal channel morphology.

This study used the Pheonix V|tome|x M300 X-Ray microfocus CT system, by Waygate Technologies to perform the CT scanning of the AM components. This is an XCT scanning system with dual tubes for microfocus and nanofocus. The microfocus has a maximum voltage of 300 kV and nanofocus has 180 kV [136]. The voxel size was about 20µm and hence the minimum detectable defects are approximately 60µm. The microCT parameters used for the IN718 alloy were 220 kv, 90 µA, 18 W whereas the parameters used for the Ti6Al4V were 200 kv, 120 µA, 24W. Inconel 718 parts generated higher noise compared to Ti6Al4V parts due to higher density. Volume graphics software was used to reconstruct the 3D meshes of the scanned objects and also to examine the CT slices for defects. The locations of porosities, dimensional deviations, and other defects observed in the CT scanned specimens were compared with the observations in the in-situ monitoring systems.

3.5.2 3D scanning

3D laser scanning was carried out to measure the geometrical deviation on as-built parts and compare the data with the actual CAD geometry. High-speed scanning was carried out using an HP-L-8.9 laser scanner integrated in 6-axis Absolute Arm (Hexagon). The scanner is a non-contact measuring tool with sensor that captures details of the geometry from a stand-off distance. The laser sensor collects the geometrical data as millions of points which are stored in a point-cloud in the PC-DMIS software paired with the scanner (Figure 3.5a). The data was exported as

surface mesh to external software for 3D data evaluation. GOM Inspect Pro software was used to compare the mesh STL file with the nominal CAD geometry. The surface deviation on the actual part from the CAD geometry is obtained (Figure 3.5b).

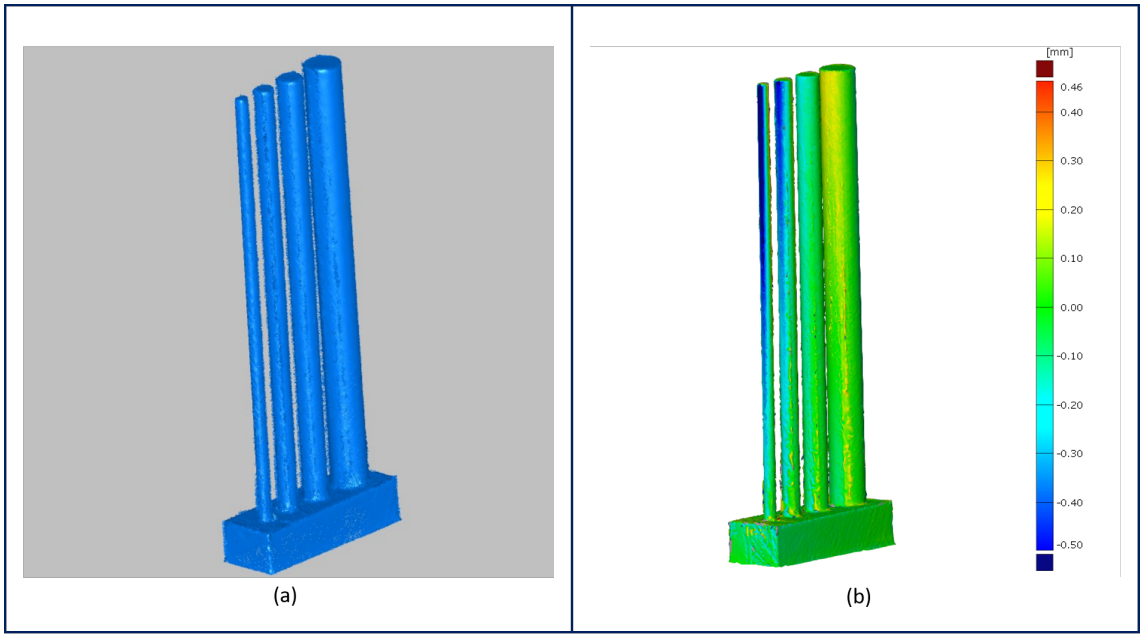

Figure 3.5: Inspection results of a thin rod specimen (a) as point-cloud data in the PC-DMIS software (b) as actual part-CAD comparison heat map

3.5.3 Surface roughness

Surface roughness measurement were carried out on samples, which were expected to have surface defects in critical regions. The surface characteristics were studied using a non-contact optical measurement sensor Alicona IF-SensorR25 with 10x objective magnification, minimum vertical resolution of 100nm, and minimum measurable roughness (Sa) value of 0.15μm. The measurement unit was paired with Alicona Measure Suite software. The scan area was set manually between two points, the sensor software then captured images in smaller rectangular areas within the set region and stitched them together into a complete optical colour image. In the software, the geometrical form of the specimen was removed to obtain a flat surface dataset. A real surface measurement was carried out on a filtered area large enough to represent the behaviour seen in the scanned surface (Figure 3.6).

Surface information such as average height (Sa), maximum peak height (Sp), maximum valley depth (Sv), Skewness of the selected area (Ssk) were generated in the report (represented as a histogram plot in Figure A.3). The average height, Sa, measurements were used as comparison to evaluate the surface roughness behaviour on different regions of the part.

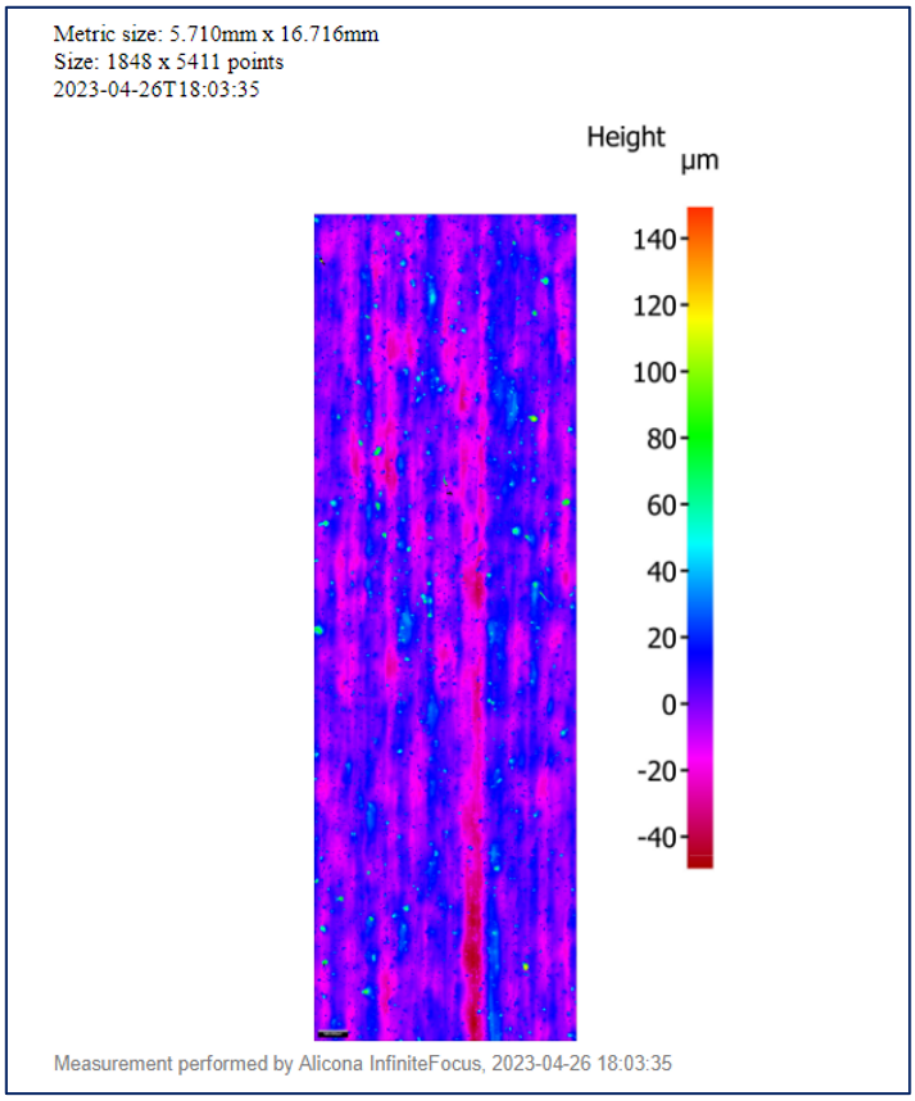

Figure 3.6: Results heatmap for surface roughness measurements

3.5.4 Sample preparation and metallography

The cylinder samples printed in IN718 and Ti6Al4V were cut across the laser tracks on the top layer to observe the meltpool depths. The samples were cut, ground, polished and mounted in MultiFast Red resin using the Struers Citopress. Both the samples went through the grinding with the MD Gekko and two stages of polishing on Struers Tegrapol-31 machine with MD Dac. In the last polishing step Oxide Polishing-A (OP-A) solution was used for the IN718 samples, whereas Oxide Polishing-S (OP-S) was used for Ti6Al4V samples. Between each polishing step samples were cleaned through an ultrasonic ethanol bath and further by using ethanol spray.

The IN718 was etched through electrolytic etching with 5% oxalic acid with HCl base. A fresh polish was used and the surface was kept wet during etching. The specimen is immersed in the etchant solution face up. The carbon cathode is placed

about one inch away from the specimen and the anode can be hovered just above the specimen or brought in contact with it. Voltage of approximately 6V is used. The Ti6Al4V specimen was etched by swabbing the surface with the Keller's Reagent and then washing under running water and rinsing with ethanol. Metallographic analysis was done using the Zeiss Axioscope 7 Light Optical Microscope (LOM).

3.6 Simulation and build preparation

3.6.1 Simulation

In order to gain more insight on the warping behaviour of a thick plate (Refer Table 3.6) that was to be studied for residual stress in the EOS build, a build simulation of the part was carried out on Simufact Additive software using the material and process settings parameter similar to what was used in the build. Design of different support structure were used in this simulation experiment to ensure that sufficient warping is observed during the printing process.

3.6.2 Build preparation

The build preparation and the orientation and position of the parts on the build plate for EOS M290 (Figure 3.7a) and RenAM 500 (Figure 3.7b) was made consistent with respect to the recoater movement and the gas flow in both the LPBF machines. Components with a higher possibility of failure were placed to avoid other components in the downstream and reduce the recoater influence in case of failure. Components intended for porosity analysis and metallography were placed closer to the gas flow inlet to avoid spatter induced porosity and defects [137].

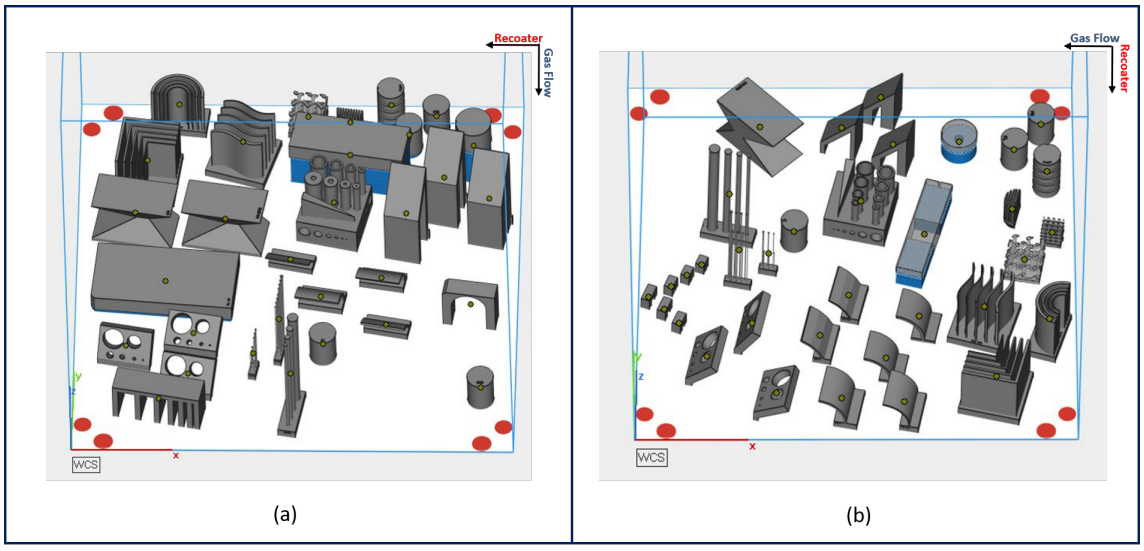

Figure 3.7: Build plate designed for (a) EOS M290 build (b) RenAM 500 build

Materialise Magics software was used to repair STL files, orient the parts, generate supports and make the builds for EOS and Renishaw machines. EOSPRINT is the

proprietary Computer Aided Manufacturing (CAM) tool that with the EOS M290 machine. EOSPRINT was used to import the build preparation data, position in the machine build plate, and prepare the build by selecting process parameters. These parameters included laser power, scan speed, layer thickness, hatch distance, scan pattern, scan direction, build plate temperature, feedstock dosing factor, recoater speed and gas flow rate. Each layer can be viewed as a slice with the chosen exposure settings on each part can be visualized as well. This gives an insight on what happens during the printing. QuantAM is the proprietary file preparation and build preparation software tool for Renishaw AM systems. The build made in Materialise Magics was transferred to QuantAM for the printing in the Renishaw AM 500Q flex machine. All the printing parameters are fed into the QuantAM software. The laser path can also be viewed slice-by-slice in QuantAM.

3.7 Data analysis

The data analysed in this thesis were in-situ monitoring images from EOSTATE, powder bed camera images from both LPBF systems, and laser intensities for each layer on the Renishaw AM500Q in the form of text files. In-situ monitoring images were analysed using the ImageJ and Fiji open-source image analysis software. Python Code was used to compare powder bed camera image pairs and compute their RMS values. Matlab code was used to generate a heatmap of the laser intensities mapped to their corresponding X-Y coordinates as registered in the text file for each layer obtained from the Renishaw AM500Q LPBF system.

3.7.1 Image analysis

ImageJ and its variant Fiji were the open-source software used for image analysis. Images from in-situ monitoring systems, powder bed camera were analysed in this software. This software allows image processing operations such as cropping, thresholding, rotating, contrast etc. This software also allowed stacking of images to form an animation of the image slices from the monitoring system. Fig. 3.8 depicts thresholding mask applied to an EOSTATE OT grayscale image of a part.

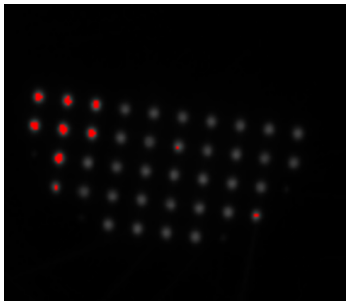

Figure 3.8: Example of an image acquired from the EOSTATE OT system with thresholding mask applied in ImageJ.

3.7.2 Renishaw Spectral Images

Matlab code was used to process the Renishaw in-situ monitoring data received in text file format. These text files store data in form of timestamps, X-Y co-ordinates of the laser beam on the build plate and corresponding laser intensities for each layer in the Renishaw build. The Matlab code (Appendix A.1) processes the data in the text files and generates heatmaps for each of the layers of the Renishaw LPBF machine. The code script uses the following functions: 'importdata' to load the text files, 'imagesc' for creating the heatmaps and 'saveas' to save the generated heatmaps as Portable Network Graphics (PNG) image files.

The script defines the parameters like size of the build plate, desired resolution of the output PNG image and the cut-off value of the laser intensities. The text files are all stored in the same directory as the code file and the code reads each layer file in the chronological order. For each layer the, a new figure window is created and, the heatmap is displayed using the 'imagesc' function. The 'cut-off' parameter is used to determine the maximum laser intensity in each layer. The resulting heatmap is then stored as PNG image and labelled according to the layer number, resolution and cut-off value.

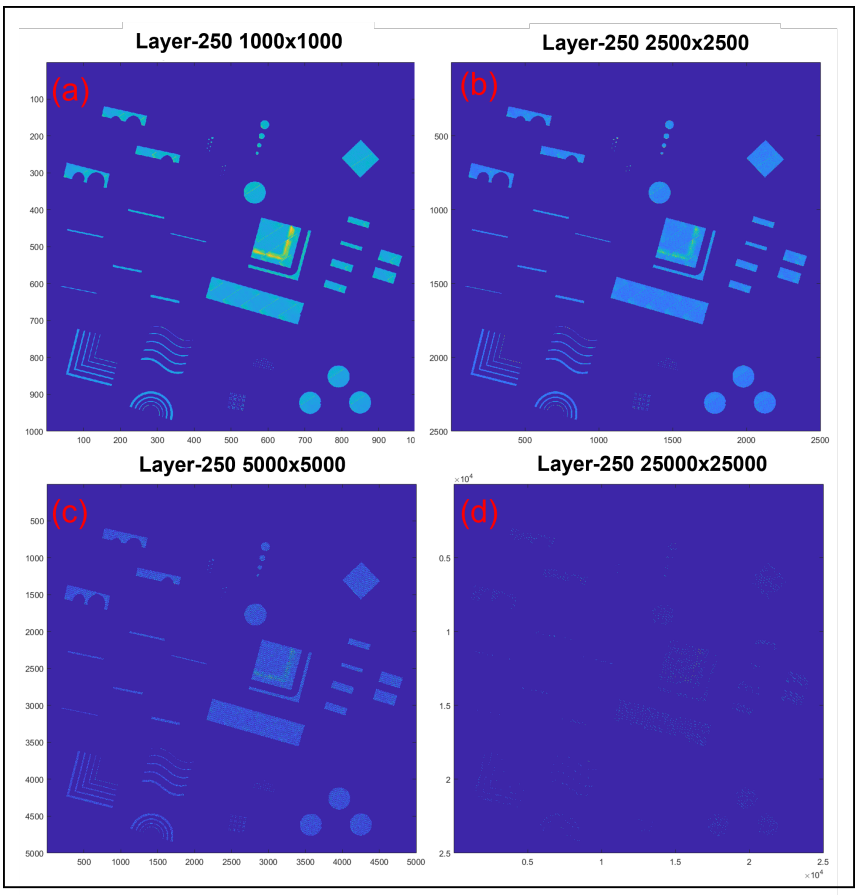

Figure 3.9: Figure depicts the same layer with different resolutions (a) 1000x1000 pixels, (b) 2500x2500 pixels, (c) 5000x5000 pixels and (d) 25000x25000 pixels.

In short, the code provides a visualization of the laser intensity distribution across the whole build plate of the Renishaw LPBF process. Fig. 3.9 depicts the Matlab generated heatmap in various resolutions for layer 250. The yellow spots in the image depict the areas with higher laser intensity or hotspots. The code averages the laser intensity values over surrounding pixels and then depicts them and additionally as the system captures the data every 20µs there are several areas in the map which are seen empty at 25000 pixel resolution, Fig. 3.9(d). The Fig. 3.9(a) with 1000 pixel resolution gives the best result in terms of the actual process indications. This Matlab script was used to generate 1000 x 1000 pixel images of each layer from the RenAM 500 machine. The low resolution of the images made it challenging to identify hotspots in thin and smaller geometries. However, consistent indications were observed in the heatmaps even for these geometries.

3.7.3 Python

Python code was used to determine the anomalies in the powder bed camera (LayerCAM) grayscale images obtained from the Renishaw LPBF process. Due to the large amount of layers, manually analysing each layer for part warpage and powder bed anomalies after powder dosing was impractical. Python code helped automate the process. The objective of the code was to generate an interactive Root Mean Square (RMS) plot to determine the difference between consecutive image pairs of each layer. The code uses several python functions, including 'glob' for file handling, 'cv2' for OPenCV image processing, 'mpld3' for interactive plotting, 'numpy' for calculations, 'matplotlib' for visualizations, and the interactive plot was created as a Hypertext Markup Language (HTML) file.

The RMS difference between two consecutive grayscale image pairs is calculated by the 'rms_diff' function. This function reads the image files, converts them to grayscale, computes the pixel-wise difference and calculates the RMS value. The 'glob' function is used to compare the image pairs and calculates the RMS value for each pair. These RMS values are stored in the variable 'rms_values' and the corresponding image pairs are stored in 'image_pairs'. The lineplot is created using the 'matplotlib' library with the RMS values on the Y-axis and the corresponding image pairs on the X-axis. 'mpld3' function is used to plot an interactive plot which allows annotation of the particular image pair when the cursor hovers over a particular point on the RMS line plot. The complete code is provided in the Appendix A.2

In brief, the Python code automates the process of analysing the LayerCAM images in grayscale, compares the image pairs, calculates the RMS difference between image pairs, and provides a result in the form of an interactive RMS line plot. The visualization assists in finding the anomalies in the between the different image pairs of the LayerCAM. However, there is a shortcoming in this method; it can only detect a part protruding out of the powder bed (shown by green circles in Fig.3.10(b) and (c)) and does not provide satisfactory results for the powder packing errors, showed by red arrows in Fig.3.10(b) and (c). This shortcoming results due to the negligible shift in brightness related to powder packing errors. Fig.3.10(a) depicts a snippet

of the RMS plot with the annotated image pair Fig.3.10(b) and (c).

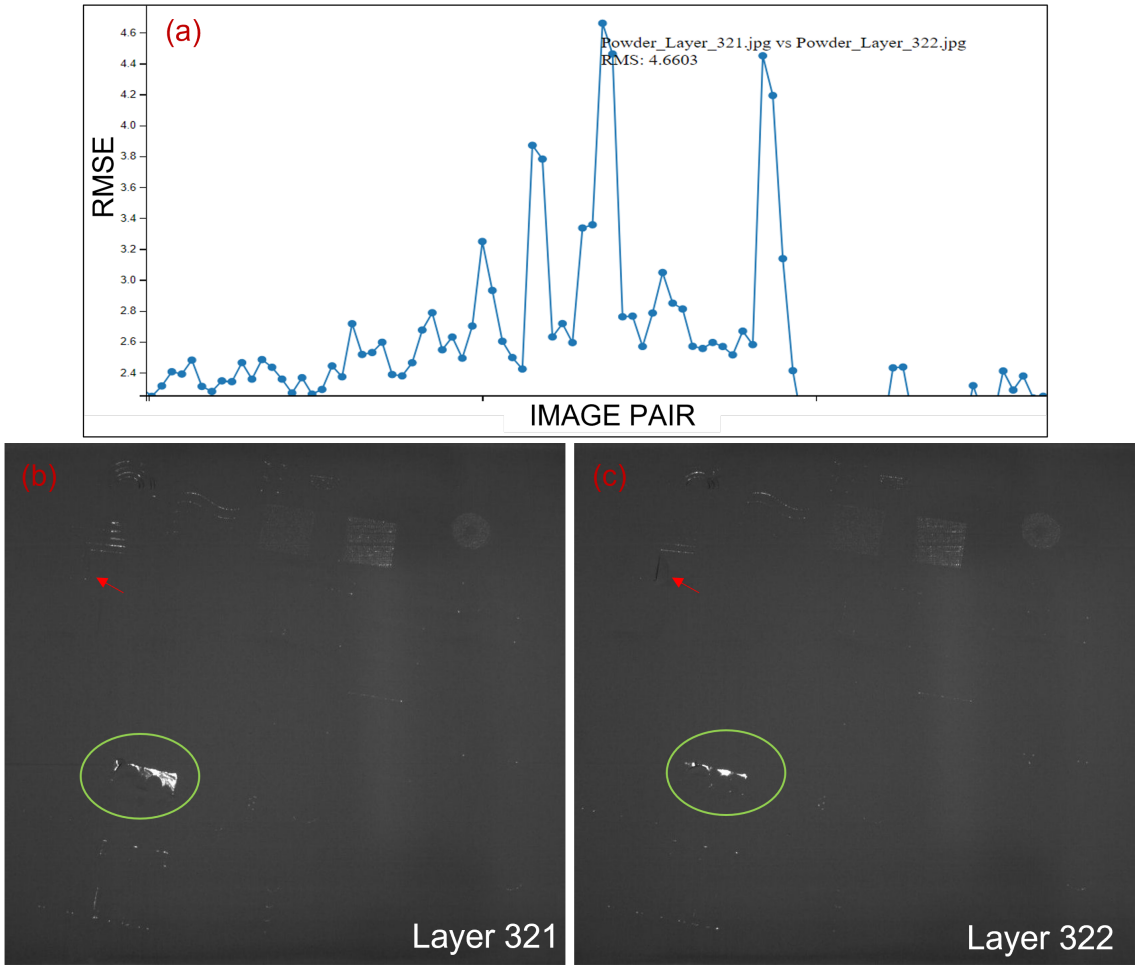

Figure 3.10: The figure depicts a portion of the interactive RMSE values plotted against the image pairs. The cursor and annotation on one of the peaks depicts the corresponding the image pairs. Image (a) and (b) show protruding part circled green, and red arrow show the powder packing error.

4

Results and Discussion

4.1 Build results

The IN718 material printed in the EOS M290 was intended to be printed upto 76.96mm height with 34 parts in the build. However, some of the intended geometries proved to be too challenging to build. There were several interruptions in the build due to the recoater crashes. The thick plate, thin wall colonies and the hourglass were responsible for the recoater collisions and crash. The original design of the bridge, with 8mm and 10mm unsupported bridges in IN718 were the eventual reason for a major recoater crash and subsequent build failure. The print was aborted at layer 566 at a height of 19.92mm. Among the 34 parts in the build, 16 were printed to their complete Z-height and 18 did not print to completion. The Renishaw AM500 Q Flex machine printed the Ti6Al4V material. It had 35 parts all of which were printed to their full Z height with 1366 layers.

4.2 Metallography

The meltpool measurements and the material characterization of the IN718 and Ti6Al4V samples were done according to the sample preparation method described in section 3.5.4. The intent was to measure the meltpool depth, estimate the density, observe the microstructure and assess the presence of porosity defects of the as built parts.

Cylinders were printed in IN718 and Ti6Al4V with the parameters listed in Table 3.3 and Table 3.4 respectively. A composite image (13.4 x 10.19 mm) of the unetched IN718 sample revealed presence of the spherical porosities. Lack of fusion defects and keyhole porosities were not observed, refer to Fig. 4.1. The morphology of the spherical pores match that of gas porosities [138]. The average meltpool depth for the IN718 specimen with the chosen parameters was 178.235 µm. The meltpool depth to layer thickness (40µm) ratio was 4.45, which is sufficient to produce dense parts with no lack of fusion defects. The chosen parameters are within the optimal processing window. This corroborates that the parameters selected for IN718 are robust and reduce the probability of parameter induced defects in this study.

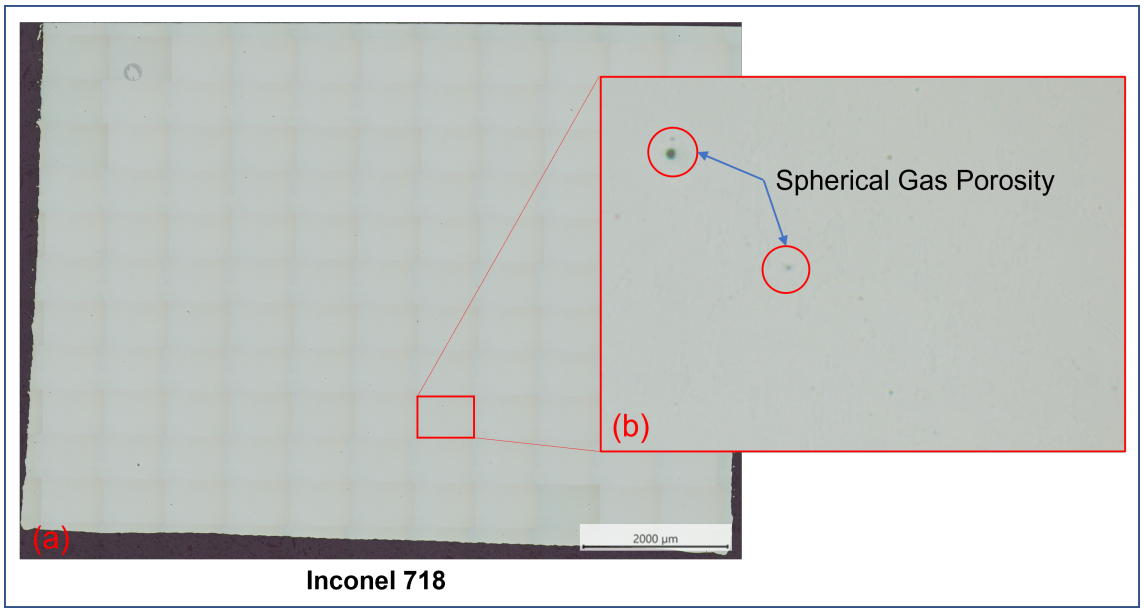

Figure 4.1: Spherical gas porosities as seen in the magnified image of the composite Inconel 718 unetched specimen.

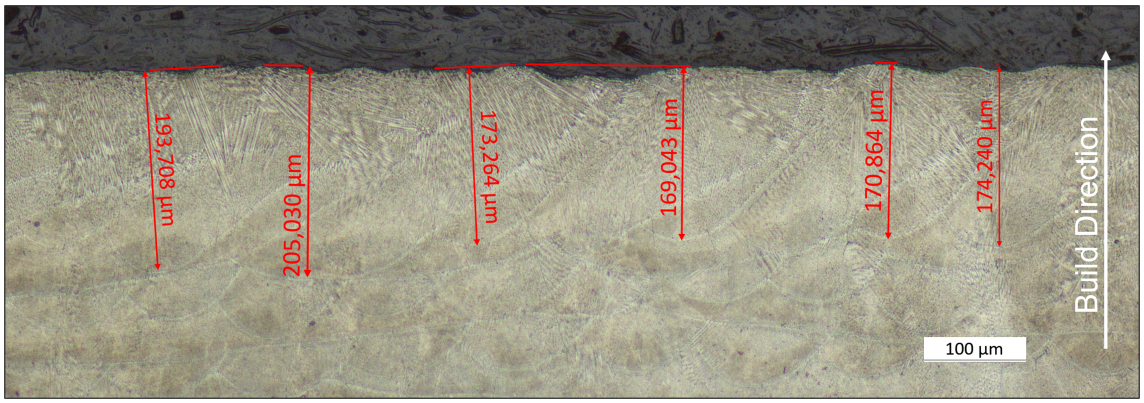

Figure 4.2: Meltpool depth for the selected parameters for Inconel 718.

The Ti6Al4V specimen was also prepared and etched as previously described. Some gas porosities were observed, but lack of fusion defects were not observed on the specimen. Although meltpool depth measurement could not be done as the etch did not reveal melt pool boundaries, certain correlations of the as built microstructure could be made to previous studies to corroborate that the parameters as described in Table 3.4 were sufficient for Ti6Al4V [123] [127]. As rapid cooling of Ti6Al4V alloy in LPBF produces α' martensite laths, similar laths were observed in the RenAM 500 prints as well. Fig. 4.3 shows the Ti6Al4V microstructure with α' martensite laths and the largest observed gas porosity of 15.143µm diameter (composite image size 12.46 x 10.93 mm) [123]. Density was calculated by analysing the unetched surfaces of IN718 and Ti6Al4V samples using ImageJ and the results are summarised in Table 4.1.

Material	EOS IN718 Selected Parameter	EOS IN718 Standard Parameter	Renishaw Ti6Al4V Standard Parameter
Estimated Density (%)	99.995%	99.960%	99.982%

Table 4.1: Estimated density of Inconel 718 and Ti6Al4V.

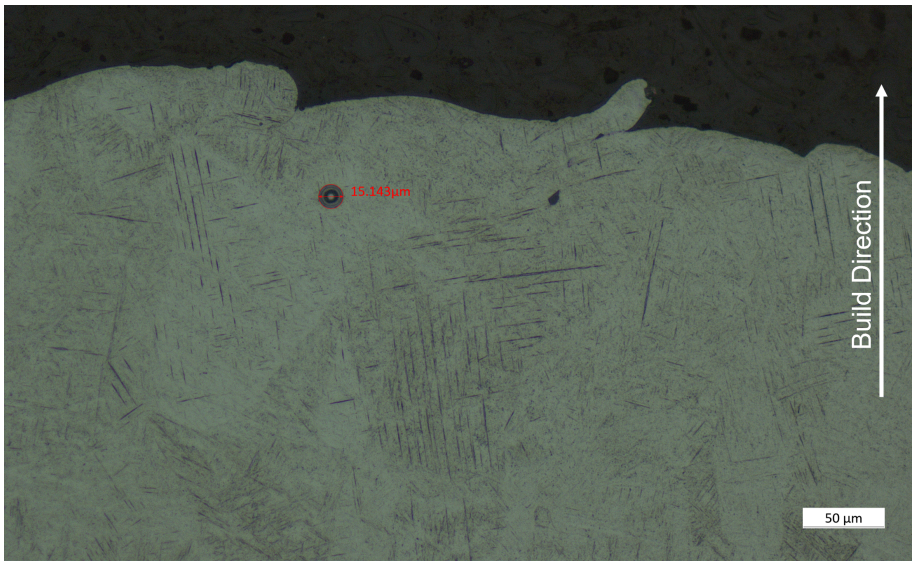

Figure 4.3: Gas porosity defect and α' martensite laths seen in the Ti6Al4V microstructure.

4.3 Anomaly detection, NDE observations and correlations

4.3.1 Thin wall geometries

Square (L-shaped), semi-circular and wavy thin walls (Table 3.5) in were printed in IN718 and Ti6Al4V with the intended height of 30 mm excluding the base. Thin walls in EOS (IN718) were completed only until partial build height due to build failure, whereas in RenAM 500 (Ti6Al4V) they were built to the complete height.

Hotspots were seen at certain locations in the square thin walls as shown in the pseudocolor image from the EOS OT systems in Fig. 4.4(a). The corresponding grayscale image is also shown in Fig. 4.4(b), with the hotspot having higher intensity than the rest of the image. Fig. 4.4(c) depicts the previous layer with part exposed and a powder packing anomaly. This may be a sign of protruding part edges due to distortion in the build direction [20]. The recoater collides with the protruding edges resulting in scattering of powder creating a powder packing anomaly [139]. The corresponding slice from the XCT, Fig. 4.4(d), depicts an area of damaged wall close to the hotspot. The hotspots are usually present in the areas of parts exposed in the powder bed after powder dosing. The exposed part in the powder bed with powder packing anomalies is a strong indicator of distortion of part in build direction.

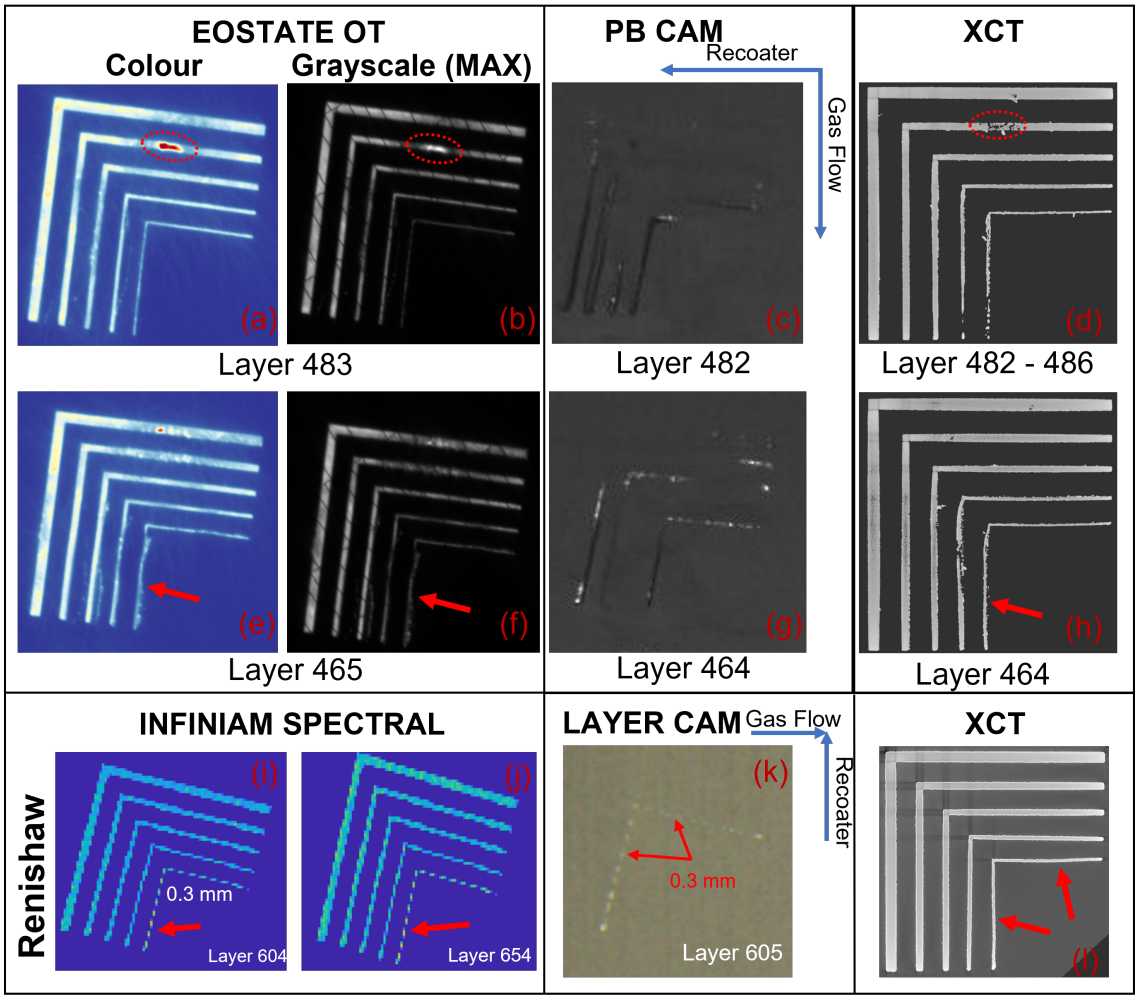

Figure 4.4: Hotspot in square thin walls in both the EOSTATE (a) (b) marked with red circle and in Renishaw InfiniAM (i,j). Distortions seen in EOSTATE OT marked with red arrows (e) (f). Powder Bed Camera images (c,g,k) and the corresponding XCT slices (d,h,l).

Similarly Fig. 4.4(e) depicts distorted elements of 0.3 mm wall in OT but hotspots are absent. In the previous layer 464 after powder dosing, a powder packing anomaly is shown, which probably occurred due to the recoater collision, refer Fig. 4.4(g) [139]. The walls of thickness 0.3mm, 0.5mm and 1 mm show a deformed outline, evident in the XCT slice of the same layer, Fig. 4.4(h). Thin walls perpendicular to the recoater movement appear to be relatively more deformed compared to walls parallel to recoater movement. A similar effect is seen in Fig. 4.5(a) where discontinuity in the thinnest wall is visible in the OT and is accompanied by streak marks and powder packing anomaly in the powder bed, Fig. 4.5(b). Streak marks on the powder bed may be caused by debris dragged by the recoater [140]. In this layer, these debris may have caused the recoater collision and subsequent deformation of the thin wall. Overall, visible distortion in OT, the protruding part in the powder bed and the accompanying powder bed anomalies correlate with the actual physical

deformation of the part as depicted in Fig.4.7(a). In the 3D scan to CAD comparison, Fig.4.7(a), deformations of the top of the walls are observed which corresponds to the layers with frequent recoater collisions as inferred from the powder bed images with powder packing anomalies.

Images from Renishaw monitoring also present hotspots on the 0.3 mm walls, Fig. 4.4(i) and their subsequent exposed areas in the powder bed after recoating, Fig. 4.4(j). XCT scan slice Fig. 4.4(l) shows the distortion which is confirmed by the 3D scan to CAD comparison as depicted in the Fig.4.7(b). However, in Ti6Al4V the recoater is not deemed responsible for the thin wall distortion as a soft recoater was used. It is possible that short hatch vectors for thin walls cause overheating and thermal distortion of thin walls [71] [141]. In both EOS and Renishaw monitoring systems, protruding edges of parts and subsequent powder bed anomalies after the powder recoating are consistent across the walls with distortion or deformation, and are a strong indicator of the vertical distortion of the part. Hotspots usually appear in areas which were previously exposed in the powder bed and on 0.3 mm walls possibly indicating overheating due to short hatch vectors. However hotspots alone do cannot indicate distortion, as further correlation from the powder bed images show that protrusion of the parts is always associated with distortion.

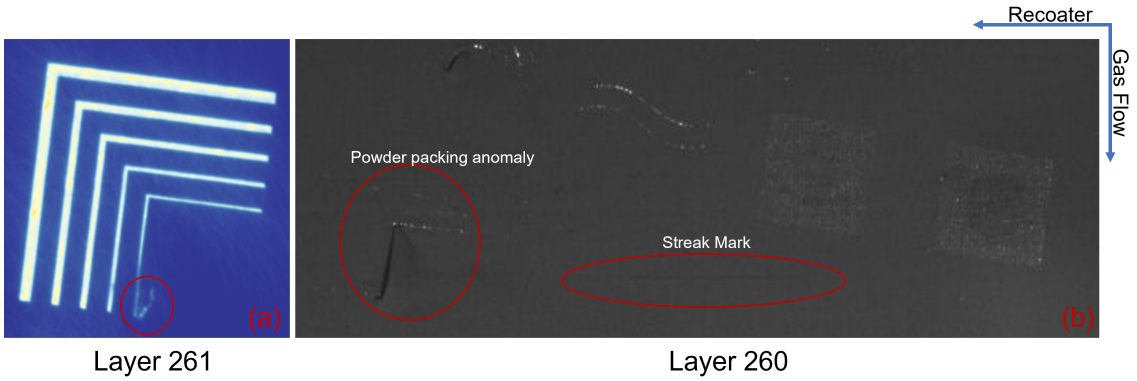

Figure 4.5: (a) EOSTATE OT image shows distortion of 0.3mm thin wall and debris present in layer 261. (b) Previous layer 260, shows streak marks and powder packing anomaly due to the recoater crash.

The upper layers in square thin walls presented visible voids in the XCT scan, Fig. 4.6. These voids are consistent across the walls parallel and perpendicular to the recoater direction. However, a measurement of the porosity sizes was not be made in XCT. In the upper layers of the walls, recoater collisions caused powder packing anomalies as seen in, Fig. 4.4(c) and (g). These powder packing anomalies are a potential cause for porosity formation and voids as seen in the thin walls XCT, Fig. 4.6 [20]. However, there were no direct correlations to the OT observations to the porosity.

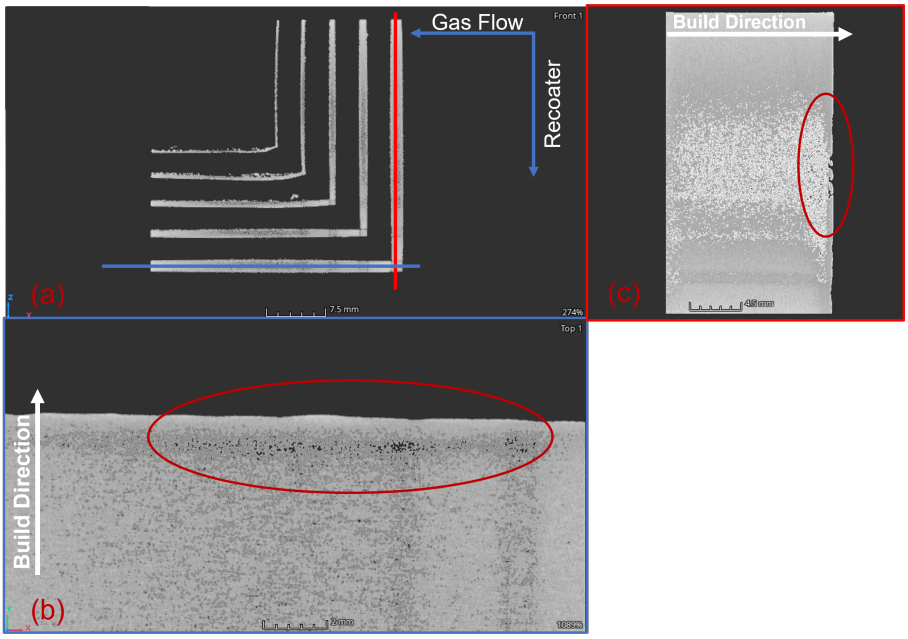

Figure 4.6: XCT slices depicting porosities in the upper end of the square thin walls (a) horizontal slice of the square thin wall, (b) Porosities in the wall perpendicular to recoater movement and (c) Porosities present in the wall parallel to recoater movement.

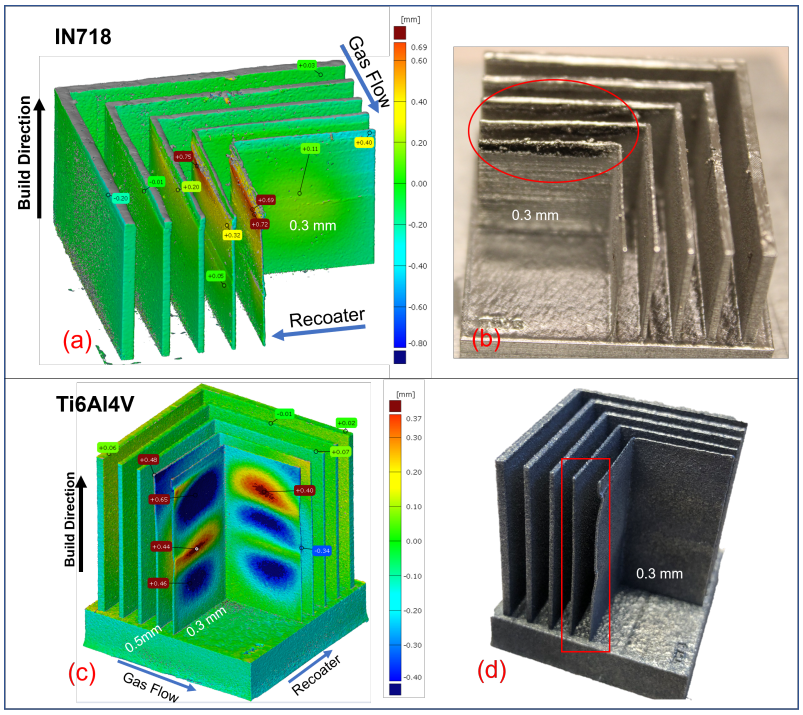

Figure 4.7: (a) describes the XCT scan mesh comparison to CAD for IN718 square thin wall with the distortions shown in red corresponding to the distortion and damage marked with circle in the as built part (b). Ti6Al4V XCT scan to CAD comparison (c) and the as built part with marked distortions (d).

The semi-circular thin walls showed a similar trend with the thinnest wall of 0.5 mm showing the maximum distortion 4.9(a). However, the circular thin walls in the IN718 were horizontally deformed in certain layers due to recoater collisions. Hence, several layers have hotspots and powder packing anomalies persistent in the layers prior. One such example is seen for layer 493 in Fig. 4.8(a), with the distortion visible in XCT slice too. No anomalies are observed in the OT images of the wavy walls but the thinnest walls of 0.3 mm and 0.5 mm thickness are exposed in the powder bed layer after recoating as shown in Fig. 4.8(a). This is likely an indicator of distortion in the build direction and subsequent protrusion of the part from the powder bed [20]. In Ti6Al4V hotspots are observed in the semi-circular and wavy walls of 0.3 mm and 0.5 mm thickness as seen in Fig. 4.8(b), similar to the square thin walls. These walls are also exposed in the previous powder bed layers. However, no anomalies are observed in the XCT measurements of these parts. Hence, the observations made in the monitoring data are similar to those seen in the square thin walls with distorted walls visible in the powder bed after recoating and accompanied by powder bed anomalies and hotspots are present on the thinnest walls. However, merely the presence of hotspots is not enough to confirm distortion, it further needs to be confirmed with the powder bed anomalies.

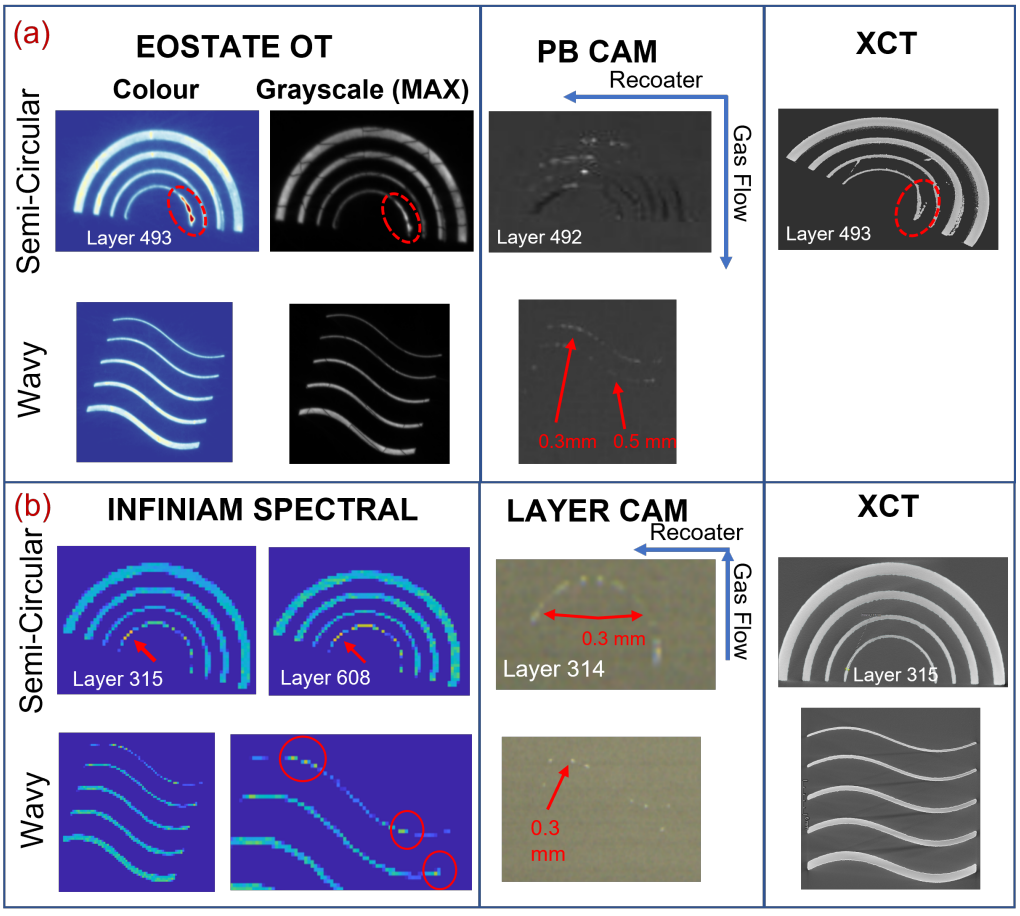

Figure 4.8: Circular and wavy thin walls observations seen in the monitoring, powder bed camera and XCT slice for EOS M290 (a) and Renishaw RenAM 500 (b).

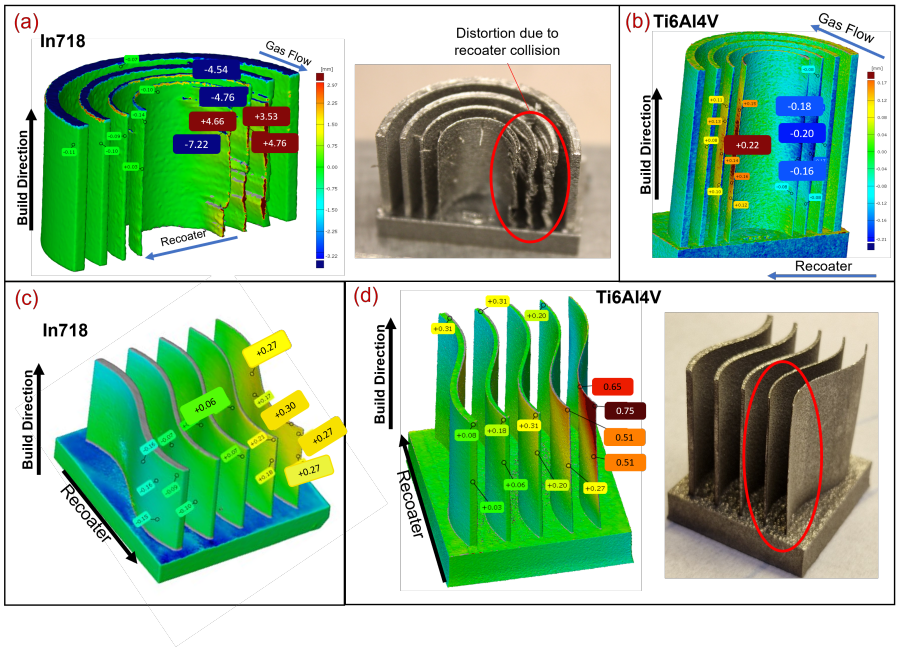

Figure 4.9: (a) Semi-circular walls printed in IN718, with XCT comparison to CAD with severe distortions due to recoater collisions. (b) Shows distortion in Ti6Al4V semi-circular wall compared to CAD. (c) and (d) depict the distortion for wavy thin walls in IN718 and Ti6Al4V respectively.

4.3.2 Hourglass

The hourglass specimen was printed with upskin and downskin surfaces with 30°, 45°, 60° and 90° orientation to the build plate surface. In IN718 two specimens of this geometry were printed with the objective to examine the effect of upskin and downskin parameters on the surfaces roughness. The parts were completed until a partial build height due to the build failure in IN718 and were printed with partial downskin surfaces as depicted in the Fig. 4.10. In Ti6Al4V, only one hourglass specimen was printed as the skin parameters were disabled by the manufacturer (Renishaw) and the build was completed successfully.

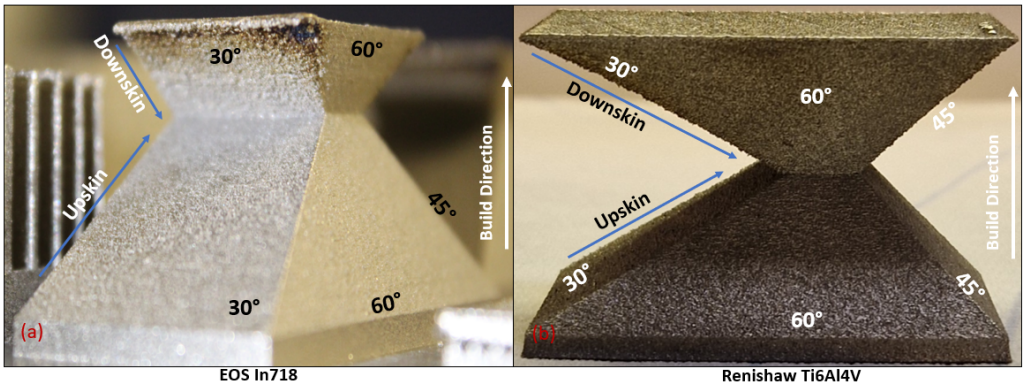

Figure 4.10: Hourglass specimen in (a) IN718 in EOS failed at height 22.60mm and (b) Renishaw in Ti6Al4V built to its full height

In both the IN718 and Ti6Al4V monitoring systems, no anomalies were identified in the upskin surfaces in the monitoring data. Contrarily, hotspots are visible on the 30° and 45° downskin surface angles at several instances as depicted in the Fig. 4.11. In the EOSTATE OT system the hotspots are visible on downskin surfaces irrespective of whether skin parameters are enabled or disabled. It was also noted that on the 30° downskin the hotspots are present at the end of both the short and long hatch vectors, Fig. 4.11(b) and (c). Dursun et al. [142] observed a similar effect in OT with hotspots on frequent hotspots on downskin surfaces lower than 45° inclination. Lack of heat dissipation induced by thermal insulation of powder underneath the overhang zones is the primary cause for the heat accumulation on the 30° downskin surface [142] [17]. This heat accumulation on downskin inclinations lesser than 45° manifest as hotspots in the in-situ monitoring as corroborated with previous studies [142] [17]. Fig. 4.12 from EOSTATE powder bed camera depicts 30° downskin side protruding from the powder bed. This matches the defect described as super-elevated edges which can cause powder bed anomalies [20] [25]. Super-elevated edges occur as a consequence of the overheating in overhang parts and scan strategies and it has further implications on the surface topology [25] [143].

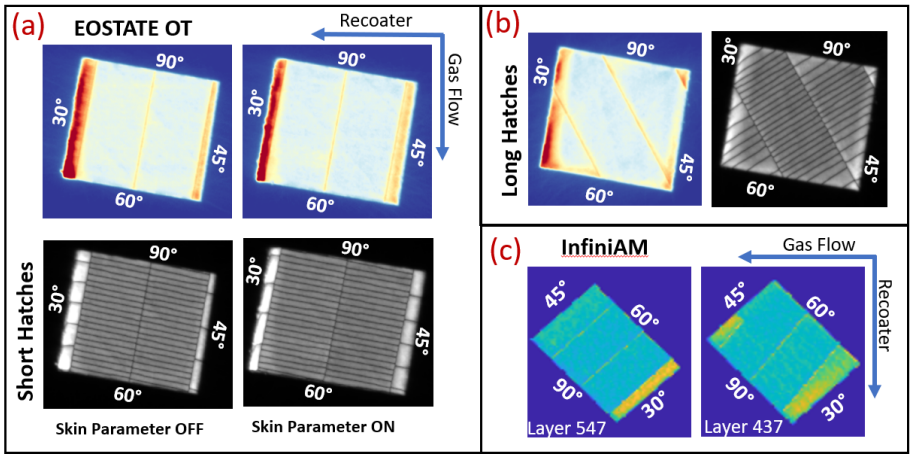

Figure 4.11: IN718 hotspots on hourglass on the 45° and 30° downskin surfaces with short hatch vectors with EOS Skin Parameter OFF and ON (a). (b) depicts the hotspots on 30° downskin on IN718 hourglass with long hatches. (c) Depicts Ti6Al4V layer 437 with hotspots on 30° downskin surface.

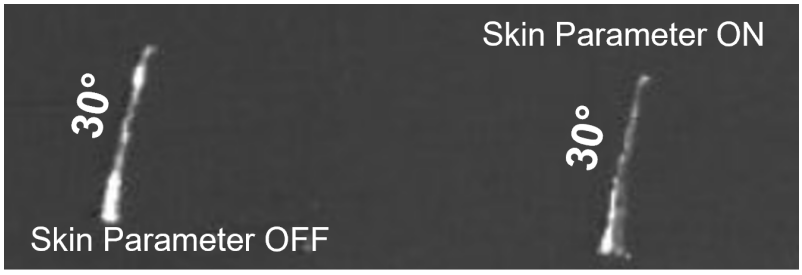

Figure 4.12: 30°downskin faces on hourglass part, peeking out of powder bed after powder dosing in EOS.

Surface roughness characterization of the part revealed that the average surface roughness (Sa) at 30° surface inclination was significantly higher compared to other downskin and upskin surfaces, see Table 4.2. Additionally, there was significant difference in the upskin to downskin surface roughness at 45° and 30° inclinations, see Fig. 4.13. In the Ti6Al4V hourglass specimen, the 30° downskin surface roughness worsens in the direction of the build height, Fig.4.15. All these observations confirm the findings by Dursun et al. [142], where downskin surface roughness increases with the decreasing inclination angle. Higher heat accumulation at the downskin surfaces promotes adhesion of powder particles on the downskin surface, and causes balling resulting in a rougher surface [144]. Staircase effect is also a significant contributor to the surface roughness and this effect is more prominent as the inclination angle decreases [3]. Thus, the hotspots seen on the downskin surfaces correlate to the low inclination angle of the downskin surfaces and the resultant heat accumulation below the overhangs.

Face Angle	**EOS Skin ON (IN718)**		**EOS Skin OFF (IN718)**		**Renishaw (Ti6al4V)**	
	Downskin	Upskin	Downskin	Upskin	Downskin	Upskin
(°)	(Sa)(µm)	(Sa)(µm)	(Sa)(µm)	(Sa)(µm)	(Sa)(µm)	(Sa)(µm)
90	5.62	5.71	5.62	5.89	14.47	16.30
60	42.82	8.97	42.82	9.59	38.57	19.70
45	10.45	6.28	10.45	6.16	21.51	16.55
30	65.40	10.82	65.40	8.77	57.21	26.94

Table 4.2: Average surface roughness (Sa) values on the upskin and downskin faces of hourglass.

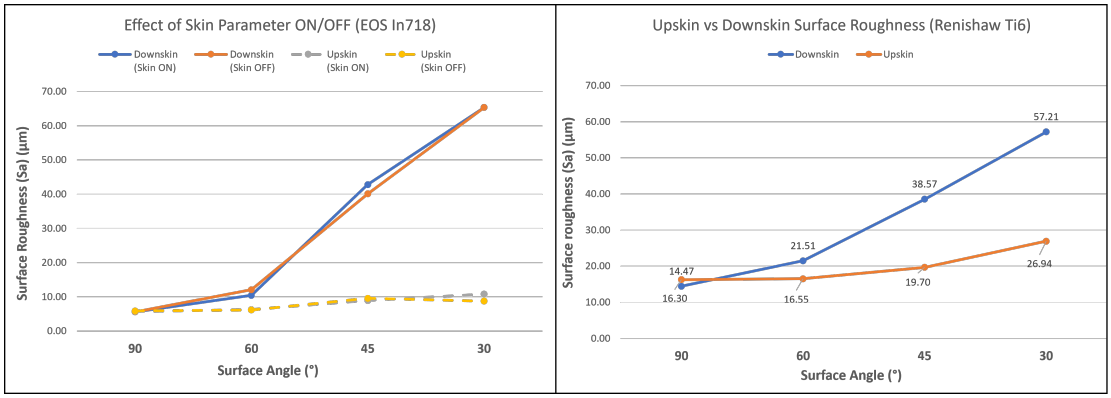

Figure 4.13: (a) Effect of skin parameter enabled and disabled on the surface roughness values in upskin and downskin surfaces in IN718. (b) Comparison of upskin and downskin surface roughness values in Ti6Al4V.

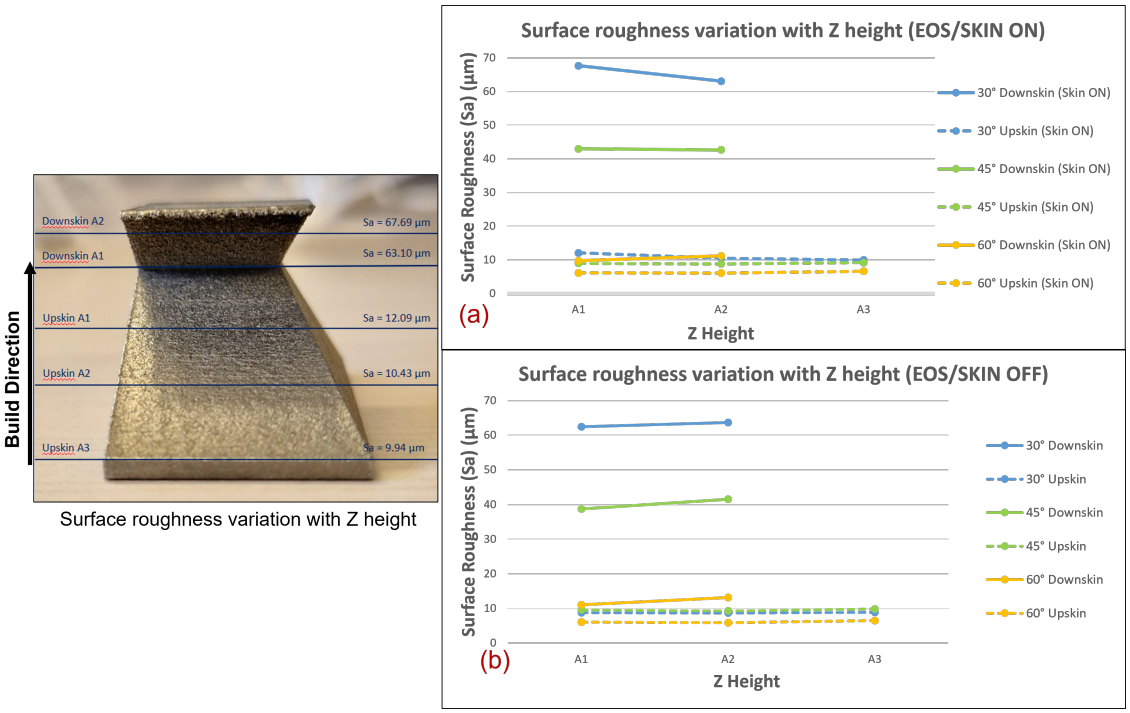

Figure 4.14: Effect of surface roughness with Z height increase in IN718 hourglass with (a) Skin parameters ON and (b) Skin parameters OFF

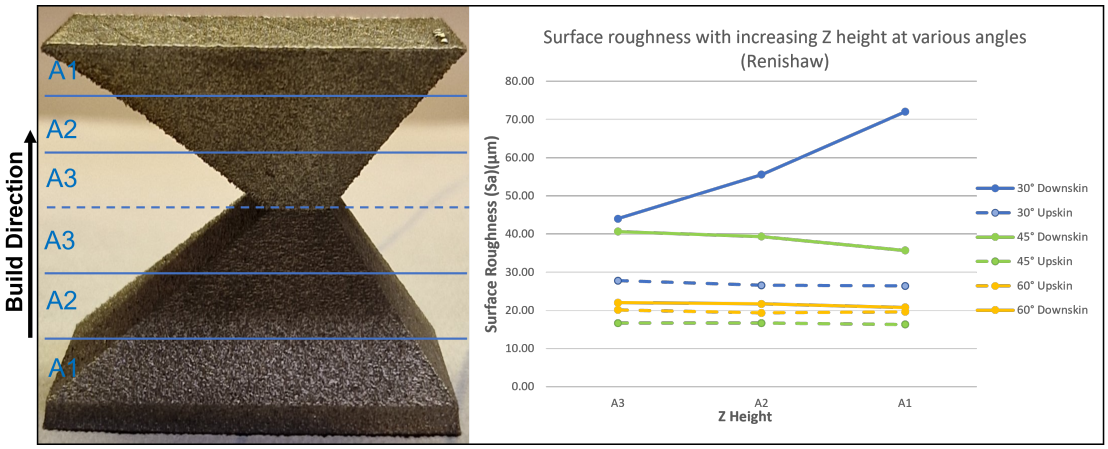

Figure 4.15: Effect of surface roughness with Z height increase in Ti6Al4V hourglass

4.3.3 Thin arches and angled arches

Thin arches and angled arches (Table 3.5) produced in IN718 and Ti6Al4V were evaluated in terms of surface roughness on upskin and downskin faces and 3D scanned to determine geometrical deviation. In IN718 the thin arches and angled arches were produced in 1mm and 0.5mm thicknesses. In Ti6Al4V the angled arches had thickness of 1mm and 0.5mm, whereas thin arches were printed with 0.5mm, 1mm, 1.2mm and 1.5mm thicknesses. All the parts were successfully completed to their

complete build height.

The majority of the layers of the thin arches were printed without any anomalies in the in-situ monitoring systems of both EOS and Renishaw. However, the top layers of the thin arches shows higher number of hotspots in both EOS as well as Renishaw as depicted in the Fig. 4.16 and Fig. 4.17. The intensity of hotspots in IN718 was higher in the layers with short hatch vectors as shown in the Fig. 4.18. Thin arches printed in Ti6Al4V also depicted hotspots on the top few layers, however their correlation to short hatch vectors could not be confirmed due to lack of hatch data and lower resolution of the generated heatmap. The top few layers in the arch correspond to the unsupported thin overhangs with low inclination angles. These hotspots are a possible indication of the excess heat accumulation due to the unmelted powder below with lower thermal conductivity [20]. Several layers on the top of the arches protrude from the powder bed after the recoating and are also accompanied by powder packing anomalies as seen in Fig.4.16. The packing anomalies indicate a possible recoater collision with the top layers of the arches [139]. The local overheating caused by low thermal conduction by the surrounding powder and short hatch vectors causes distortions of arches in the build direction which has been confirmed earlier by Jones et al [21]. Severe balling effect on the top of the overhangs may also cause recoater crash with the top layers of the arches [25]. This effect is seen in Fig. 4.19, where the top layers with surface defects collided with the recoater and resulted in the breaking off of the part. The distortion in the top layers of the arch as described by Jones et al.[21] is also evident in this study and is inversely proportional to the thickness, refer Fig.4.21(a).

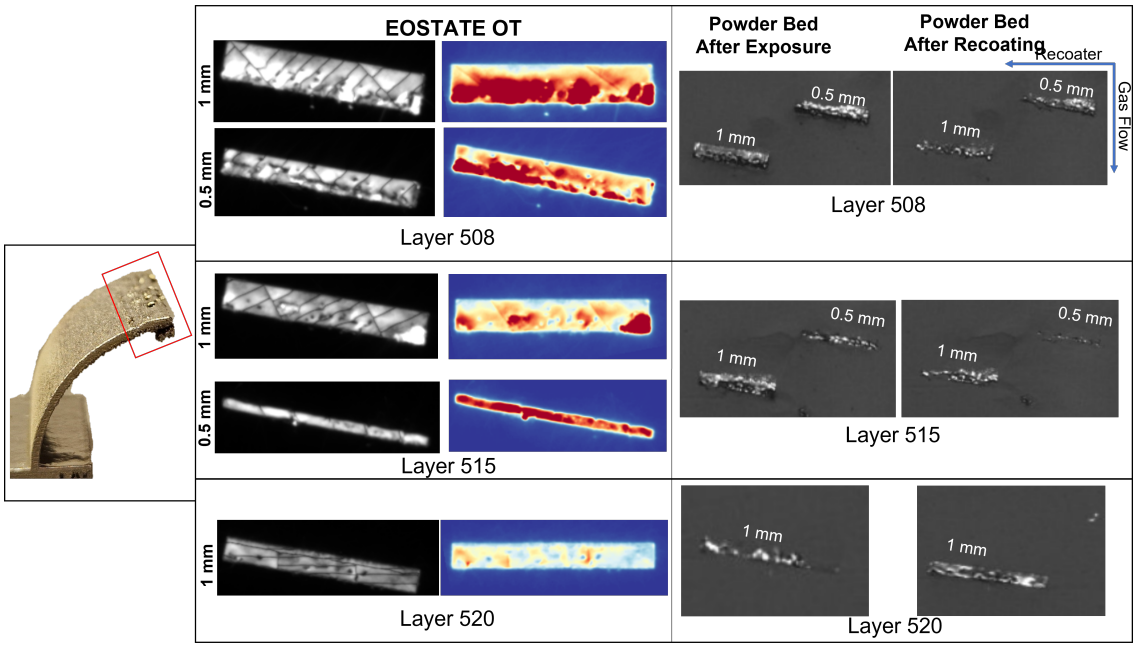

Figure 4.16: Hotpots on IN718 thin arches printed in EOS and their corresponding powder bed images.

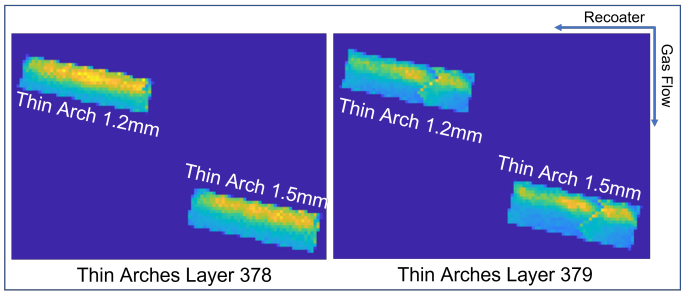

Figure 4.17: Hotspots observed on thin arches printed in Renishaw.

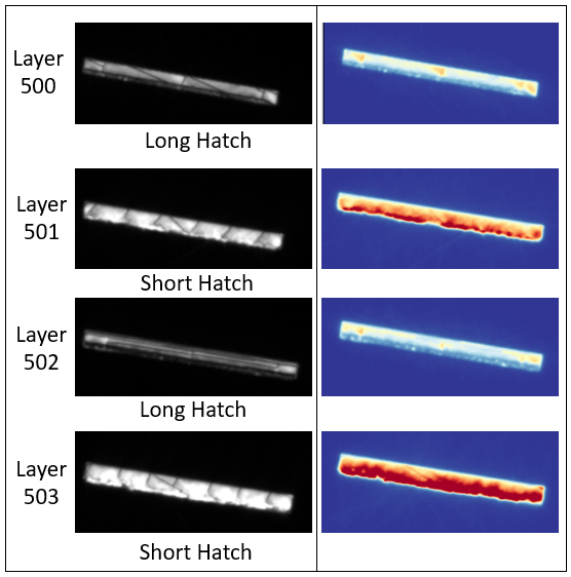

Figure 4.18: Alternate short and long hatching in and the appearance of hotspots on 0.5mm thin arch in EOS.

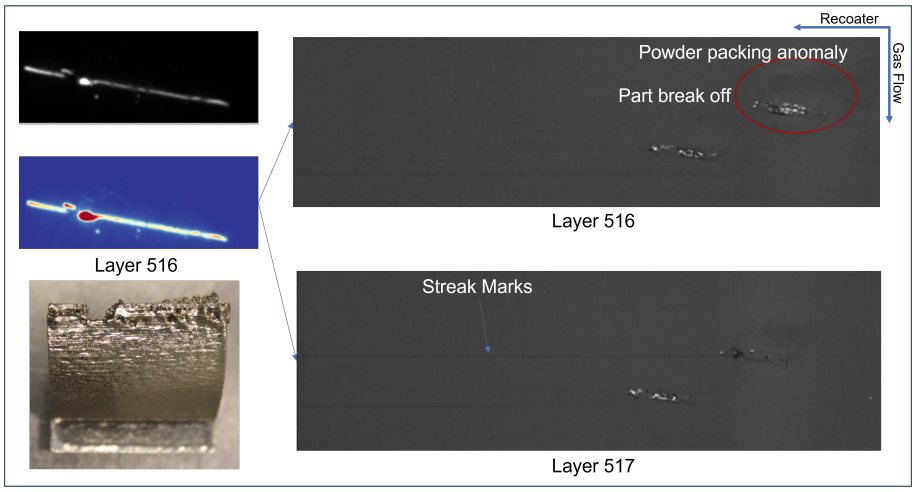

Figure 4.19: Part break away and the hotspot on the top of thin arch printed in EOS. Subsequent powder bed layer depicting the streak marks caused by debris from the damaged part.

Surface roughness characterization of the arches showed that overall the upskin surfaces had better surface roughness compared to the downskin surfaces. With the decrease in the inclination angle surface roughness increases for both upskin and downskin surfaces in the build direction, see Fig.4.20. The highest surface roughness is observed at the top layers. Higher surface roughness on downskin surfaces at the tip of the thin arches can be attributed to the heat accumulation that causes partially sintered powder to adhere to the downskin surface [144]. Severe cases may cause dross formation as seen in this study, Fig. 4.21(a) also known as infiltration effect [66]. This infiltration effect is more prominent than staircase effect at lower inclination angles [66] [145]. It is also possible that the effect of contour scan and hatch pattern on the upskin surface results in better surface roughness than downskin [144]. Thus the hotspots seen on the thin arches correspond to areas with severe surface defects like balling and infiltration. The vertical distortion in the build direction is correlated with the protrusion of the part from the powder bed and accompanying powder bed anomalies.

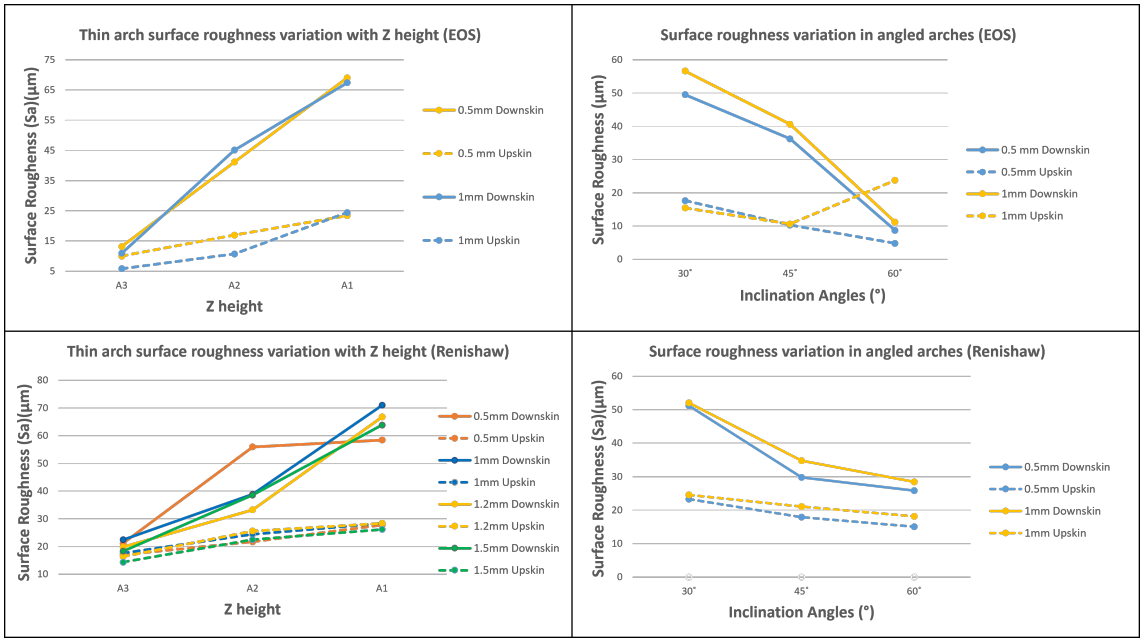

Figure 4.20: Surface roughness variation with respect to inclination in thin arches and angled arches in EOS and Renishaw.

Angled arches in both the platforms did not contain any observable anomalies in EOSTATE OT, Renishaw InifinAM or the powder bed data. Even though there were no adverse indications in the the in-situ monitoring systems, angled arches also display distortions and increasing surface roughness with decrease in inclination angle, particularly for downskin faces, refer Fig.4.20. Angled arches also experience distortions, prominently in the lateral direction, see Fig. 4.21(b). The angled arches show higher surface roughness at lower inclination angles (30°) as confirmed by Jones et al [21]. Thus, there are no indications in the monitoring system for the increase in surface roughness with decreasing inclination angle. Additionally, no major vertical distortions nor dross formation were present on these specimens, which matches the

lack of anomalies present in the monitoring data.

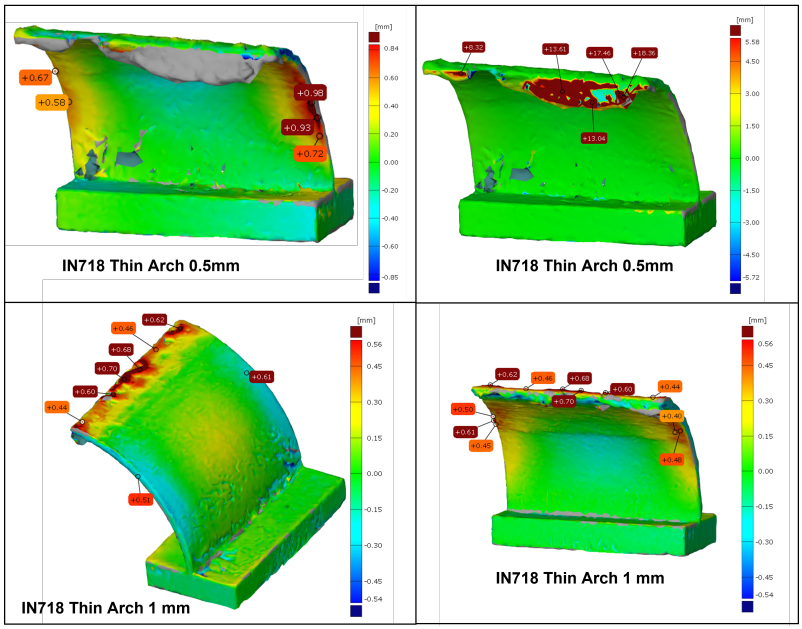

(a)

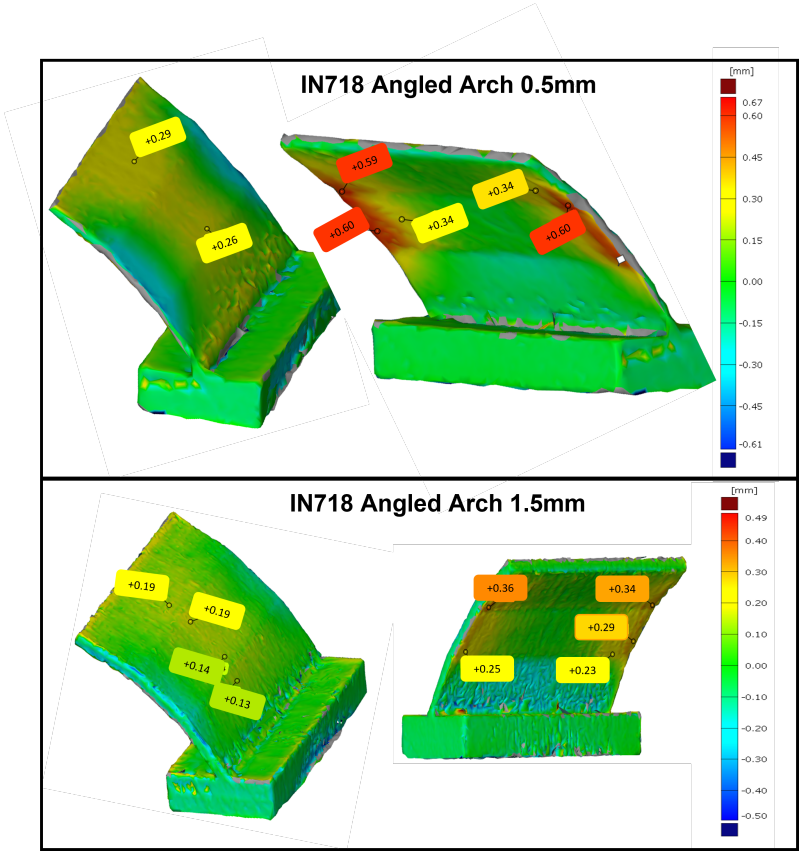

(b)

Figure 4.21: Comparison of 3D scans to CAD models for different arches printed in EOS.

4.3.4 Large artefact with internal channels

The large artefact printed had internal channels at the bottom part of the geometry and the top part consisted of vertical tubes of different diameters and an inclined wedge (Table 3.5). The internal channels ranged from a diameter of 7 mm to 0.8 mm.

The in-situ monitoring systems for EOS and Renishaw both showed hotspots at the layers where each of the internal channels was closing. These hotspots correspond to the top layers of the channels and appear at different build heights due to the varying diameters of the internal channels as depicted in Fig. 4.22.The meltpool depth is larger than the layer thickness at the top of the channels which causes heating of the powder layers below the overhanging regions of the channels and loose powder particles to fuse to the roof of the channel [146]. Fig. 4.23 shows the outline of the changed shape of the internal channels superimposed on the XCT slice of the internal channels due to powder agglomeration. The measurements of channels in the vertical and the horizontal directions is as shown in Fig. 4.23. The diameter is reduced by a significant margin in the vertical direction compared to the nominal diameter of the channels. The smaller diameter channels, are more constricted and narrower compared to the larger diameter channels. XCT slices in the Z direction in Fig. 4.23 show the blockage of the smaller channels with powder agglomeration. The constriction of the internal channels is inversely proportional to their diameter with more constriction of narrower channels compared to the wider channels [69]. Feng et al.[146] also observed that the dross formation was considerably significant for smaller internal channel diameters from 1mm to 3mm. The hotspots on the top of the channels correspond to the heat accumulation on the overhangs. There is no indication of any powder bed anomalies in the vicinity of the channels in both EOS and Renishaw monitoring systems.

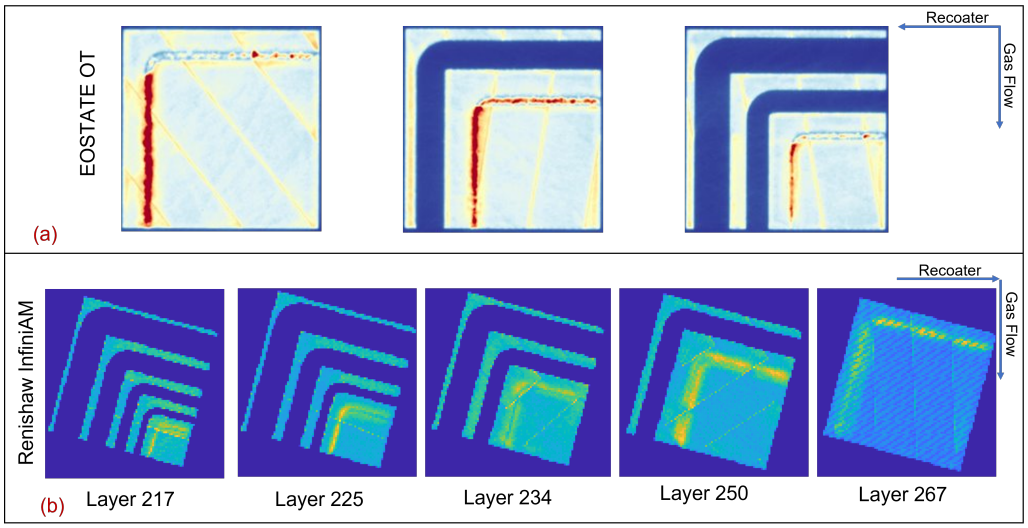

Figure 4.22: (a) Hotspots on the closing overhang surfaces of the internal channels in IN718. (b) Hotspots visible on various layers on the overhang surfaces of the internal channels in Ti6Al4V.

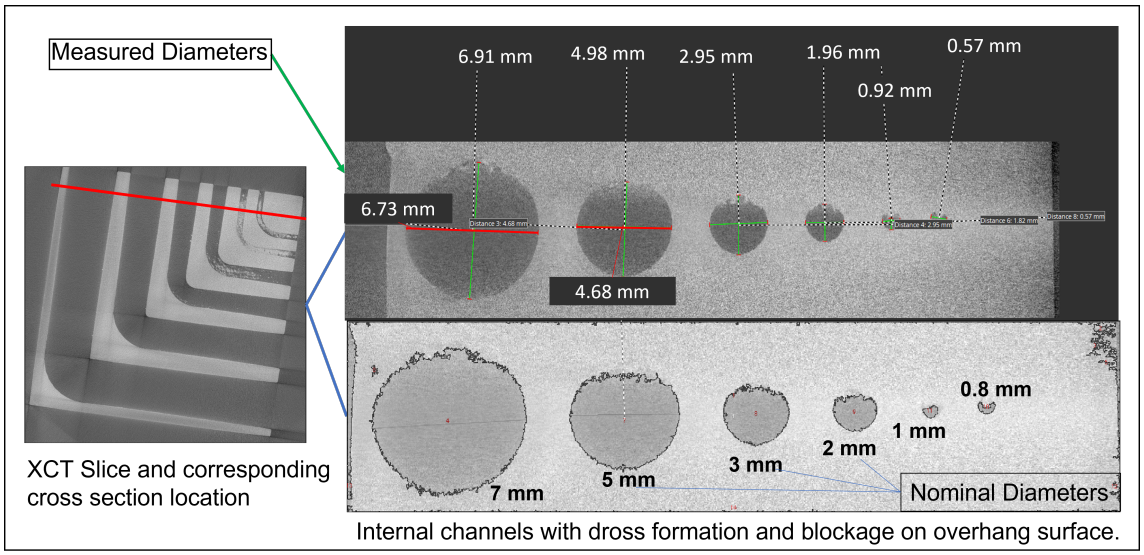

Figure 4.23: Vertical and horizontal XCT slices depicting dimensional deviations in the internal channels.

The vertical tubes in IN718 were printed with varying diameters and two thickness of 1mm and 2mm. For Ti6Al4V the tube designs had varying thickness in the vertical direction. The tubes and wedge on top of the channels did not show any anomalies in the EOSTATE OT system or powder bed. However, in the InfiniAM spectral images, hotspots were observed in the top layers on the thinnest parts of the tubes with 0.4mm thickness, see Fig. 4.24. In the LayerCam images, the top layers of the thin tubes are visible through the powder bed in several layers from layer 503 onwards to the completion of the part. Even though no XCT data are available for these parts, based on previous observations from powder bed images (Fig. 4.24), warpage in the build direction is expected on the top of these thin tubes.

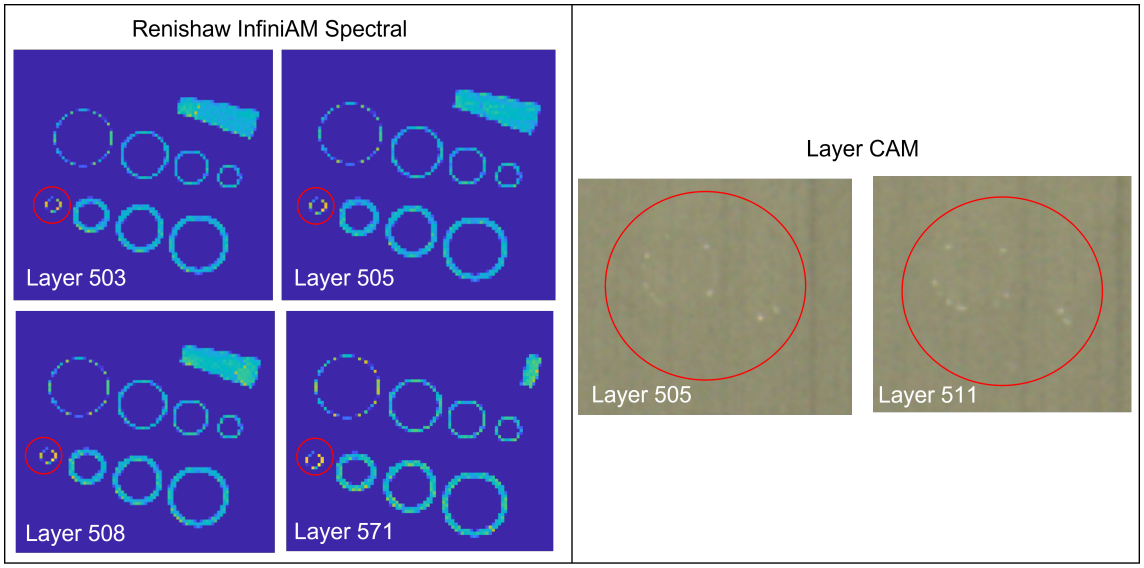

Figure 4.24: Hotspots on the thin tubes on and the exposed layers in the powder bed after powder dosing in Ti6Al4V.

4.3.5 Bridges

Bridges were designed with up to 8 mm and 10 mm horizontal unsupported structures for the EOS build and caused its failure. The design of the bridges for the Renishaw build was changed with the horizontal unsupported areas ranging from 5mm to 0.5mm all of which were successfully printed. The intent was to examine the in-situ monitoring systems for signatures during the printing of the horizontal unsupported areas of the bridge and 3D scan them to compare with the nominal CAD to understand the extent of geometrical deviation.

The 0.5mm bridge was CT scanned instead of 3D scanning as the gap was too small for the laser beam to scan and obtain the surface data. All the other bridges from 1mm and upwards were 3D scanned. In the InfiniAM spectral images hotspots are observed on downfacing surface of all the bridges except for the 0.5 mm as observed in the Fig.4.25(a). The LayerCam indicates a slight anomaly in the powder bed, Fig.4.25(b) for all bridges which have higher intensity hotspots. In the 3D scanning the it is evident that the maximum deviation is measured in 5mm bridges, Fig.4.25(c).

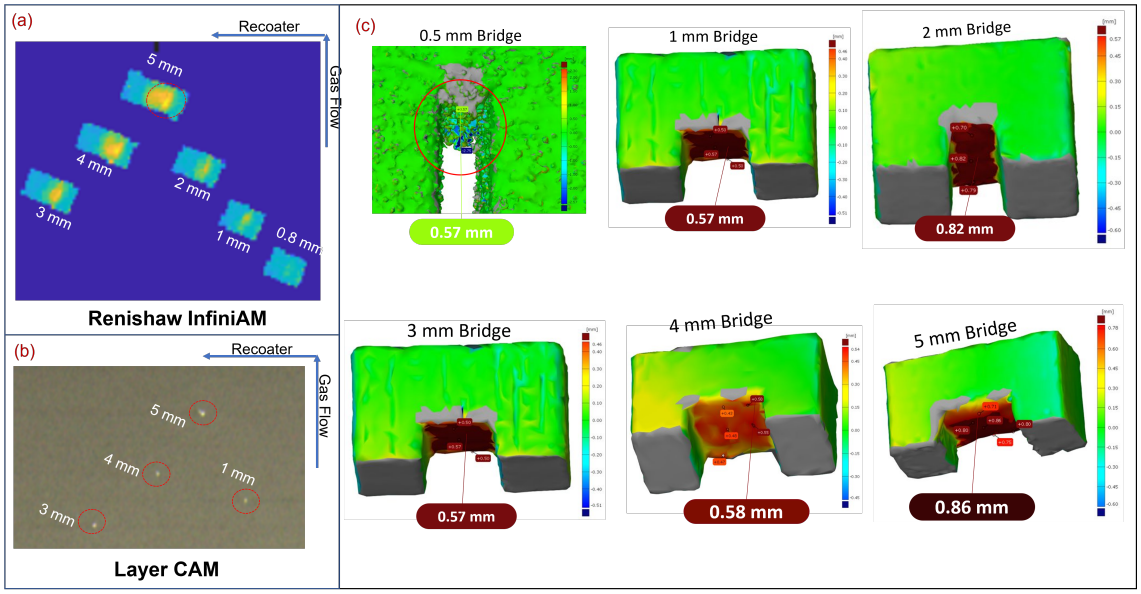

Figure 4.25: (a) Hotspots indicated in the Renishaw InfiniAM on the unsupported overhang layers of bridges. (b) Deviation on the unsupported overhangs from their nominal geometries.

The 3D scan results agree with Herzog et al. [68] that, a considerable material fall-in is seen in the downskin surfaces of bridges with spans greater than 3 mm . The size of the hotspots are directly proportional to the bridge span in this study. The overhang regions with larger spans have low heat dissipation through the powder layer below causing the adhering of the powder particles to the downskin surface of the bridges [146]. In the XCT scan mesh of the 0.5 mm bridge (Fig.4.25(c)) a lot of powder adhered to the unsupported overhang and probably is an indication of balling.

4.3.6 Gyroid lattice

The gyroid lattice, made in IN718, of 15% volume fraction and unit cell size of 8 mm was manufactured to its complete height and showed no obvious deformation or broken struts from visual inspection. This was confirmed with the actual part-to-CAD comparison. Yan et al. [73] attribute this to the self-supporting design of the structures unlike other other cellular lattices which have overhanging struts. XCT data revealed a large quantity of powder particles on the surface of the struts. This is also observed in previous studies and is attributed partially melted powder particles on the boundary of each layer by the contour laser track [73].

Internal defects were identified by the CT scans. A large number of pores were detected in the analysis, but these included the open pores in areas where struts joined due to surface defects. Since the open-pores were too many to analyse, they were filtered out by shifting the boundaries of the porosity analysis 0.2 mm towards the inner region of the part. A total of 15 near-surface and bulk porosity were detected in the entire part at various locations (Fig. 4.26). Their size varied from 60 μm to 160 μm with a sphericity ranging from 0.49 to 0.83. Based on the size and sphericity, there are a mix of gas pores and lack-of-fusion defects. In comparison to previous studies which manufactured gyroid lattice structure of 8mm cell size with a part density of 90% [73], the part manufactured in this study shows negligible volume fraction of defects.

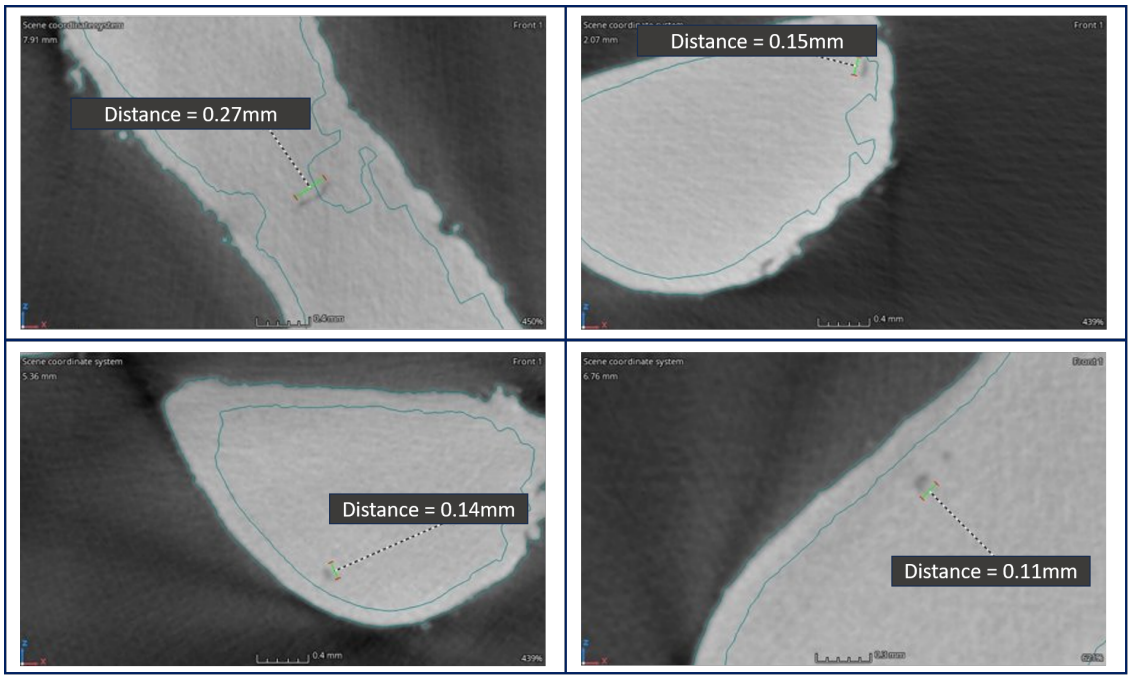

Figure 4.26: Examples of the largest pores observed in the XCT analysis

The data from the monitoring system do not show any anomalies on the locations where these defects are present (Fig. 4.27). Higher intensity spots are observed in the OT images corresponding to the first few layers where the struts of the lattice

join (Fig. 4.28) . This might be indicative of the low heat dissipation in the first few unsupported layers, resulting in the adhering partially melted powder particles on the surface. No anomalies were observed in EOSTATE powder bed images.

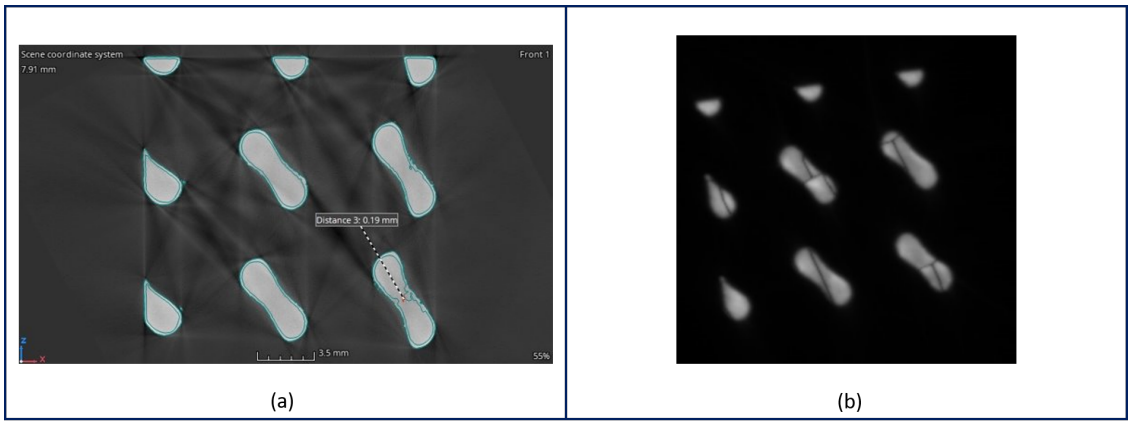

Figure 4.27: Comparing the location of the pore between (a) observation in XCT slice (b) observation in corresponding OT layer

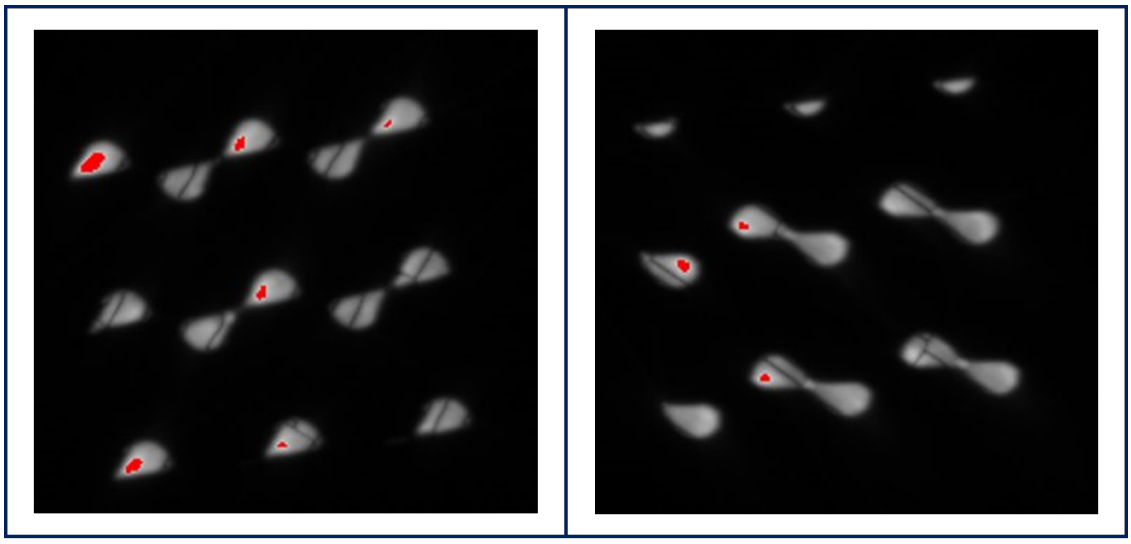

Figure 4.28: High intensity spots seen in OT image in the layers where the struts join. Red regions are the mask applied to the image and correspond to the pixels with intensity above an arbitrary threshold grayvalue.

4.3.7 Cross lattice

The cellular lattice structure, with straight beam-like struts, containing both horizontal and vertical beam elements manufactured using IN718 was fully printed. Visual inspection of the parts revealed that the struts contained significant deviation in their size with material fall-in in the overhanging horizontal struts. A significant deviation was observed in the vertical struts which were not aligned to their cylindrical axis (waviness). NDE was carried out on the dimensions and the waviness

of the horizontal and vertical cylindrical features. A total of 60 horizontal and 50 vertical features were investigated at different sections in the part (X1-X6 along longitudinal axis, Y1-Y4 along lateral axis, Z1-Z8 along vertical axis). Compared to the nominal dimension of the struts which was 0.47 mm, the observed average size of the horizontal features were 0.63-0.65 mm measured in the vertical direction (Fig. 4.30) and 0.45-0.49 mm in the lateral direction (Fig.4.29). This data confirms the fall-in observed in the horizontal features in the building direction. The observed deviations are as expected based in the guidelines for printing IN718, according to which the maximum overhang to avoid fall-in is 1mm [68], whereas the length used in this specimen was 1.5 mm.

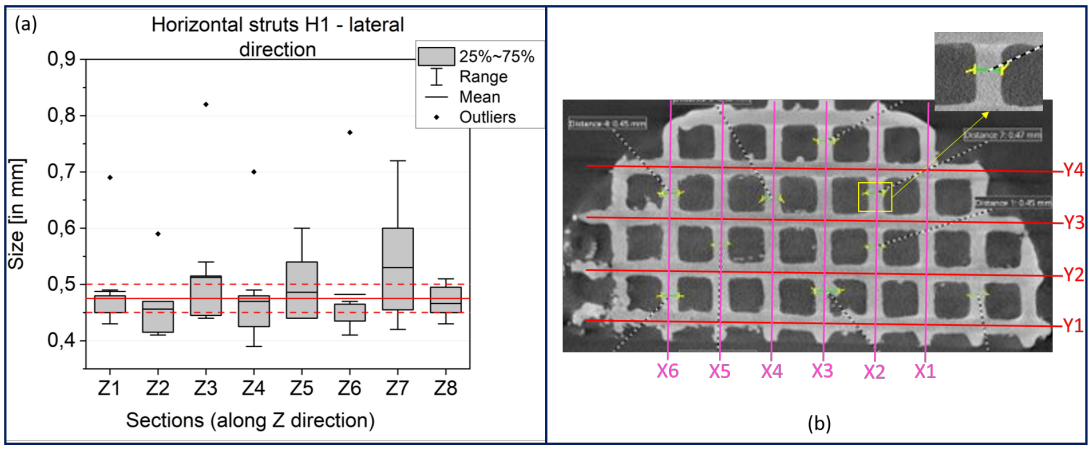

Figure 4.29: Size distribution of horizontal features in the lateral direction

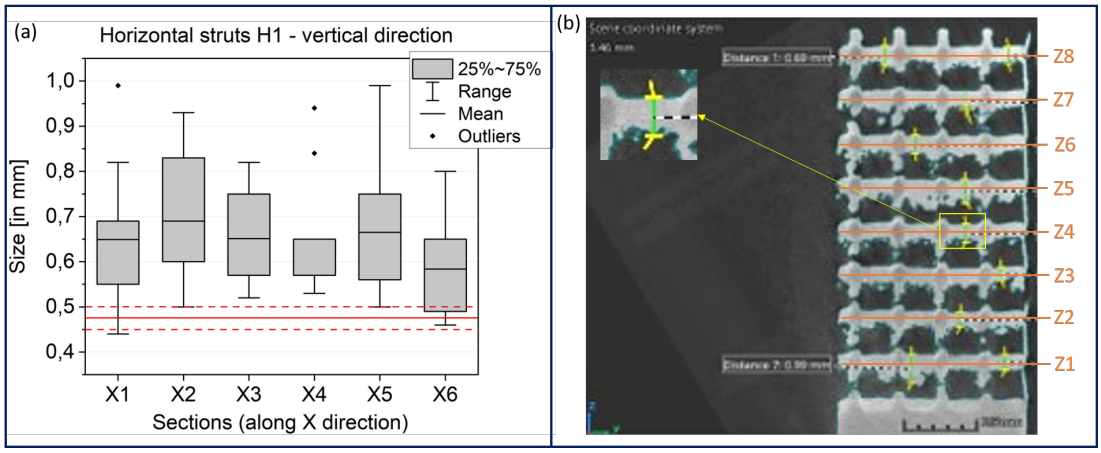

Figure 4.30: Size distribution of horizontal features in the vertical direction

The average size of the vertical features was 0.60 mm (Fig. 4.31) with waviness of 0.41 mm (Fig. 4.32). This suggested a very large deviation of the geometry both from its nominal size and its cylindrical axis. This phenomenon was not observed in previous study with similarly designed struts, where the vertical features were observed to be cylindrical and closer to their nominal sizes with small variation along their length [74]. This behavior was attributed to their self-supporting design [74].

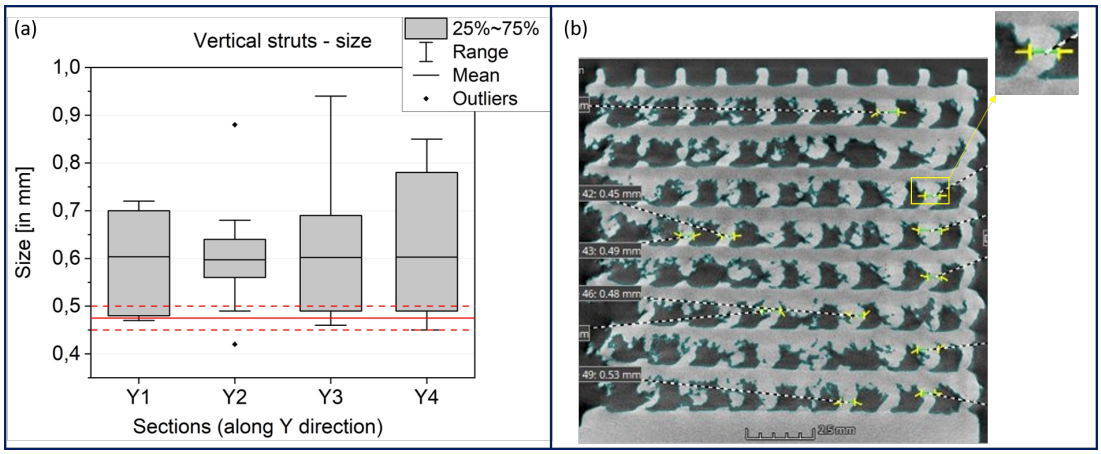

Figure 4.31: Size distribution of vertical features

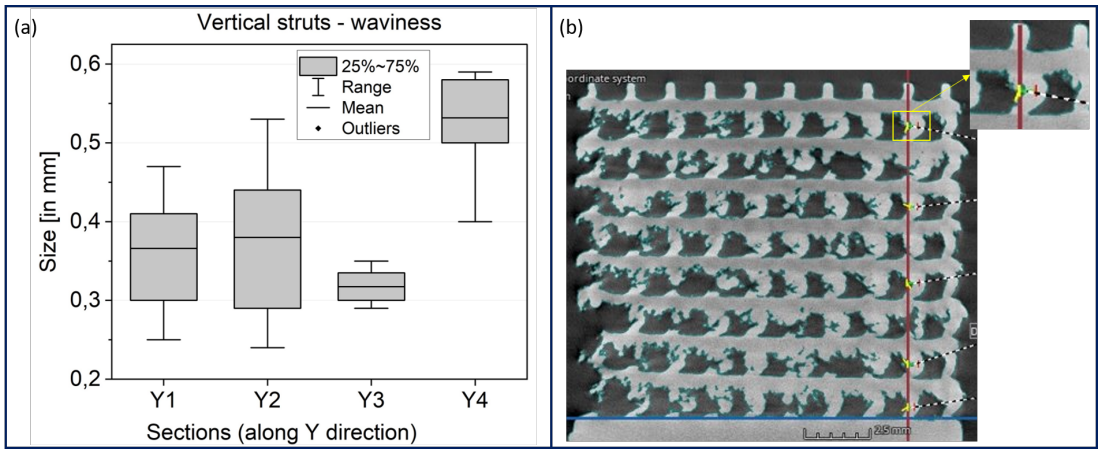

Figure 4.32: Deviation of vertical features from its cylindrical axis

Some anomalies observed in the OT data, correspond to shifted features (Fig.4.33) and also oversized features (Fig.4.34) in some layers. These correlate with the behaviour we see on the vertical struts of the physical part like deviation from its cylindrical axis and oversized strut dimensions.

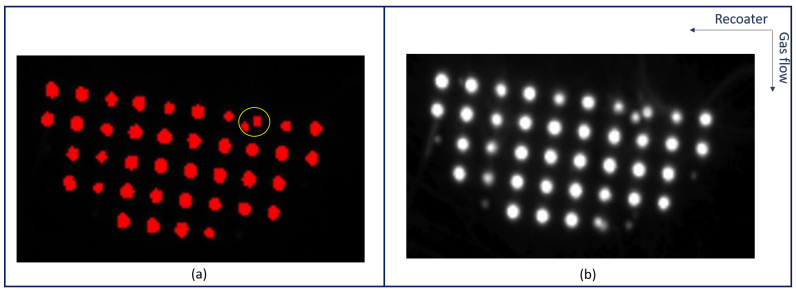

Figure 4.33: Anomalies that correspond to shifted features seen in (a) binary OT image (b) over-exposed OT image

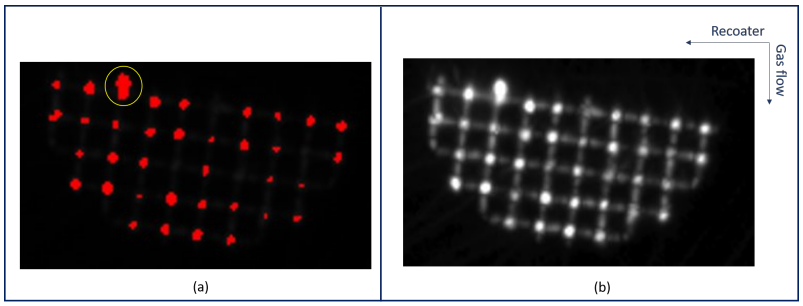

Figure 4.34: Anomalies that correspond to oversize features seen in (a) binary OT image (b) over-exposed OT image

In the Ti6Al4V, the deviation of vertical features from its cylindrical axis was absent. This maybe attributed to the effect of the recoater blade as a soft recoater was used for Ti6Al4V when compared to hard recoater for IN718. The shift in the vertical struts is along the travel direction of the recoater, further affirming this assumption.

4.3.8 Overhang holes

Holes of diameter ranging from ∅1mm to ∅12mm, were manufactured in three angles 30°, 45° and 60° with respect to the powder bed in both the setup. The 30° specimen in IN718 did not print successfully while the rest of the specimens were manufactured to its complete height but not without deviations (Fig. 4.35). All overhang holes were seen to have fall-in on the top of the hole regardless of the diameter.

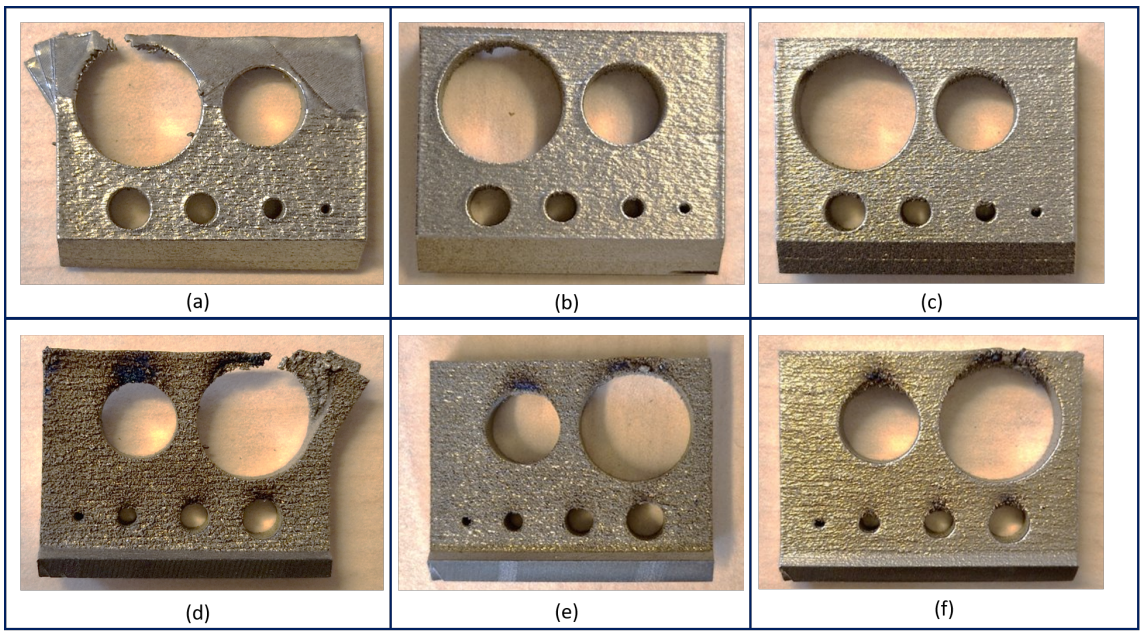

Figure 4.35: Upskin surface of (a) 30° (b) 45° (c) 60° specimens, downskin surface of (d) 30° (e) 45° (f) 60° specimens

Greater fall-in is experienced in the diameter smaller than ∅2mm and larger than ∅8mm. Comparison of actual part to the CAD geometry (Figures 4.37a, 4.38a) shows that the magnitude of deviation increases with increase in overhang angle. Maximum deviation in the diameter is 0.45 mm for ∅3mm hole at the angle of 60° (Fig. 4.38a). This trend is also observed in the Ti6Al4V specimens (Figures 4.41a,4.42a, 4.43a). These observation are in line with Herzog et al. study of similar specimens produced using IN718 and LPBF technology [68]. The measurements are limited to the holes larger than ∅2 mm, as the 3D scanner could not capture accurate data for resolution sizes equal or less than 2mm.

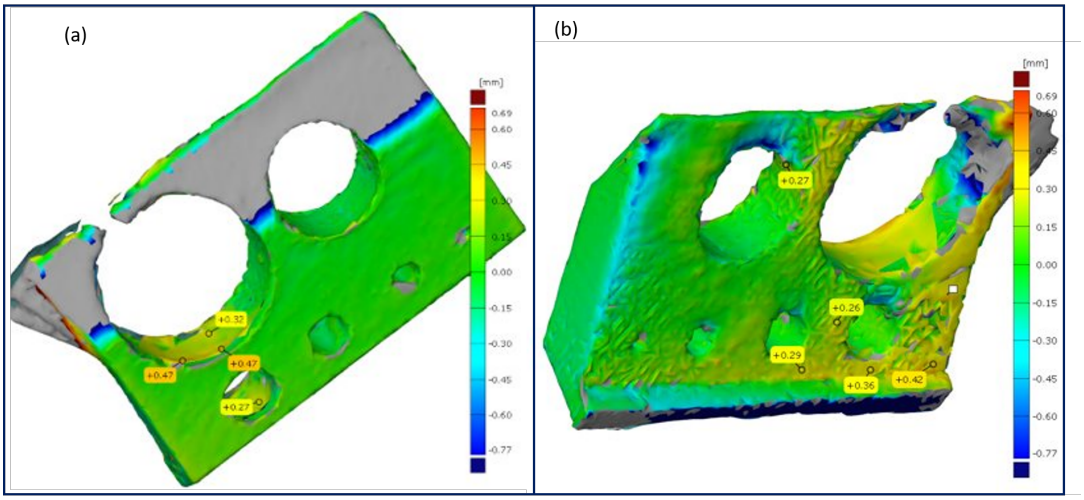

Figure 4.36: Actual part-CAD comparison showing deviations in (a) upskin surface (b) downskin surface of 30° specimen manufactured in Inconel 718

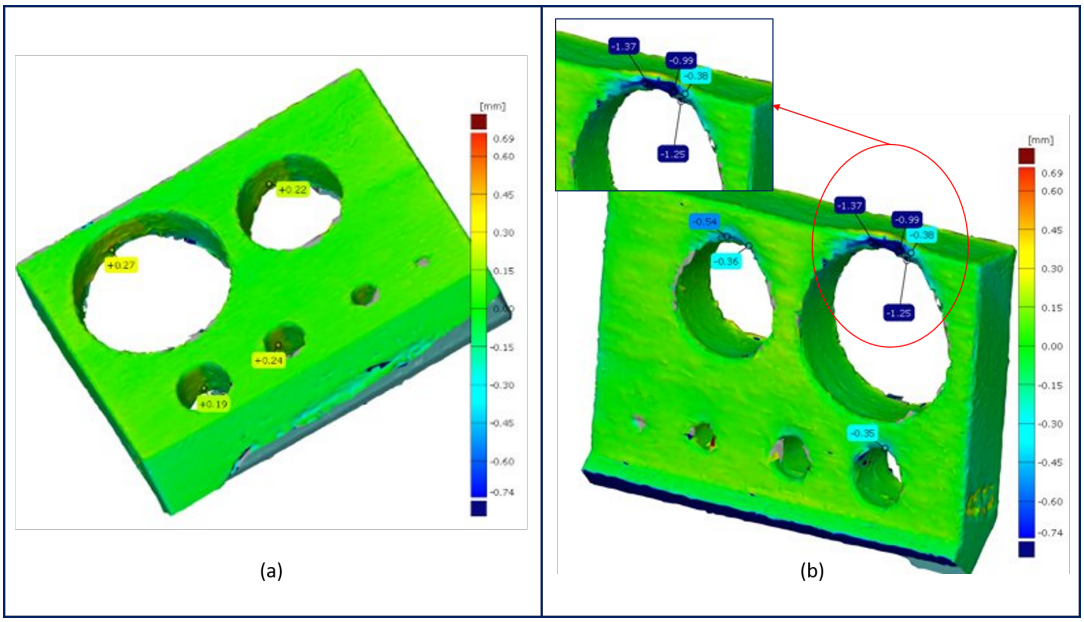

Figure 4.37: Actual part-CAD comparison showing deviations in (a) upskin surface (b) downskin surface of 45° specimen manufactured in Inconel 718

A distortion is seen on the down-facing edge of the holes of diameter greater than 8mm (Figures 4.37b,4.38b). This effect is pronounced on the edge of the ∅12mm hole of the 30° specimen (Fig. 4.35d). The maximum distortion that is measurable is observed to be 1.37 mm on the ∅12mm hole of the 45° specimen (Fig1 4.37b). This defect can be attributed to worsening staircase effect with decreasing angle and distortion due to super-elevated edges [147].

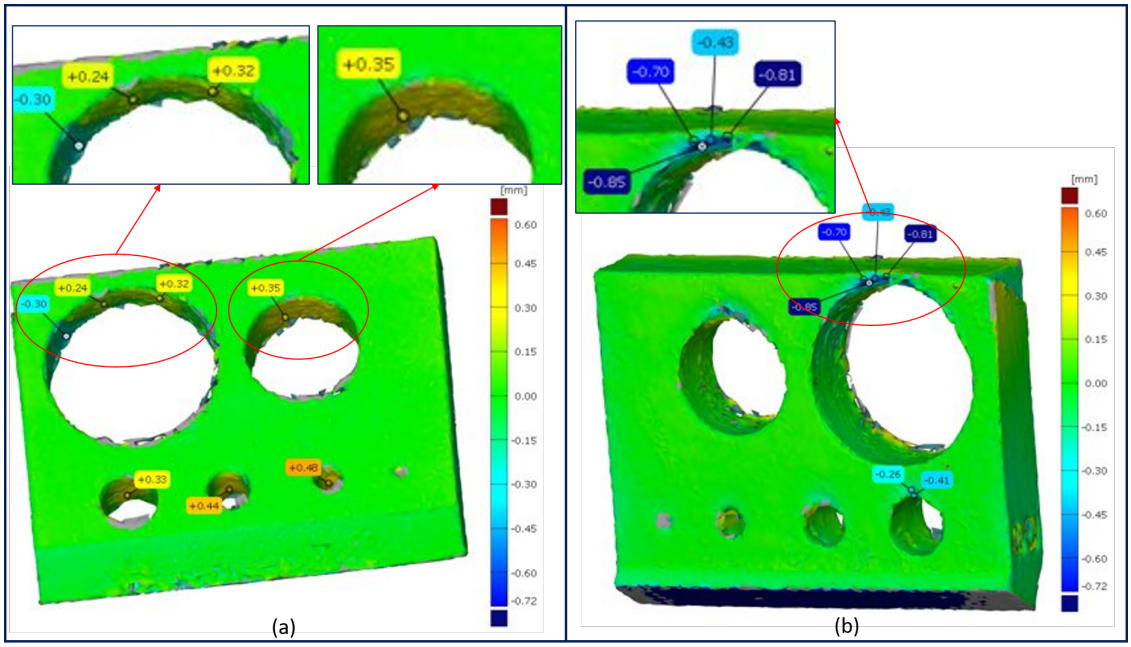

Figure 4.38: Actual part-CAD comparison showing deviations in (a) upskin surface (b) downskin surface of 60° specimen manufactured in Inconel 718

The down-facing surfaces in most layers showed hotspots in the OT data. Higher intensity hotspots were seen near the edges of the diameters that were distorted. Anomalies are also observed in the powder bed images of corresponding layers, where exposed part edges are observed on the powder bed after powder recoating, indicating distortion in the build direction (Fig. 4.39). The layers with significant anomalies correspond to the location of distortion in the physical part.

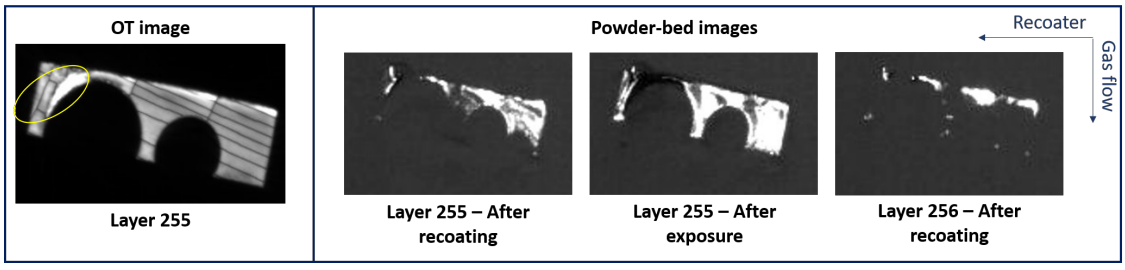

Figure 4.39: Example of anomalies observed in the OT and PB images of 30° specimen on the down-skin edges of ∅12mm hole

The layers that are seen to have exposed part in PB images post-recoating also correspond to layers with discontinuous elements in OT images at the down-skin edge of ∅12mm hole. This is seen in all the three samples (Fig. 4.40), but a higher frequency of this anomaly is observed for the 30° specimen, which failed due to large discontinuity on the ∅12mm hole. There is a strong correlation between the anomalies in monitoring data and this type of defect.

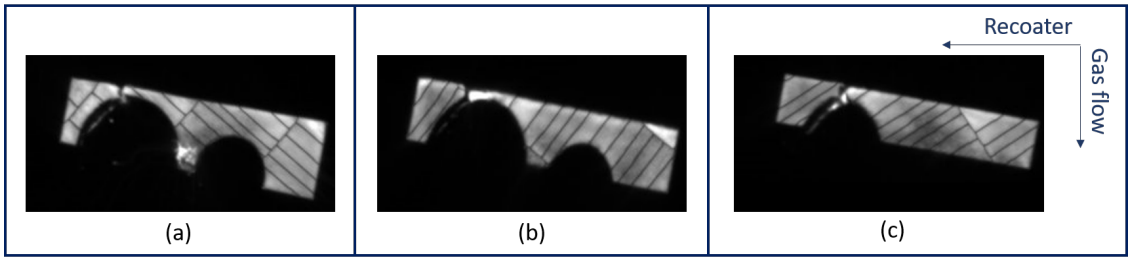

Figure 4.40: Example of discontinuous elements observed in OT images of (a)30° (b)45° (c)60° specimens on the down-skin edges of ∅12mm hole

The Ti6Al4V specimens shows lesser magnitude of distortion (Figures 4.41b, 4.42b, 4.43b) in comparison to the IN718 specimens (Figures 4.36b, 4.37b, 4.38b). For Ti6Al4V specimens, maximum deviation observed in the diameter was 0.40mm on the ∅3mm hole on the 60° specimen (Fig. 4.43a) and maximum distortion of 0.36 mm observed on the down-facing edge of the ∅12 mm hole on the 30° specimen (Fig. 4.41b).

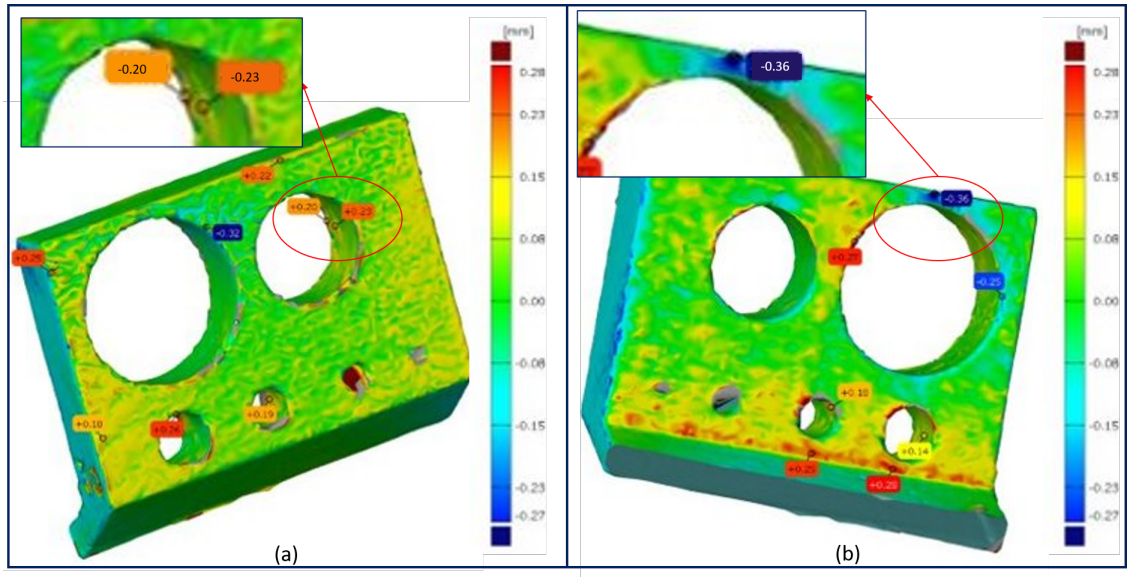

Figure 4.41: Actual part-CAD comparison showing deviations in (a) upskin surface (b) downskin surface of 30° specimen manufactured in Ti6Al4V

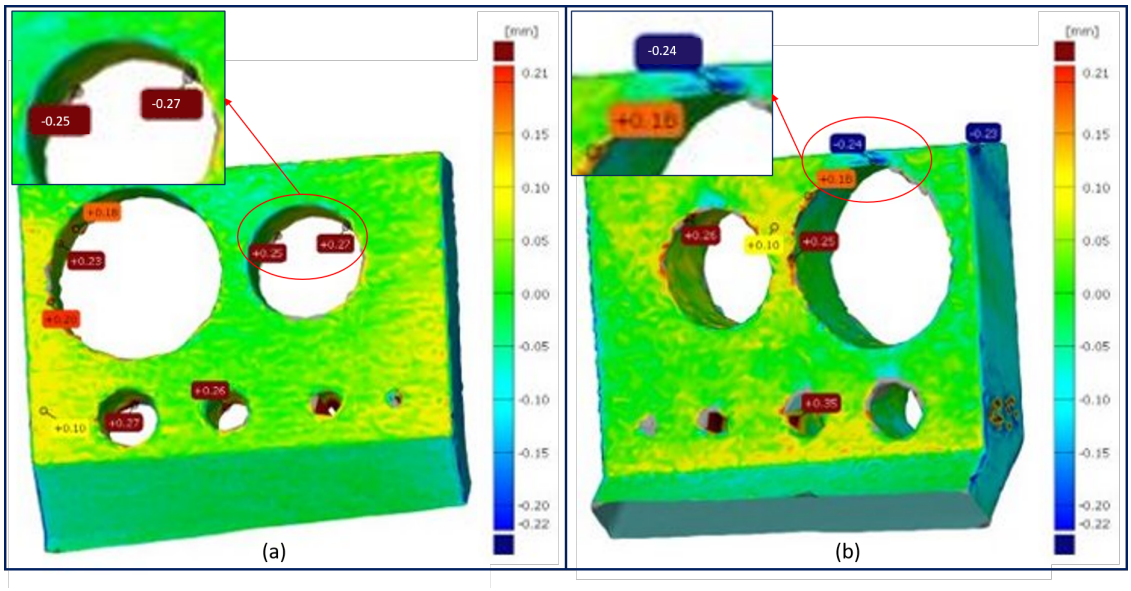

Figure 4.42: Actual part-CAD comparison showing deviations in (a) upskin surface (b) downskin surface of 45° specimen manufactured in Ti6Al4V

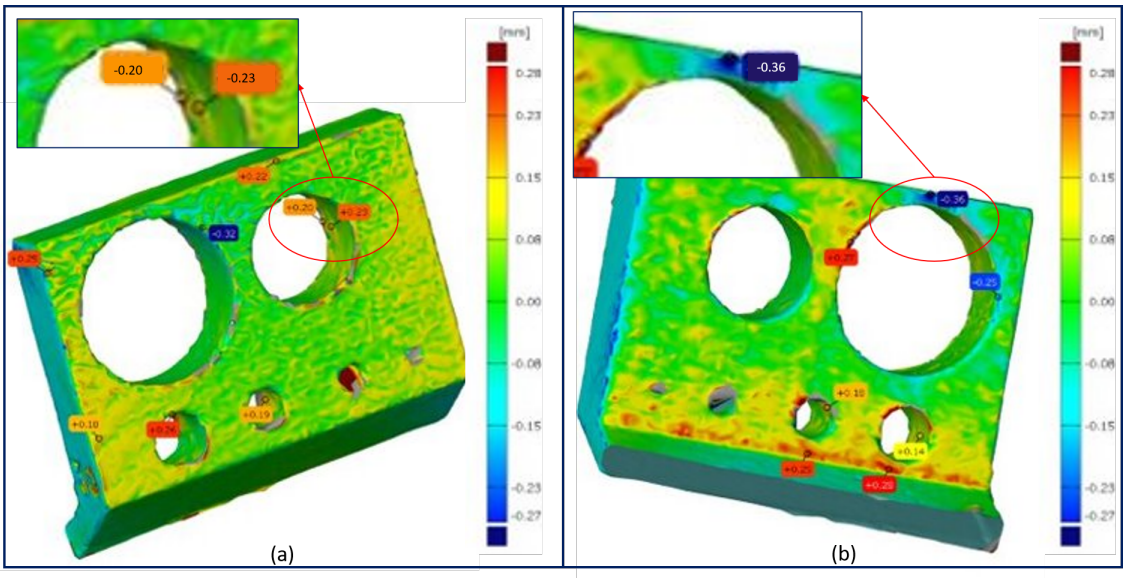

Figure 4.43: Actual part-CAD comparison showing deviations in (a) upskin surface (b) downskin surface of 60° specimen manufactured in Ti6Al4V

From the Renishaw spectral data, there are some hotspots near the edges of the holes (Fig. 4.44) that might indicate a distortion similar to the observation in the EOSTATE OT. The hotspots are observed on the same location in a number of layers, irrespective of the hatch angle, indicating their presence is not merely due to the effect of short hatch vectors. But the powder bed images of corresponding layers where hotspots are observed in the spectral data, do not show any significant anomalies.

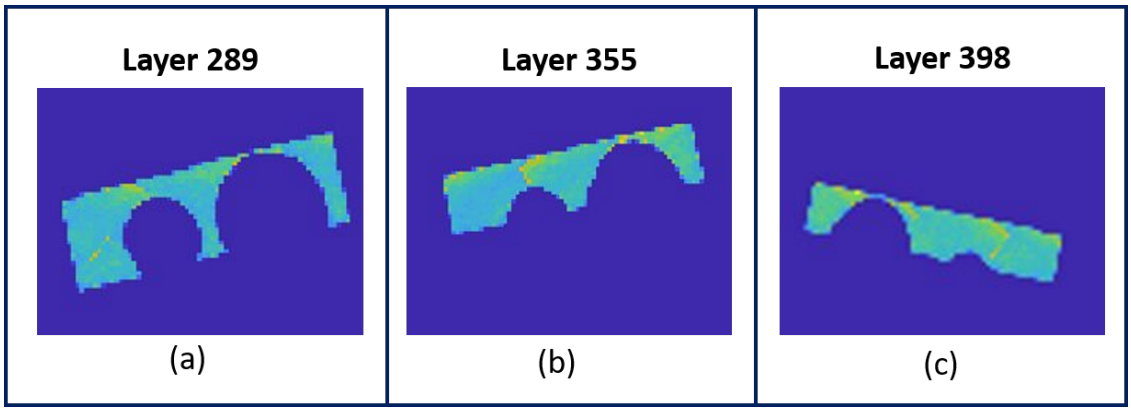

Figure 4.44: Heat sigatures in the spectral data of (a)30° (b)45° (c)60° specimens on the down-skin edges of ∅12mm hole

4.3.9 High aspect ratio thin rods

None of the thin rods parts in IN718 were built to their full height as the build was interrupted. It can be observed that all rods of diameter less than 0.8 mm were not successfully built (Figures 4.45a, 4.45b). A similar effect is not observed in Ti6Al4V, where all the vertical bars where built with to their full height (Figures 4.45c, 4.45d). The behaviour of Inconel 718 specimens are in contrast to previous studies [68] where thin vertical bars of diameters less than 0.8 mm were printed to their full height.

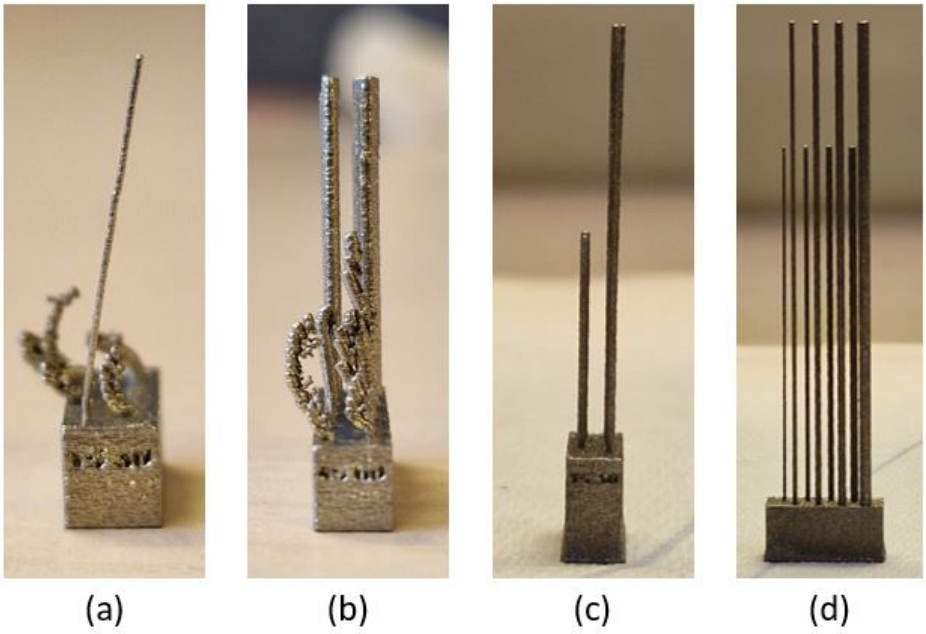

Figure 4.45: Partially built IN718 thin rods (a) designed height of 15mm and 30mm (b) designed height of 45mm and 60mm and successfully built Ti64 thin rods (c) height of 15mm and 30mm (d) height of 45mm and 60mm

Only the ∅0.4mm bar from the Renishaw build exhibited deviation. It is to be noted that these bars could bend during handling due to their weak structural integrity. Therefore this deviation might not be true indication of deviation in as-built part since the components went through different manual post-processing before 3D scanning stage.

The EOS monitoring data was examined due to the presence of significant deviations. For better visualization of the subtle features in the OT data, an arbitrary threshold was selected and the grayscale images were binarized. The red region in Figure 4.46 registers intensity above this threshold value. The OT data for multiple layers showed signs of shifted features (Fig. 4.46). This is indicative of the deviation observed in the physical part. Also to be noted, the thin rod of ∅0.3 mm showed no shift between layers but this might be due to smaller resolution of the part and limitation with the analysis technique.

The powder bed images of the corresponding layers showed deviation such as improper powder packing (Fig. 4.47). Also reviewing the EOS build layout, it is to be noted that the rods that survived in the build and were printed without significant deviation were shielded from the recoater by the solid cylinder part, standing in front, in the recoater travel direction (Fig. 4.48).

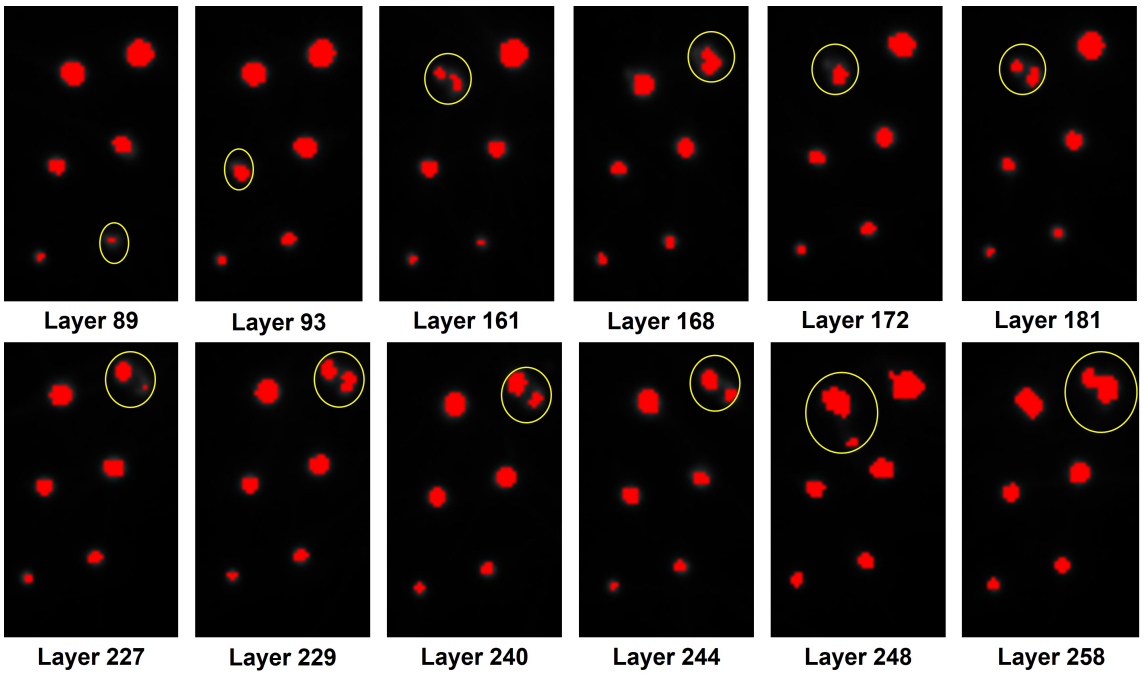

Figure 4.46: Binarized OT images of OT of the thin rods. Anomalies that corresponds to feature shift and distortion are visible.

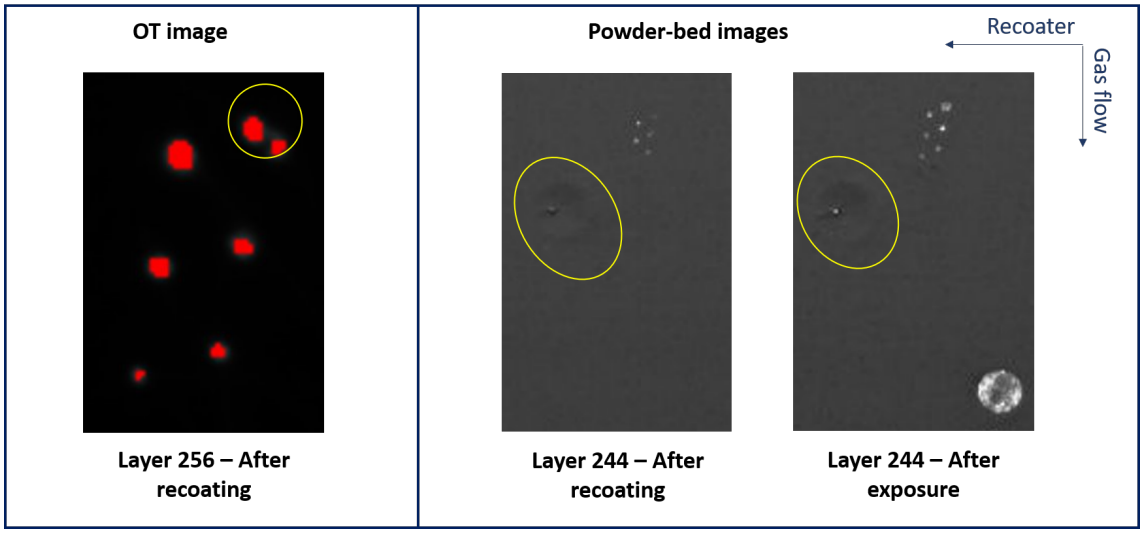

Figure 4.47: Correlation of OT layer data with powder bed defects before recoating and after exposure on that layer

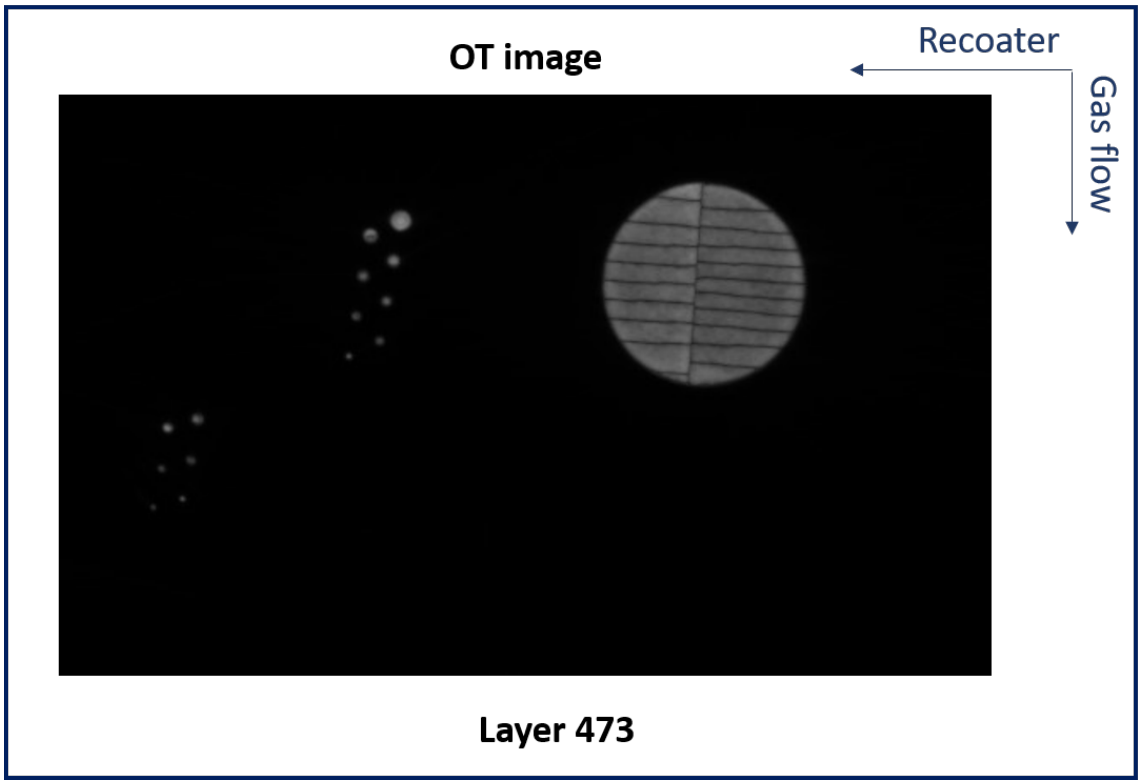

Figure 4.48: Thin rods shielded by solid cylinder in recoater travel direction

4.3.10 Parts with changing thin to thick cross-section

In the Ti6Al4V, two different types of geometries (Rectangular and circular) which change from thin to thick section were built, parallel to the build direction, with support structures on the overhangs. After manual removal of the support structures, the edge where the thin-to-thick transition occurs was investigated. From the

actual part to CAD comparison, it was confirmed that the sharp edge experienced some distortion and did not print accurately on both parts. A maximum deviation of 0.75 mm was observed on the transition edge of the part with rectangular section (Fig. 4.49), and 0.50 mm on the part with circular cross section (Fig. 4.50). This was expected, as sharp features generally observe high heat stresses due to the acute scan vectors in these regions.

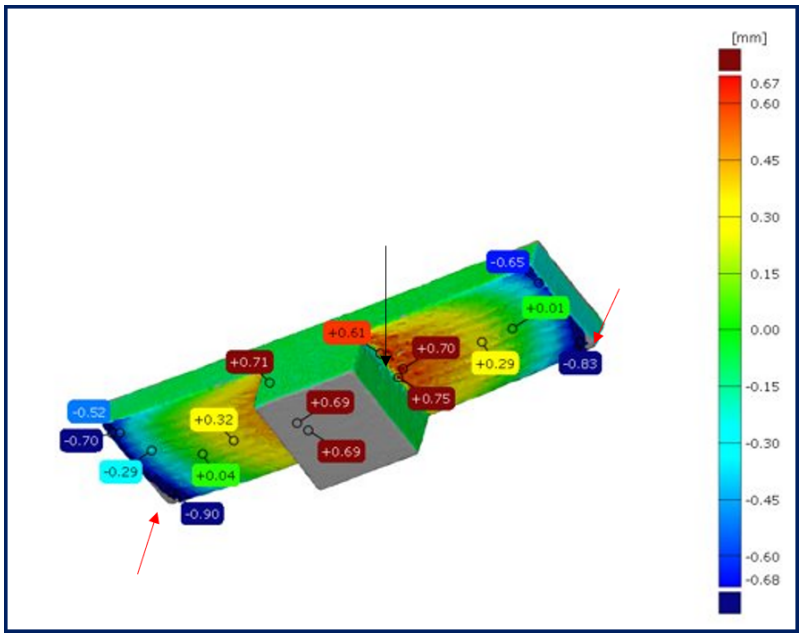

Figure 4.49: Actual part-to-CAD comparison for specimen with rectangular-section

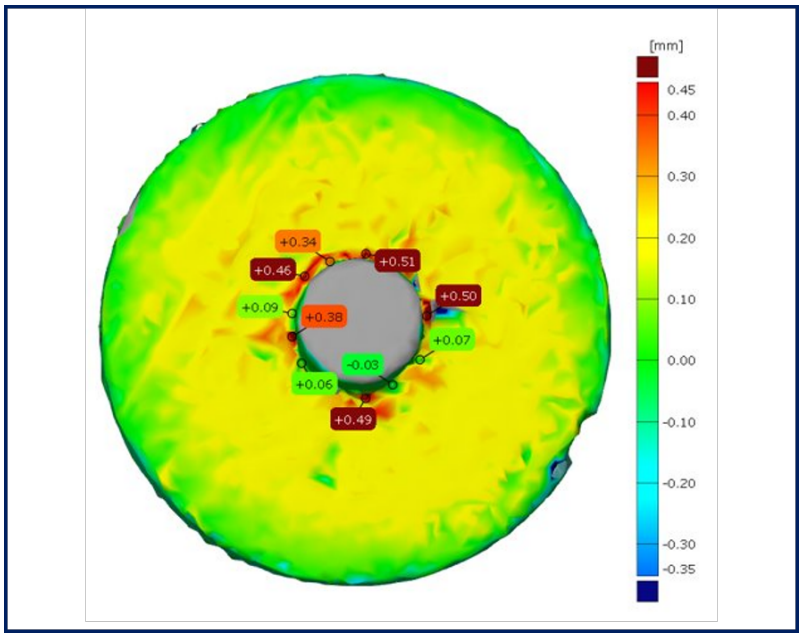

Figure 4.50: Actual part-to-CAD comparison for specimen with circular-section

From the spectral data, we observe that there is a sudden change in the laser intensity in both parts, on the layers where the transition occurs, and it begins near the particular edge (Fig. 4.51). This signature can be attributed to the lower heat dissipation through the support structures as compared to the bulk of the part. The effect continues for three layers. This anomaly observed in the spectral image can be indicative of distortion. It is to be noted that in the part with the circular cross section, the removal of the support structure could not be achieved completely. Therefore, the deviation observed in the actual part to CAD comparison might not be accurate.

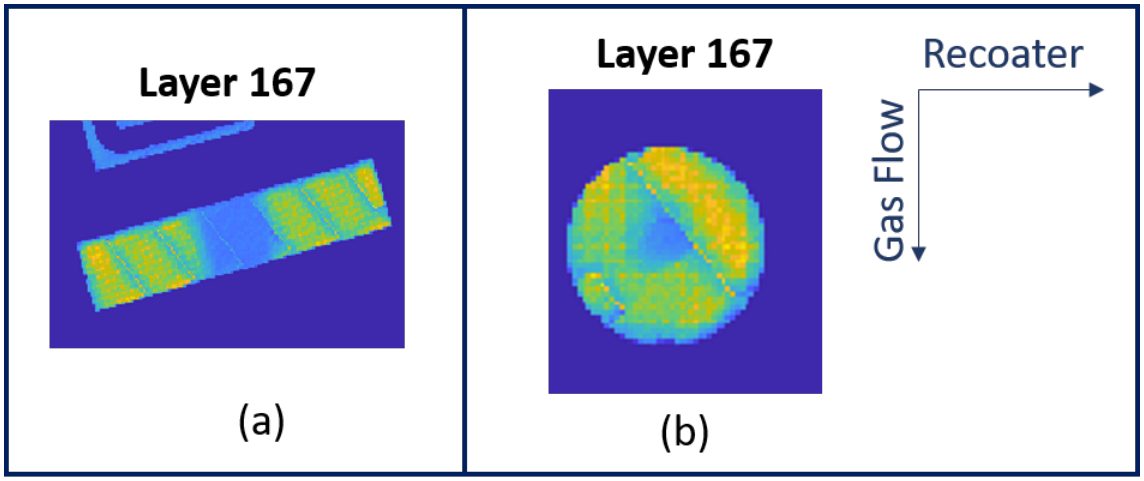

Figure 4.51: Difference in intensity observed on spectral data of (a) Rectangular-section (b) Circular-section specimen

In the T-section part, warpage is observed on the extreme edges of the bottom surface of the overhangs (marked with red arrows in Fig. 4.49). The effect is more pronounced in the corners and are of the magnitude 0.9 mm and 0.65 mm. This warping effect can be attributed to the effect of residual stresses which are a common contributing factor to warpage in thick section with weak supports. In spectral images, high intensities correlate to the the corners where the deviation is maximum (Fig. 4.51). Although similar warping effect is observed in the top layers of the overhangs, there are no significant signature that indicate this defect. This allows us to speculate that this effect can be observed only on the downskin surfaces of the overhangs.

Similar warping due to residual stress was also observed in the thick plate part printed in Inconel 718. The behaviour agrees with Simufact simulation of the part with maximum deviation, of 1.37mm, observed on the corners of the edge of the part (Fig. 4.52).

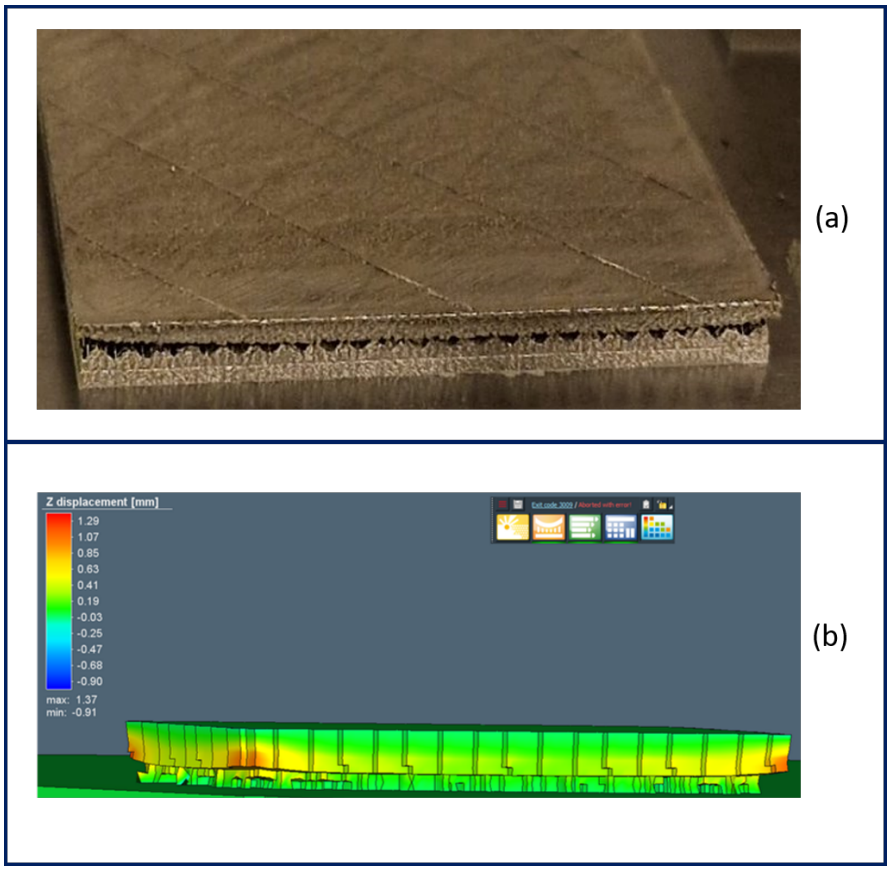

Figure 4.52: Warping on the edges of the thick plate (a) as observed in the part (b) observed in the simulation results

Higher intensity in OT images was registered in the first few layers of the part especially on the corners due to short hatch vectors (Fig. 4.53). This effect is consistent among layers with the short hatch vectors, thus indicating that short hatch vector could be a contributing factor to warpage due to high thermal stresses.

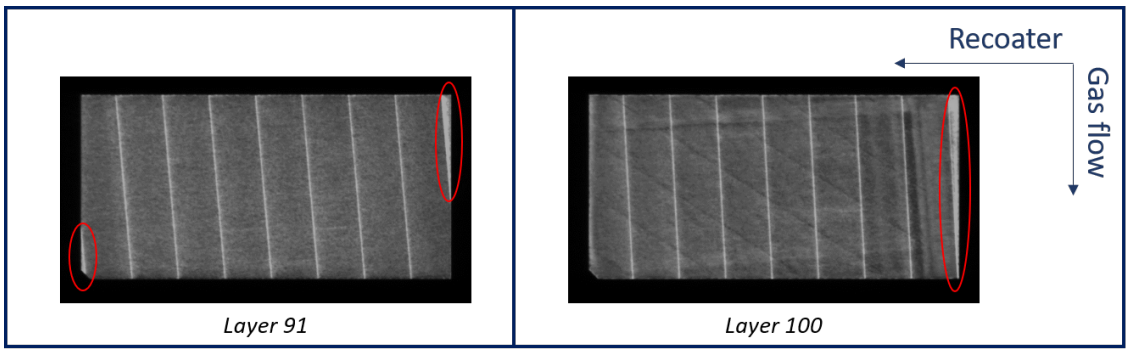

Figure 4.53: High intensity regions observed in the layers with short hatch vectors

5
Conclusion

This study was successful in provoking the intended defects by challenging geometrical features, validating the presence of the defects using ex-situ measurements and further establishing relevant qualitative correlations between defects and the anomalies observed in the monitoring data.

5.1 Correlation of monitoring data to defects

- Distortion in the build direction has a stronger correlation to the powder bed anomalies than hotspots observed in OT/spectral images because it affects the interaction of the part with recoater and surrounding powder bed, resulting in visible anomalies in the powder bed images. However, there are instances where both hotspots and powder bed anomalies correspond to indicate distortions in build direction. Anomalies in the OT / Spectral data alone are not sufficient to indicate part distortion/warpage. These observations are valid for all parts that experienced significant distortions such as the thin rods, overhang holes, thin arches and thin walls.

- Hotspots that appear in layers with exposed surfaces in powder bed post-recoating correlate with progressively worse distortions in the subsequent layers. This was observed in the IN718 hourglass part, overhang holes and the thin arches.

- Presence of a hotspot may not always indicate defects. Hotspots can correspond to challenging geometrical features, defects or a combination of both.

- Geometries with small features are influenced by the type of recoater used and its contact with the parts. Identifying geometrical shift between layers in intricate geometries (lattice, thin rods and pins) in monitoring data is feasible in EOSTATE OT, due to its long exposure images.

- A strong correlation between surface roughness and anomalies in the monitoring data could not be established. However, severe surface defects observed in overhangs correlate to a high frequency of hotspots which occur at critical angle and short hatch vectors.

- Internal defects lesser than 150 µm were detected in XCT of the gyroid lattice,

however monitoring data did not show any anomalies that corresponded to the defect locations.

5.2 Challenges and limitation in this study

XCT measurements
CT scan clarity depends on material density, part thickness, noise generated and scan parameters. In this study large artefacts in IN718 generated a lot of noise in the scans, which could be resolved only to a limited extent in post processing. Smaller voxel sizes are needed to detect porosity. However, there is a trade-off between favourable scan parameters and voxel sizes. The detection of larger internal porosity was possible using this technique but the presence of the detected pores needs further validation.

3D scanning
This NDE methods was suitable for large features, however it was challenging to 3D scan small features (small holes) where the scanning laser cannot penetrate. Scanning of thin rods and holes of diameter less than 2 mm was not possible. Meshing errors when converting data from point cloud to mesh induced further errors in scan to CAD comparisons.

Surface roughness measurement
The non-contact optical measurements used in this study, calculates the Sa values, taking the average roughness of the selected region. It normalizes the effect of peaks and valleys and provides an average surface roughness value. This method is more suitable for surface roughness measurements of machined surfaces where large deviations are not generally expected unlike as printed LPBF components. Due to the machine's limitation in accessing certain regions of curved or angular surfaces, some of the samples would have to be cut for measurements. This invalidated the purpose of the method being non-destructive. Measurement of darker downskin surface was tricky as the optical system could not register the surfaces.

Data storage and handling
The data from the monitoring systems, especially from the Renishaw machine, was large and presented a challenge with transfer, processing and storage of the data. Monitoring sensor data obtained in the form of large text files needed to be converted into meaningful visualization of the process. The converted visual data that was analyzed was only a near representation of the true data. Comparatively, the EOSTATE system provided image data that could be used for analysis directly.

Monitoring data from parts with small resolution
The output from the monitoring systems were mapped into images of 2000x2000 pixels (EOSTATE OT) and 1000x1000 (Renishaw InfiniAM spectral). Some of the parts used in the study had features smaller than 1mm. The resolution on these parts was extremely low and the presence of anomalies was difficult to observe. Therefore some assumptions and image processing had to be employed, but there were limits to this approach as well.

5.3 Future Work

A further continuation of this study could be statistical correlation between the instances of anomalies observed in the monitoring data to the actual defects observed. Additionally, this work can be further developed to automate the detection of the anomalies identified in this study.

References

[1] "ISO/ASTM 52900:2021 Additive manufacturing-General principles-Fundamentals and vocabulary," Tech. Rep., 2023. [Online]. Available: www.sis.se.

[2] S. Roscoe, P. D. Cousins, and R. Handfield, "Transitioning additive manufacturing from rapid prototyping to high-volume production: A case study of complex final products," *Journal of Product Innovation Management*, 2023, ISSN: 15405885. DOI: 10.1111/jpim.12673.

[3] L. Yang, K. Hsu, B. Baughman, *et al.*, "Additive Manufacturing of Metals: The Technology, Materials, Design and Production Springer Series in Advanced Manufacturing," Tech. Rep. [Online]. Available: http://www.springer.com/series/7113.

[4] "Additive Manufacturing: Pursuing the Promise," Tech. Rep. [Online]. Available: https://www.energy.gov/eere/amo/articles/additive-manufacturing-pursuing-promise.

[5] B. Blakey-Milner, P. Gradl, G. Snedden, *et al.*, "Metal additive manufacturing in aerospace: A review," *Materials and Design*, vol. 209, Nov. 2021, ISSN: 18734197. DOI: 10.1016/j.matdes.2021.110008.

[6] P. Gradl, D. C. Tinker, A. Park, *et al.*, "Robust Metal Additive Manufacturing Process Selection and Development for Aerospace Components," *Journal of Materials Engineering and Performance*, vol. 31, no. 8, pp. 6013–6044, Aug. 2022, ISSN: 15441024. DOI: 10.1007/s11665-022-06850-0.

[7] Z. Snow, A. R. Nassar, and E. W. Reutzel, "Invited Review Article: Review of the formation and impact of flaws in powder bed fusion additive manufacturing," *Additive Manufacturing*, vol. 36, p. 101 457, Dec. 2020, ISSN: 2214-8604. DOI: 10.1016/J.ADDMA.2020.101457.

[8] M. Mani, B. Lane, A. Donmez, S. Feng, S. Moylan, and R. Fesperman, "Measurement Science Needs for Real-time Control of Additive Manufacturing Powder Bed Fusion Processes," National Institute of Standards and Technology, Gaithersburg, MD, Tech. Rep., Feb. 2015. DOI: 10.6028/NIST.IR.8036. [Online]. Available: https://nvlpubs.nist.gov/nistpubs/ir/2015/NIST.IR.8036.pdf.

[9] G. Tapia and A. Elwany, *A Review on Process Monitoring and Control in Metal-Based Additive Manufacturing*, Dec. 2014. DOI: 10.1115/1.4028540.

[10] J. P. Kruth, P. Mercelis, J. Van Vaerenbergh, and T. Craeghs, "Feedback control of Selective Laser Melting," in *Proceedings of the 3rd International Conference on Advanced Research in Virtual and Rapid Prototyping: Virtual and Rapid Manufacturing Advanced Research Virtual and Rapid Prototyping*, 2007, pp. 521–527, ISBN: 9780415416023.

[11] M. Grasso, A. Remani, A. Dickins, B. M. Colosimo, and R. K. Leach, "In-situ measurement and monitoring methods for metal powder bed fusion: An updated review," *Measurement Science and Technology*, vol. 32, no. 11, Nov. 2021, ISSN: 13616501. DOI: 10.1088/1361-6501/AC0B6B.

[12] Z. Smoqi, A. Gaikwad, B. Bevans, *et al.*, "Monitoring and prediction of porosity in laser powder bed fusion using physics-informed meltpool signatures and machine learning," *Journal of Materials Processing Technology*, vol. 304, p. 117 550, Jun. 2022, ISSN: 09240136. DOI: 10.1016/J.JMATPROTEC.2022.117550. [Online]. Available: https://linkinghub.elsevier.com/retrieve/pii/S0924013622000620.

[13] J. A. Mitchell, T. A. Ivanoff, D. Dagel, J. D. Madison, and B. Jared, "Linking pyrometry to porosity in additively manufactured metals," *Additive Manufacturing*, vol. 31, Jan. 2020, ISSN: 22148604. DOI: 10.1016/j.addma.2019.100946.

[14] J. Lesseur, B. Tranchand, T. Mancier, A. Montauzier, C. Larignon, and S. Perusin, "On the use of X-ray microtomography to control artificial defect geometries produced by metal additive manufacturing," *Nondestructive Testing and Evaluation*, vol. 37, no. 5, pp. 611–630, 2022, ISSN: 14772671. DOI: 10.1080/10589759.2022.2085701.

[15] C. Schwerz and L. Nyborg, "Linking In Situ Melt Pool Monitoring to Melt Pool Size Distributions and Internal Flaws in Laser Powder Bed Fusion," *Metals 2021, Vol. 11, Page 1856*, vol. 11, no. 11, p. 1856, Nov. 2021, ISSN: 2075-4701. DOI: 10.3390/MET11111856. [Online]. Available: https://www.mdpi.com/2075-4701/11/11/1856/htm%20https://www.mdpi.com/2075-4701/11/11/1856.

[16] C. Schwerz, B. A. Bircher, A. Küng, and L. Nyborg, "In-situ detection of stochastic spatter-driven lack of fusion: Application of optical tomography and validation via ex-situ X-ray computed tomography," *Additive Manufacturing*, vol. 72, p. 103 631, Jun. 2023, ISSN: 22148604. DOI: 10.1016/j.addma.2023.103631. [Online]. Available: https://linkinghub.elsevier.com/retrieve/pii/S2214860423002440.

[17] S. Clijsters, T. Craeghs, S. Buls, K. Kempen, and J. P. Kruth, "In situ quality control of the selective laser melting process using a high-speed, real-time melt pool monitoring system," *International Journal of Advanced Manufacturing Technology*, vol. 75, no. 5-8, pp. 1089–1101, Oct. 2014, ISSN: 14333015. DOI: 10.1007/s00170-014-6214-8. [Online]. Available: https://link.springer.com/article/10.1007/s00170-014-6214-8.

[18] "ASTM INTERNATIONAL Additive Manufacturing Center of Excellence Strategic Guide: Additive Manufacturing In-Situ Monitoring Technology Readiness Findings and Path Forward for Applications in Qualification and Certification," Tech. Rep. [Online]. Available: www.amcoe.org.

[19] W. H. Kan, L. N. S. Chiu, C. V. S. Lim, *et al.*, *A critical review on the effects of process-induced porosity on the mechanical properties of alloys fabricated by laser powder bed fusion*, Jun. 2022. DOI: 10.1007/s10853-022-06990-7.

[20] A. Mostafaei, C. Zhao, Y. He, *et al.*, "Defects and anomalies in powder bed fusion metal additive manufacturing," *Current Opinion in Solid State and*

Materials Science, vol. 26, no. 2, Apr. 2022, ISSN: 13590286. DOI: 10.1016/J.COSSMS.2021.100974.

[21] A. Jones, M. Leary, S. Bateman, and M. Easton, "Effect of surface geometry on laser powder bed fusion defects," *Journal of Materials Processing Technology*, vol. 296, Oct. 2021, ISSN: 09240136. DOI: 10.1016/j.jmatprotec.2021.117179.

[22] "ISO/ASTM 52911-1:2019(E) Additive manufacturing — Design — Part 1: Laser-based powder bed fusion of metals," [Online]. Available: www.sis.se.

[23] *European Powder Metallurgy Association (EPMA) - Introduction to Additive Manufacturing Technology (Brochure)*, 2019. [Online]. Available: https://www.epma.com/epma-free-publications/product/introduction-to-additive-manufacturing-brochure.

[24] E. Toyserkani, D. Sarker, O. O. Ibhadode, F. Liravi, P. Russo, and K. Taherkhani, "Metal Additive Manufacturing," Dec. 2021. DOI: 10.1002/9781119210801. [Online]. Available: https://onlinelibrary.wiley.com/doi/book/10.1002/9781119210801.

[25] M. Grasso and B. M. Colosimo, "Process defects and in situ monitoring methods in metal powder bed fusion: A review," *Measurement Science and Technology*, vol. 28, no. 4, aa5c4f, 2017, ISSN: 13616501. DOI: 10.1088/1361-6501/aa5c4f. [Online]. Available: https://doi.org/10.1088/1361-6501/aa5c4f.

[26] B. Zhang, Y. Li, and Q. Bai, "Defect Formation Mechanisms in Selective Laser Melting: A Review," *Chinese Journal of Mechanical Engineering (English Edition)*, vol. 30, no. 3, pp. 515–527, May 2017, ISSN: 21928258. DOI: 10.1007/S10033-017-0121-5.

[27] E. Malekipour and H. El-Mounayri, "Common defects and contributing parameters in powder bed fusion AM process and their classification for online monitoring and control: a review," *International Journal of Advanced Manufacturing Technology*, vol. 95, no. 1-4, pp. 527–550, Mar. 2018, ISSN: 14333015. DOI: 10.1007/S00170-017-1172-6.

[28] B. Dutton, W. Vesga, J. Waller, S. James, and M. Seifi, "Metal additive manufacturing defect formation and nondestructive evaluation detectability," in *ASTM Special Technical Publication*, vol. STP 1620, ASTM International, 2020, pp. 1–50, ISBN: 9780803176867. DOI: 10.1520/STP162020180136.

[29] S. Tammas-Williams, P. J. Withers, I. Todd, and P. B. Prangnell, "The Influence of Porosity on Fatigue Crack Initiation in Additively Manufactured Titanium Components," *Scientific Reports 2017 7:1*, vol. 7, no. 1, pp. 1–13, Aug. 2017, ISSN: 2045-2322. DOI: 10.1038/s41598-017-06504-5. [Online]. Available: https://www.nature.com/articles/s41598-017-06504-5.

[30] P. Beiss and M. Dalgic, "Structure property relationships in porous sintered steels," *Materials Chemistry and Physics*, vol. 67, no. 1-3, pp. 37–42, Jan. 2001, ISSN: 02540584. DOI: 10.1016/S0254-0584(00)00417-X. [Online]. Available: https://linkinghub.elsevier.com/retrieve/pii/S025405840000417X.

[31] S. Beretta and S. Romano, "A comparison of fatigue strength sensitivity to defects for materials manufactured by AM or traditional processes," *Inter-*

national Journal of Fatigue, vol. 94, pp. 178–191, Jan. 2017, ISSN: 01421123. DOI: 10.1016/j.ijfatigue.2016.06.020. [Online]. Available: https://linkinghub.elsevier.com/retrieve/pii/S0142112316301645.

[32] S. Tammas-Williams, H. Zhao, F. Léonard, F. Derguti, I. Todd, and P. B. Prangnell, "XCT analysis of the influence of melt strategies on defect population in Ti–6Al–4V components manufactured by Selective Electron Beam Melting," *Materials Characterization*, vol. 102, pp. 47–61, Apr. 2015, ISSN: 1044-5803. DOI: 10.1016/J.MATCHAR.2015.02.008.

[33] N. T. Aboulkhair, N. M. Everitt, I. Ashcroft, and C. Tuck, "Reducing porosity in AlSi10Mg parts processed by selective laser melting," *Additive Manufacturing*, vol. 1-4, pp. 77–86, Oct. 2014, ISSN: 22148604. DOI: 10.1016/j.addma.2014.08.001. [Online]. Available: https://linkinghub.elsevier.com/retrieve/pii/S2214860414000062.

[34] C. L. A. Leung, S. Marussi, M. Towrie, R. C. Atwood, P. J. Withers, and P. D. Lee, "The effect of powder oxidation on defect formation in laser additive manufacturing," *Acta Materialia*, vol. 166, pp. 294–305, Mar. 2019, ISSN: 13596454. DOI: 10.1016/j.actamat.2018.12.027. [Online]. Available: https://linkinghub.elsevier.com/retrieve/pii/S1359645418309698.

[35] R. Cunningham, S. P. Narra, C. Montgomery, J. Beuth, and A. D. Rollett, "Synchrotron-Based X-ray Microtomography Characterization of the Effect of Processing Variables on Porosity Formation in Laser Power-Bed Additive Manufacturing of Ti-6Al-4V," *JOM*, vol. 69, no. 3, pp. 479–484, Mar. 2017, ISSN: 15431851. DOI: 10.1007/S11837-016-2234-1. [Online]. Available: https://www.researchgate.net/publication/312051675_Synchrotron-Based_X-ray_Microtomography_Characterization_of_the_Effect_of_Processing_Variables_on_Porosity_Formation_in_Laser_Power-Bed_Additive_Manufacturing_of_Ti-6Al-4V.

[36] W. E. King, H. D. Barth, V. M. Castillo, *et al.*, "Observation of keyhole-mode laser melting in laser powder-bed fusion additive manufacturing," *Journal of Materials Processing Technology*, vol. 214, no. 12, pp. 2915–2925, 2014, ISSN: 09240136. DOI: 10.1016/J.JMATPROTEC.2014.06.005. [Online]. Available: https://www.researchgate.net/publication/264826812_Observation_of_keyhole-mode_laser_melting_in_laser_powder-bed_fusion_additive_manufacturing.

[37] M. Tang, P. C. Pistorius, S. Narra, and J. L. Beuth, "Rapid Solidification: Selective Laser Melting of AlSi10Mg," *JOM*, vol. 68, no. 3, pp. 960–966, Mar. 2016, ISSN: 15431851. DOI: 10.1007/S11837-015-1763-3. [Online]. Available: https://www.researchgate.net/publication/289367514_Rapid_Solidification_Selective_Laser_Melting_of_AlSi10Mg.

[38] R. Molaei, A. Fatemi, and N. Phan, "Significance of hot isostatic pressing (HIP) on multiaxial deformation and fatigue behaviors of additive manufactured Ti-6Al-4V including build orientation and surface roughness effects," *International Journal of Fatigue*, vol. 117, pp. 352–370, Dec. 2018, ISSN: 01421123. DOI: 10.1016/J.IJFATIGUE.2018.07.035.

[39] E. J. Schwalbach, S. P. Donegan, M. G. Chapman, K. J. Chaput, and M. A. Groeber, "A discrete source model of powder bed fusion additive manufac-

turing thermal history," *Additive Manufacturing*, vol. 25, pp. 485–498, Jan. 2019, ISSN: 2214-8604. DOI: 10.1016/J.ADDMA.2018.12.004.

[40] M. Tang, P. C. Pistorius, and J. L. Beuth, "Prediction of lack-of-fusion porosity for powder bed fusion," *Additive Manufacturing*, vol. 14, pp. 39–48, Mar. 2017, ISSN: 22148604. DOI: 10.1016/j.addma.2016.12.001. [Online]. Available: https://linkinghub.elsevier.com/retrieve/pii/S2214860416300471.

[41] H. Gong, "Generation and detection of defects in metallic parts fabricated by selective laser melting and electron beam melting and their effects on mechanical properties.," 2013. DOI: 10.18297/ETD/515. [Online]. Available: http://ir.library.louisville.edu/etd/515.

[42] A. R. Nassar, M. A. Gundermann, E. W. Reutzel, P. Guerrier, M. H. Krane, and M. J. Weldon, "Formation processes for large ejecta and interactions with melt pool formation in powder bed fusion additive manufacturing," *Scientific Reports 2019 9:1*, vol. 9, no. 1, pp. 1–11, Mar. 2019, ISSN: 2045-2322. DOI: 10.1038/s41598-019-41415-7. [Online]. Available: https://www.nature.com/articles/s41598-019-41415-7.

[43] A. B. Anwar and Q.-C. Pham, "Study of the spatter distribution on the powder bed during selective laser melting," *Additive Manufacturing*, vol. 22, pp. 86–97, Aug. 2018, ISSN: 22148604. DOI: 10.1016/j.addma.2018.04.036. [Online]. Available: https://linkinghub.elsevier.com/retrieve/pii/S2214860418300897.

[44] S. Li, G. Chen, S. Katayama, and Y. Zhang, "Relationship between spatter formation and dynamic molten pool during high-power deep-penetration laser welding," *Applied Surface Science*, vol. 303, pp. 481–488, Jun. 2014, ISSN: 0169-4332. DOI: 10.1016/J.APSUSC.2014.03.030.

[45] J. Trapp, A. M. Rubenchik, G. Guss, and M. J. Matthews, "In situ absorptivity measurements of metallic powders during laser powder-bed fusion additive manufacturing," *Applied Materials Today*, vol. 9, pp. 341–349, Dec. 2017, ISSN: 2352-9407. DOI: 10.1016/J.APMT.2017.08.006.

[46] B. Ferrar, L. Mullen, E. Jones, R. Stamp, and C. J. Sutcliffe, "Gas flow effects on selective laser melting (SLM) manufacturing performance," *Journal of Materials Processing Technology*, vol. 212, no. 2, pp. 355–364, Feb. 2012, ISSN: 0924-0136. DOI: 10.1016/J.JMATPROTEC.2011.09.020.

[47] B. Foster, E. Reutzel, A. Nassar, B. Hall, S. Brown, and C. Dickman, "Optical, Layerwise Monitoring of Powder Bed Fusion," 2015. [Online]. Available: https://repositories.lib.utexas.edu/handle/2152/89328.

[48] W. Hong, Y. T. Lee, and H. Gong, "A study of the staircase effect induced by material shrinkage in rapid prototyping," *Rapid Prototyping Journal*, vol. 11, no. 2, pp. 82–89, 2005, ISSN: 13552546. DOI: 10.1108/13552540510589449. [Online]. Available: https://www.researchgate.net/publication/235293769_A_study_of_the_staircase_effect_induced_by_material_shrinkage_in_rapid_prototyping.

[49] L. A. Parry, I. A. Ashcroft, and R. D. Wildman, "Geometrical effects on residual stress in selective laser melting," *Additive Manufacturing*, vol. 25,

pp. 166–175, Jan. 2019, ISSN: 2214-8604. DOI: 10.1016/J.ADDMA.2018.09.026.

[50] P. Prabhakar, W. J. Sames, R. Dehoff, and S. S. Babu, "Computational modeling of residual stress formation during the electron beam melting process for Inconel 718," *Additive Manufacturing*, vol. 7, pp. 83–91, Jul. 2015, ISSN: 2214-8604. DOI: 10.1016/J.ADDMA.2015.03.003.

[51] B. Cheng, S. Shrestha, and K. Chou, "Stress and deformation evaluations of scanning strategy effect in selective laser melting," *Additive Manufacturing*, vol. 12, pp. 240–251, Oct. 2016, ISSN: 2214-8604. DOI: 10.1016/J.ADDMA.2016.05.007.

[52] R. Li, J. Liu, Y. Shi, L. Wang, and W. Jiang, "Balling behavior of stainless steel and nickel powder during selective laser melting process," *International Journal of Advanced Manufacturing Technology*, vol. 59, no. 9-12, pp. 1025–1035, Apr. 2012, ISSN: 02683768. DOI: 10.1007/S00170-011-3566-1/METRICS. [Online]. Available: https://link.springer.com/article/10.1007/s00170-011-3566-1.

[53] J. C. Fox, S. P. Moylan, and B. M. Lane, "Effect of Process Parameters on the Surface Roughness of Overhanging Structures in Laser Powder Bed Fusion Additive Manufacturing," *Procedia CIRP*, vol. 45, pp. 131–134, Jan. 2016, ISSN: 2212-8271. DOI: 10.1016/J.PROCIR.2016.02.347.

[54] J. Delgado, J. Ciurana, and C. A. Rodríguez, "Influence of process parameters on part quality and mechanical properties for DMLS and SLM with iron-based materials," *International Journal of Advanced Manufacturing Technology*, vol. 60, no. 5-8, pp. 601–610, May 2012, ISSN: 02683768. DOI: 10.1007/S00170-011-3643-5/METRICS. [Online]. Available: https://link.springer.com/article/10.1007/s00170-011-3643-5.

[55] K. Solberg, E. W. Hovig, K. Sørby, and F. Berto, "Directional fatigue behaviour of maraging steel grade 300 produced by laser powder bed fusion," *International Journal of Fatigue*, vol. 149, p. 106 229, Aug. 2021, ISSN: 0142-1123. DOI: 10.1016/J.IJFATIGUE.2021.106229.

[56] C. Qiu, C. Panwisawas, M. Ward, H. C. Basoalto, J. W. Brooks, and M. M. Attallah, "On the role of melt flow into the surface structure and porosity development during selective laser melting," *Acta Materialia*, vol. 96, pp. 72–79, Sep. 2015, ISSN: 1359-6454. DOI: 10.1016/J.ACTAMAT.2015.06.004.

[57] M. Jamshidinia and R. Kovacevic, "The influence of heat accumulation on the surface roughness in powder-bed additive manufacturing," *Surface Topography: Metrology and Properties*, vol. 3, no. 1, Jan. 2015, ISSN: 2051672X. DOI: 10.1088/2051-672X/3/1/014003. [Online]. Available: https://www.researchgate.net/publication/271966401_The_influence_of_heat_accumulation_on_the_surface_roughness_in_powder-bed_additive_manufacturing.

[58] D. Gu and Y. Shen, "Balling phenomena in direct laser sintering of stainless steel powder: Metallurgical mechanisms and control methods," *Materials and Design*, vol. 30, no. 8, pp. 2903–2910, Sep. 2009, ISSN: 02641275. DOI: 10.1016/J.MATDES.2009.01.013. [Online]. Available: https://www.researchgate.net/publication/223884995_Balling_phenomena_in_

direct_laser_sintering_of_stainless_steel_powder_Metallurgical_mechanisms_and_control_methods.

[59] S. Chandrasekhar, "Hydrodynamic and Hydromagnetic Stability," *Oxford University Press, 1961. 652 pp.*, vol. 1, p. 652, 1961, ISSN: 1469-7645. DOI: 10.1017/S0022112062210592.

[60] A. Giorgetti, A. Girgenti, P. Citti, and M. Delogu, "A novel approach for axiomatic-based design for the environment," *Axiomatic Design in Large Systems: Complex Products, Buildings and Manufacturing Systems*, pp. 131–148, Jan. 2016. DOI: 10.1007/978-3-319-32388-6{_}5/COVER. [Online]. Available: https://link.springer.com/chapter/10.1007/978-3-319-32388-6_5.

[61] M. K. Thompson, G. Moroni, T. Vaneker, *et al.*, "Design for Additive Manufacturing: Trends, opportunities, considerations, and constraints," *CIRP Annals*, vol. 65, no. 2, pp. 737–760, Jan. 2016, ISSN: 0007-8506. DOI: 10.1016/J.CIRP.2016.05.004.

[62] I. Gibson, D. Rosen, B. Stucker, and M. Khorasani, "Design for Additive Manufacturing," *Additive Manufacturing Technologies*, pp. 555–607, 2021. DOI: 10.1007/978-3-030-56127-7{_}19. [Online]. Available: https://link.springer.com/chapter/10.1007/978-3-030-56127-7_19.

[63] E. Komi, "Design for Additive Manufacturing," Tech. Rep., 2016. [Online]. Available: https://publications.vtt.fi/julkaisut/muut/2016/VTT-R-03159-16.pdf.

[64] F. Ceccanti, A. Giorgetti, G. Arcidiacono, and P. Citti, "Laser Powder Bed Fusion: A Review on the Design Constraints," *IOP Conference Series: Materials Science and Engineering*, vol. 1038, no. 1, p. 012 065, Feb. 2021, ISSN: 1757-899X. DOI: 10.1088/1757-899X/1038/1/012065. [Online]. Available: https://iopscience.iop.org/article/10.1088/1757-899X/1038/1/012065%20https://iopscience.iop.org/article/10.1088/1757-899X/1038/1/012065/meta.

[65] L. Rebaioli and I. Fassi, "A review on benchmark artifacts for evaluating the geometrical performance of additive manufacturing processes," *International Journal of Advanced Manufacturing Technology*, vol. 93, no. 5-8, pp. 2571–2598, Nov. 2017, ISSN: 14333015. DOI: 10.1007/S00170-017-0570-0/METRICS. [Online]. Available: https://link.springer.com/article/10.1007/s00170-017-0570-0.

[66] Z. Wu, S. P. Narra, and A. Rollett, "Exploring the fabrication limits of thin-wall structures in a laser powder bed fusion process," DOI: 10.1007/s00170-020-05827-4/Published. [Online]. Available: https://doi.org/10.1007/s00170-020-05827-4.

[67] H. Yang, J. Yang, W. Huang, Z. Wang, and X. Zeng, "The printability, microstructure, crystallographic features and microhardness of selective laser melted Inconel 718 thin wall," *Materials & Design*, vol. 156, pp. 407–418, Oct. 2018, ISSN: 0264-1275. DOI: 10.1016/J.MATDES.2018.07.007.

[68] D. Herzog, K. Asami, and C. Scholl, "Design guidelines for laser powder bed fusion in Inconel 718," *J. Laser Appl*, vol. 34, p. 12 015, 2022. DOI: 10.2351/7.0000508. [Online]. Available: https://doi.org/10.2351/7.0000508.

[69] T. Dahmen, W. A. Edgar Alphonso Danfoss, C. G. Klingaa, and V. Karthik Nadimpalli, "Evaluating the scalability of channels made by Binder Jetting and Laser Powder Bed Fusion using an X-ray CT and image analysis approach .," Tech. Rep., 2022. [Online]. Available: https://www.researchgate.net/publication/363586249.

[70] C. G. Klingaa, M. K. Bjerre, S. Mohanty, *et al.*, "Roughness Investigation of SLM Manufactured Conformal Cooling Channels Using X-ray Computed Tomography Engineering Computational Modeling of Nanoscale Phenomena View project Laser Based-Powder Bed Fusion of Pure Copper View project Roughness Investigation of SLM Manufactured Conformal Cooling Channels Using X-ray Computed Tomography," Tech. Rep. DOI: https://doi.org/10.58286/23739. [Online]. Available: https://www.researchgate.net/publication/331011133.

[71] D. Wang, S. Wu, Y. Bai, H. Lin, Y. Yang, and C. Song, "Characteristics of typical geometrical features shaped by selective laser melting," *Journal of Laser Applications*, vol. 29, no. 2, p. 022 007, May 2017, ISSN: 1042-346X. DOI: 10.2351/1.4980164.

[72] J. Kranz, D. Herzog, and C. Emmelmann, "Design guidelines for laser additive manufacturing of lightweight structures in TiAl6V4," *Journal of Laser Applications*, vol. 27, no. S1, S14001, Dec. 2014, ISSN: 1042-346X. DOI: 10.2351/1.4885235. [Online]. Available: https://lia.scitation.org/doi/abs/10.2351/1.4885235.

[73] C. Yan, L. Hao, A. Hussein, and D. Raymont, "Evaluations of cellular lattice structures manufactured using selective laser melting," *International Journal of Machine Tools and Manufacture*, vol. 62, pp. 32–38, Nov. 2012, ISSN: 0890-6955. DOI: 10.1016/J.IJMACHTOOLS.2012.06.002.

[74] F. Zanini, M. Sorgato, E. Savio, and S. Carmignato, "Dimensional verification of metal additively manufactured lattice structures by X-ray computed tomography: Use of a newly developed calibrated artefact to achieve metrological traceability," *Additive Manufacturing*, vol. 47, Nov. 2021, ISSN: 22148604. DOI: 10.1016/j.addma.2021.102229.

[75] C. Gobert, E. W. Reutzel, J. Petrich, A. R. Nassar, and S. Phoha, "Application of supervised machine learning for defect detection during metallic powder bed fusion additive manufacturing using high resolution imaging.," *Additive Manufacturing*, vol. 21, no. April, pp. 517–528, 2018, ISSN: 22148604. DOI: 10.1016/j.addma.2018.04.005. [Online]. Available: https://doi.org/10.1016/j.addma.2018.04.005.

[76] R. McCann, M. A. Obeidi, C. Hughes, *et al.*, *In-situ sensing, process monitoring and machine control in Laser Powder Bed Fusion: A review*, Sep. 2021. DOI: 10.1016/j.addma.2021.102058.

[77] J. Petrich, C. Gobert, S. Phoha, A. R. Nassar, and E. W. Reutzel, "Machine learning for defect detection for PBFAm using high resolution layerwise imaging coupled with post-build CT scans," *Solid Freeform Fabrication 2017: Proceedings of the 28th Annual International Solid Freeform Fabrication Symposium - An Additive Manufacturing Conference, SFF 2017*, no. 814, pp. 1363–1381, 2020. DOI: https://hdl.handle.net/2152/89950.

[78] C. Schwerz and L. Nyborg, "A neural network for identification and classification of systematic internal flaws in laser powder bed fusion," *CIRP Journal of Manufacturing Science and Technology*, vol. 37, pp. 312–318, 2022, ISSN: 1755-5817. DOI: 10.1016/J.CIRPJ.2022.02.010. [Online]. Available: https://linkinghub.elsevier.com/retrieve/pii/S1755581722000347.

[79] T. Craeghs, S. Clijsters, E. Yasa, and J.-P. Kruth, "Online Quality Control of Selective Laser Melting," in *International Solid Freeform Fabrication Symposium*, 2011. DOI: 10.26153/tsw/15289. [Online]. Available: http://dx.doi.org/10.26153/tsw/15289.

[80] T. Furumoto, M. R. Alkahari, T. Ueda, M. S. A. Aziz, and A. Hosokawa, "Monitoring of Laser Consolidation Process of Metal Powder with High Speed Video Camera," in *Physics Procedia*, vol. 39, Elsevier B.V., 2012, pp. 760–766. DOI: 10.1016/j.phpro.2012.10.098.

[81] K. Taherkhani, E. Sheydaeian, C. Eischer, M. Otto, and E. Toyserkani, "Development of a defect-detection platform using photodiode signals collected from the melt pool of laser powder-bed fusion," *Additive Manufacturing*, vol. 46, Oct. 2021, ISSN: 22148604. DOI: 10.1016/J.ADDMA.2021.102152.

[82] Y. Zhang, P. Zhang, X. Jiang, S. Zhang, K. Zhong, and Z. Li, "In-situ 3D contour measurement for laser powder bed fusion based on phase guidance," *Theoretical and Applied Mechanics Letters*, Mar. 2023, ISSN: 20950349. DOI: 10.1016/j.taml.2022.100405.

[83] I. Yadroitsev, P. Krakhmalev, and I. Yadroitsava, "Selective laser melting of Ti6Al4V alloy for biomedical applications: Temperature monitoring and microstructural evolution," *Journal of Alloys and Compounds*, vol. 583, pp. 404–409, Jan. 2014, ISSN: 09258388. DOI: 10.1016/j.jallcom.2013.08.183.

[84] H. Krauss, T. Zeugner, and M. F. Zaeh, "Layerwise monitoring of the Selective Laser Melting process by thermography," in *Physics Procedia*, vol. 56, Elsevier B.V., 2014, pp. 64–71. DOI: 10.1016/j.phpro.2014.08.097.

[85] N. H. Paulson, B. Gould, S. J. Wolff, M. Stan, and A. C. Greco, "Correlations between thermal history and keyhole porosity in laser powder bed fusion," *Additive Manufacturing*, vol. 34, Aug. 2020, ISSN: 22148604. DOI: 10.1016/j.addma.2020.101213.

[86] H. Baumgartl, J. Tomas, R. Buettner, and M. Merkel, "A deep learning-based model for defect detection in laser-powder bed fusion using in-situ thermographic monitoring," *Progress in Additive Manufacturing*, vol. 5, no. 3, pp. 277–285, Sep. 2020, ISSN: 23639520. DOI: 10.1007/s40964-019-00108-3. [Online]. Available: https://doi.org/10.1007/s40964-019-00108-3.

[87] C. Van Gestel, "Study of physical phenomena of selective laser melting towards increased productivity," Tech. Rep., 2015. DOI: 10.5075/EPFL-THESIS-6817. [Online]. Available: https://doi.org/10.5075/EPFL-THESIS-6817.

[88] M. A. Mahmood, F. G. Alabtah, Y. Al-Hamidi, and M. Khraisheh, *On the laser additive manufacturing of high-entropy alloys: A critical assessment of in-situ monitoring techniques and their suitability*, Feb. 2023. DOI: 10.1016/j.matdes.2023.111658.

[89] W. " Guo, Q. Tian, S. Guo, and Y. Guo, "A physics-driven deep learning model for process-porosity causal relationship and porosity prediction

with interpretability in laser metal deposition," *CIRP Annals*, vol. 69, no. 1, pp. 205–208, Jan. 2020, ISSN: 17260604. DOI: 10.1016/j.cirp.2020.04.049.

[90] J. B. Forien, N. P. Calta, P. J. DePond, G. M. Guss, T. T. Roehling, and M. J. Matthews, "Detecting keyhole pore defects and monitoring process signatures during laser powder bed fusion: A correlation between in situ pyrometry and ex situ X-ray radiography," *Additive Manufacturing*, vol. 35, Oct. 2020, ISSN: 22148604. DOI: 10.1016/j.addma.2020.101336.

[91] U. Thombansen, A. Gatej, and M. Pereira, "Process observation in fiber laser–based selective laser melting," *Optical Engineering*, vol. 54, no. 1, p. 011 008, Oct. 2014, ISSN: 0091-3286. DOI: 10.1117/1.oe.54.1.011008.

[92] A. Neef, V. Seyda, D. Herzog, C. Emmelmann, M. Schönleber, and M. Kogel-Hollacher, "Low coherence interferometry in selective laser melting," in *Physics Procedia*, vol. 56, Elsevier B.V., 2014, pp. 82–89. DOI: 10.1016/j.phpro.2014.08.100.

[93] J. A. Kanko, A. P. Sibley, and J. M. Fraser, "In situ morphology-based defect detection of selective laser melting through inline coherent imaging," *Journal of Materials Processing Technology*, vol. 231, pp. 488–500, May 2016, ISSN: 09240136. DOI: 10.1016/j.jmatprotec.2015.12.024.

[94] C. Zhao, K. Fezzaa, R. W. Cunningham, *et al.*, "Real-time monitoring of laser powder bed fusion process using high-speed X-ray imaging and diffraction," *Scientific Reports*, vol. 7, no. 1, Dec. 2017, ISSN: 20452322. DOI: 10.1038/s41598-017-03761-2.

[95] A. Thompson, I. Maskery, and R. K. Leach, *X-ray computed tomography for additive manufacturing: A review*, Jun. 2016. DOI: 10.1088/0957-0233/27/7/072001.

[96] H. Rieder, A. Dillhöfer, M. Spies, J. Bamberg, and T. Hess, "Online Monitoring of Additive Manufacturing Processes Using Ultrasound," Tech. Rep. [Online]. Available: www.ndt.net/?id=16533.

[97] D. Ye, G. S. Hong, Y. Zhang, K. Zhu, and J. Y. H. Fuh, "Defect detection in selective laser melting technology by acoustic signals with deep belief networks," *International Journal of Advanced Manufacturing Technology*, vol. 96, no. 5-8, pp. 2791–2801, May 2018, ISSN: 14333015. DOI: 10.1007/s00170-018-1728-0.

[98] Y. AbouelNour and N. Gupta, "In-situ monitoring of sub-surface and internal defects in additive manufacturing: A review," *Materials & Design*, vol. 222, p. 111 063, Oct. 2022, ISSN: 0264-1275. DOI: 10.1016/J.MATDES.2022.111063.

[99] S. J. Foster, K. Carver, R. B. Dinwiddie, *et al.*, "Process-Defect-Structure-Property Correlations During Laser Powder Bed Fusion of Alloy 718: Role of In Situ and Ex Situ Characterizations," *Metallurgical and Materials Transactions A: Physical Metallurgy and Materials Science*, vol. 49, no. 11, pp. 5775–5798, Nov. 2018, ISSN: 10735623. DOI: 10.1007/s11661-018-4870-2.

[100] I. Segovia Ramírez, F. P. García Márquez, and M. Papaelias, "Review on additive manufacturing and non-destructive testing," *Journal of Manufacturing Systems*, vol. 66, pp. 260–286, Feb. 2023, ISSN: 0278-6125. DOI: 10.1016/J.JMSY.2022.12.005.

[101] J. M. Waller, B. H. Parker, K. L. Hodges, E. R. Burke, J. L. Walker, and E. R. Generazio, *Nondestructive Evaluation of Additive Manufacturing State-of-the-Discipline Report*, 2014. [Online]. Available: http://www.sti.nasa.gov.

[102] G. Mohr, S. J. Altenburg, A. Ulbricht, *et al.*, "In-situ defect detection in laser powder bed fusion by using thermography and optical tomography—comparison to computed tomography," *Metals*, vol. 10, no. 1, Jan. 2020, ISSN: 20754701. DOI: 10.3390/met10010103.

[103] M. Moshiri, D. B. Pedersen, G. Tosello, and V. K. Nadimpalli, "Performance evaluation of in-situ near-infrared melt pool monitoring during laser powder bed fusion," *Virtual and Physical Prototyping*, vol. 18, no. 1, 2023, ISSN: 17452767. DOI: 10.1080/17452759.2023.2205387.

[104] A. du Plessis and S. G. le Roux, "Standardized X-ray tomography testing of additively manufactured parts: A round robin test," *Additive Manufacturing*, vol. 24, pp. 125–136, Dec. 2018, ISSN: 22148604. DOI: 10.1016/j.addma.2018.09.014.

[105] A. Du Plessis, J. M. Waller, S. G. Le Roux, *et al.*, "X-Ray computed tomography inspection in metal additive manufacturing: The role of witness specimens," in *ASTM Special Technical Publication*, vol. STP 1631, ASTM International, 2020, pp. 139–156, ISBN: 9780803177086. DOI: 10.1520/STP163120190109.

[106] J. A. Slotwinski and E. J. Garboczi, "Porosity of additive manufacturing parts for process monitoring," in *AIP Conference Proceedings*, vol. 1581 33, American Institute of Physics Inc., 2014, pp. 1197–1204, ISBN: 9780735412118. DOI: 10.1063/1.4864957.

[107] N. Kladovasilakis, T. Kontodina, P. Charalampous, I. Kostavelis, D. Tzetzis, and D. Tzovaras, "A case study on 3D scanning, digital reparation and rapid metal additive manufacturing of a centrifugal impeller," in *IOP Conference Series: Materials Science and Engineering*, vol. 1037, IOP Publishing Ltd, Feb. 2021. DOI: 10.1088/1757-899X/1037/1/012018.

[108] M. Javaid, A. Haleem, R. Pratap Singh, and R. Suman, "Industrial perspectives of 3D scanning: Features, roles and it's analytical applications," *Sensors International*, vol. 2, Jan. 2021, ISSN: 26663511. DOI: 10.1016/j.sintl.2021.100114.

[109] L. Du, Y. Lai, C. Luo, *et al.*, "E-quality Control in Dental Metal Additive Manufacturing Inspection Using 3D Scanning and 3D Measurement," *Frontiers in Bioengineering and Biotechnology*, vol. 8, Aug. 2020, ISSN: 22964185. DOI: 10.3389/fbioe.2020.01038.

[110] A. Triantaphyllou, C. L. Giusca, G. D. Macaulay, *et al.*, "Surface texture measurement for additive manufacturing," *Surface Topography: Metrology and Properties*, vol. 3, no. 2, Apr. 2015, ISSN: 2051672X. DOI: 10.1088/2051-672X/3/2/024002.

[111] P. Wang, W. J. Sin, M. L. S. Nai, and J. Wei, "Effects of processing parameters on surface roughness of additive manufactured Ti-6Al-4V via electron beam melting," *Materials*, vol. 10, no. 10, Sep. 2017, ISSN: 19961944. DOI: 10.3390/ma10101121.

[112] U. Ali, H. Fayazfar, F. Ahmed, and E. Toyserkani, "Internal surface roughness enhancement of parts made by laser powder-bed fusion additive manufactur-

ing," *Vacuum*, vol. 177, Jul. 2020, ISSN: 0042207X. DOI: 10.1016/j.vacuum.2020.109314.

[113] A. Charles, A. Elkaseer, L. Thijs, V. Hagenmeyer, and S. Scholz, "Effect of process parameters on the generated surface roughness of down-facing surfaces in selective laser melting," *Applied Sciences (Switzerland)*, vol. 9, no. 6, 2019, ISSN: 20763417. DOI: 10.3390/app9061256.

[114] B. Whip, L. Sheridan, and J. Gockel, "The effect of primary processing parameters on surface roughness in laser powder bed additive manufacturing," *International Journal of Advanced Manufacturing Technology*, vol. 103, no. 9-12, pp. 4411–4422, Aug. 2019, ISSN: 14333015. DOI: 10.1007/s00170-019-03716-z.

[115] J. Gockel, L. Sheridan, B. Koerper, and B. Whip, "The influence of additive manufacturing processing parameters on surface roughness and fatigue life," *International Journal of Fatigue*, vol. 124, pp. 380–388, Jul. 2019, ISSN: 01421123. DOI: 10.1016/j.ijfatigue.2019.03.025.

[116] S. Cooke, K. Ahmadi, S. Willerth, and R. Herring, *Metal additive manufacturing: Technology, metallurgy and modelling*, Sep. 2020. DOI: 10.1016/j.jmapro.2020.07.025.

[117] M. Schmidt, M. Merklein, D. Bourell, *et al.*, "Laser based additive manufacturing in industry and academia," *CIRP Annals*, vol. 66, no. 2, pp. 561–583, 2017, ISSN: 17260604. DOI: 10.1016/j.cirp.2017.05.011.

[118] P. R. Gradl, C. S. Protz, D. L. Ellis, and S. E. Greene, "Progress in Additively Manufactured Copper-Alloy GRCop-84, GRCop-42, and Bimetallic Combustion Chambers for Liquid Rocket Engines," Tech. Rep., 2019.

[119] N. R. Philips, M. Carl, and N. J. Cunningham, "New Opportunities in Refractory Alloys," *Metallurgical and Materials Transactions A: Physical Metallurgy and Materials Science*, vol. 51, no. 7, pp. 3299–3310, Jul. 2020, ISSN: 10735623. DOI: 10.1007/s11661-020-05803-3.

[120] R. R. Boyer, "An overview on the use of titanium in the aerospace industry," *Materials Science and Engineering*, vol. 213, pp. 103–114, 1996. DOI: 10.1016/0921-5093(96)10233-1. [Online]. Available: https://doi.org/10.1016/0921-5093(96)10233-1.

[121] E. Hosseini and V. A. Popovich, "A review of mechanical properties of additively manufactured Inconel 718," *Additive Manufacturing*, vol. 30, p. 100 877, Dec. 2019, ISSN: 2214-8604. DOI: 10.1016/J.ADDMA.2019.100877.

[122] J. Xu, "High-performance Nickel-based Superalloys for Additive Manufacturing," Ph.D. dissertation, Linköping University, 2022, ISBN: 978-91-7929-258-4. DOI: 10.3384/9789179292584.

[123] S. Liu and Y. C. Shin, "Additive manufacturing of Ti6Al4V alloy: A review," *Materials & Design*, vol. 164, p. 107 552, Feb. 2019, ISSN: 0264-1275. DOI: 10.1016/J.MATDES.2018.107552.

[124] G. Lutjering and James C. Williams, "Alpha + Beta Alloys," in *Titanium*, 2007, pp. 203–250. [Online]. Available: https://link.springer.com/chapter/10.1007/978-3-540-73036-1_5#citeas.

[125] T. Zhang and C. T. Liu, *Design of titanium alloys by additive manufacturing: A critical review*, Jan. 2022. DOI: 10.1016/j.apmate.2021.11.001.

[126] H. Galarraga, R. J. Warren, D. A. Lados, R. R. Dehoff, M. M. Kirka, and P. Nandwana, "Effects of heat treatments on microstructure and properties of Ti-6Al-4V ELI alloy fabricated by electron beam melting (EBM)," *Materials Science and Engineering A*, vol. 685, pp. 417–428, Feb. 2017, ISSN: 09215093. DOI: 10.1016/j.msea.2017.01.019.

[127] Y. L. Hao, S. J. Li, and R. Yang, *Biomedical titanium alloys and their additive manufacturing*, Sep. 2016. DOI: 10.1007/s12598-016-0793-5.

[128] Y. Zhai, H. Galarraga, and D. A. Lados, "Microstructure, static properties, and fatigue crack growth mechanisms in Ti-6Al-4V fabricated by additive manufacturing: LENS and EBM," *Engineering Failure Analysis*, vol. 69, pp. 3–14, Nov. 2016, ISSN: 13506307. DOI: 10.1016/j.engfailanal.2016.05.036.

[129] "Premium EOS NickelAlloy IN718 Material Data Sheet Metal Solutions,"

[130] *RenAM 500 series additive manufacturing systems*. [Online]. Available: https://www.renishaw.com/en/renam-500-metal-additive-manufacturing-3d-printing-systems--37011.

[131] L. Fuchs and C. Eischer, "In-process monitoring systems for metal additive manufacturing," Tech. Rep.

[132] *EOS M 290 - Mid-Size 3D Printing*. [Online]. Available: https://www.eos.info/en/industrial-3d-printer/metal/eos-m-290.

[133] *InfiniAM Spectral-Energy input and melt pool emissions monitoring for AM systems*. [Online]. Available: https://www.renishaw.com/en/infiniam-spectral--42310.

[134] T. O. J. Fuchs and R. Hanke, "3D X-ray Tomography - Basics and Latest Developments," in *Handbook of Advanced Non-Destructive Evaluation*, Springer International Publishing, 2018, pp. 1–14. DOI: 10.1007/978-3-319-30050-4{_}22-1.

[135] J. Kastner and C. Heinzl, "X-Ray Tomography," in *Handbook of Advanced Nondestructive Evaluation*, Cham: Springer International Publishing, 2020, pp. 1–73. DOI: 10.1007/978-3-319-30050-4{_}5-2. [Online]. Available: https://link.springer.com/10.1007/978-3-319-30050-4_5-2.

[136] *Phoenix Vtomex M300*. [Online]. Available: https://www.bakerhughes.com/waygate-technologies/industrial-radiography-and-ct/phoenix-advanced-industrial-xray-and-ct/phoenix-vtomex-m-high-speed-3d-ct-scanner.

[137] C. Schwerz, A. Raza, X. Lei, L. Nyborg, E. Hryha, and H. Wirdelius, "In-situ detection of redeposited spatter and its influence on the formation of internal flaws in laser powder bed fusion," *Additive Manufacturing*, p. 102 370, Oct. 2021, ISSN: 2214-8604. DOI: 10.1016/J.ADDMA.2021.102370. [Online]. Available: https://linkinghub.elsevier.com/retrieve/pii/S2214860421005248.

[138] T. Huynh, A. Mehta, K. Graydon, *et al.*, "Microstructural Development in Inconel 718 Nickel-Based Superalloy Additively Manufactured by Laser Powder Bed Fusion," *Metallography, Microstructure, and Analysis*, vol. 11, no. 1, pp. 88–107, Feb. 2022, ISSN: 21929270. DOI: https://doi.org/10.1007/s13632-021-00811-0.

[139] F. G. Fischer, M. G. Zimmermann, N. Praetzsch, and C. Knaak, "Monitoring of the powder bed quality in metal additive manufacturing using deep transfer learning," *Materials and Design*, vol. 222, Oct. 2022, ISSN: 18734197. DOI: 10.1016/j.matdes.2022.111029.

[140] L. Scime and J. Beuth, "Anomaly detection and classification in a laser powder bed additive manufacturing process using a trained computer vision algorithm," *Additive Manufacturing*, vol. 19, pp. 114–126, Jan. 2018, ISSN: 22148604. DOI: 10.1016/j.addma.2017.11.009.

[141] M. Listl, *(3) Optimizing Quality & Productivity for Thin-Walled Parts | LinkedIn*. [Online]. Available: https://www.linkedin.com/pulse/optimizing-quality-productivity-thin-walled-parts-marek-listl/.

[142] G. Dursun, B. Pehlivanogullari, C. Sen, and A. Orhangul, "An investigation upon overhang zones by using finite element modelling and in-situ monitoring systems," in *Procedia CIRP*, vol. 93, Elsevier B.V., 2020, pp. 1253–1258. DOI: 10.1016/j.procir.2020.04.118.

[143] E. Yasa, J. Deckers, T. Craeghs, M. Badrossamay, and J.-P. Kruth, "Investigation on occurence of elevated edges in selective laser melting," in *International Solid Freeform Fabrication Symposium*, 2009. DOI: http://dx.doi.org/10.26153/tsw/15099. [Online]. Available: https://repositories.lib.utexas.edu/handle/2152/88158.

[144] A. Fardan, U. Klement, H. Brodin, and E. Hryha, "Effect of Part Thickness and Build Angle on the Microstructure, Surface Roughness, and Mechanical Properties of Additively Manufactured IN-939," *Metallurgical and Materials Transactions A: Physical Metallurgy and Materials Science*, May 2022, ISSN: 10735623. DOI: 10.1007/s11661-022-06940-7.

[145] X. Han, H. Zhu, X. Nie, G. Wang, and X. Zeng, "Investigation on selective laser melting AlSi10Mg cellular lattice strut: Molten pool morphology, surface roughness and dimensional accuracy," *Materials*, vol. 11, no. 3, Mar. 2018, ISSN: 19961944. DOI: 10.3390/ma11030392.

[146] S. Feng, S. Chen, A. M. Kamat, R. Zhang, M. Huang, and L. Hu, "Investigation on shape deviation of horizontal interior circular channels fabricated by laser powder bed fusion," *Additive Manufacturing*, vol. 36, Dec. 2020, ISSN: 22148604. DOI: 10.1016/j.addma.2020.101585.

[147] H. Zhou, H. Su, Y. Guo, *et al.*, "Formation and Evolution of Surface Morphology in Overhang Structure of IN718 Superalloy Fabricated by Laser Powder Bed Fusion," *Acta Metallurgica Sinica (English Letters)*, pp. 1–21, Mar. 2023, ISSN: 21941289. DOI: 10.1007/S40195-023-01546-3/METRICS. [Online]. Available: https://link.springer.com/article/10.1007/s40195-023-01546-3.

A

Appendix

A.1 Appendix 1

Matlab code for the heatmap generation from laser intensity text files. Credited to Erik Henrikson for helping with the code.

```
%% Preamble
% Imports a lot of data to make a neat picture

%Specify the length of one side of the square buildplate
buildPlateSize = 250; % [mm]

res = 1000; % resolution

% intentional over-exposure
cutoff = 100; % [%]
```

```
%% Load data for all layers
filePattern = fullfile(pwd, '*.txt');
txtFiles = dir(filePattern);
numFiles = length(txtFiles);

outputFolder = fullfile(pwd, 'output');

% Sort files alphabetically based on their names
[~, sortIndex] = sort({txtFiles.name});
txtFiles = txtFiles(sortIndex);

for k = 1 : numFiles
```

```
    % Get the file name and load the data
    fileName = txtFiles(k).name;
    data = importdata(fileName, '\t', 1);
    layer = str2double(extractBetween(fileName, "Packet data for layer ", ", laser 4.txt"));

    x = round(data.data(:, 3)*res/buildPlateSize + res/2); %[1/10 mm]
    y = round(data.data(:, 4)*res/buildPlateSize + res/2); %[1/10 mm]
    pwr = data.data(:, 7);
```

```
    %% Plot
    fig = figure('visible', 'off'); % Create a new figure window for each layer
    map = zeros(res);
    for i = 1:length(pwr)
        map(x(i),y(i)) = map(x(i),y(i)) + pwr(i);
    end

    imagesc(map,[0 (cutoff/100)*max(map,[],'all')])
    title(strcat('Layer-',num2str(layer),' res-',num2str(res),'x',num2str(res),' cutoff-',num2str(cutoff),'%'))
    axis image

    % Save the heatmap as a PNG image
    imageName = strcat('Layer-',num2str(layer),'-res-',num2str(res),'x',num2str(res),'-cutoff-',num2str(cutoff),'%.png');
    imagePath = fullfile(outputFolder, imageName);
    saveas(fig, imagePath);
    close(fig);
```

```
end
```

Figure A.1: Matlab code used to generate heatmaps from laser spectral data.

A.2 Appendix 2

Python code used to generate the RMSE plot for the PB images.

```
import glob
import os
import cv2
import re
import numpy as np
import matplotlib.pyplot as plt
import mpld3
from mpld3 import plugins

# Define function to calculate RMS between two images
def rms_diff(img1, img2):
    diff = img1.astype(np.int32) - img2.astype(np.int32)
    rms = np.sqrt(np.mean(diff ** 2))
    return rms

# Get a list of image files to compare
image_files = glob.glob(r"filepath.jpeg")
# Sort the files based on the number in the filename
image_files.sort(key=lambda x: int(re.findall(r'\d+', x)[-1]))
image_files = image_files[50:]  # Ignore the first 50 images

# Create a list of image pair names and RMS values
image_pairs = []
rms_values = []

for i in range(len(image_files) - 1):
    img1 = cv2.imread(image_files[i], cv2.IMREAD_GRAYSCALE)
    img2 = cv2.imread(image_files[i + 1], cv2.IMREAD_GRAYSCALE)

    if img1 is None or img2 is None:
        raise ValueError("Could not read one or more input images.")

    image_pair_name = os.path.basename(image_files[i]) + " vs " + os.path.basename(image_files[i + 1])
    image_pairs.append(image_pair_name)
    rms_values.append(rms_diff(img1, img2))

# Create a line plot of RMS values
fig, ax = plt.subplots(figsize=(50, 6))  # Set the figure size

# Increase the spacing between plotted points on the x-axis
x = np.arange(0, len(rms_values) * 60, 60)
line, = ax.plot(x, rms_values, '-o')

# Set x-axis label
ax.set_xlabel("Image Pair")

# Set y-axis label
ax.set_ylabel("RMS")

# Remove x-axis tick labels
ax.set_xticklabels([])

# Create a list of annotations to display as tooltips
annotations = []
for i, rms, image_pair_name in zip(range(len(rms_values)), rms_values, image_pairs):
    annotation = f"{image_pair_name}<br>RMS: {rms:.4f}"
    annotations.append(annotation)

# Create an interactive tooltip
tooltip = plugins.PointHTMLTooltip(line, labels=annotations)

# Add the tooltip plugin to the figure
plugins.connect(fig, tooltip)

# Save the interactive HTML plot
output_file_path = r"output.html"
mpld3.save_html(fig, output_file_path)

# Display the plot
mpld3.show()
```

Figure A.2: Python code used to generate heatmaps from laser spectral data.

A.3 Appendix 3

Example of a histogram plot generated by the surface texture measurement module.

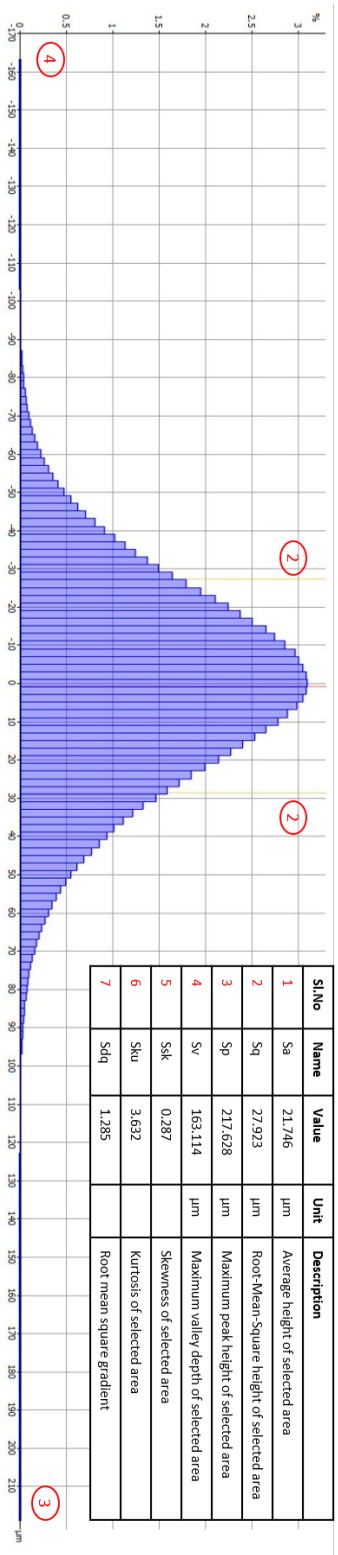

Sl.No	Name	Value	Unit	Description
1	Sa	21.746	µm	Average height of selected area
2	Sq	27.923	µm	Root-Mean-Square height of selected area
3	Sp	217.628	µm	Maximum peak height of selected area
4	Sv	163.114	µm	Maximum valley depth of selected area
5	Ssk	0.287		Skewness of selected area
6	Sku	3.632		Kurtosis of selected area
7	Sdq	1.285		Root mean square gradient

Figure A.3: Histogram plot representing the Sq, Sp, Sv values

DEPARTMENT OF SOME SUBJECT OR TECHNOLOGY
CHALMERS UNIVERSITY OF TECHNOLOGY
Gothenburg, Sweden
www.chalmers.se

CHALMERS
UNIVERSITY OF TECHNOLOGY